



UNIVERSITY OF
CAMBRIDGE

**Numerical study of detonation in solid explosives under
hydrodynamic and elastic-plastic confinement**

Eleftherios Ioannou

Selwyn College

September 2018

This dissertation is submitted for the degree of Doctor of Philosophy

Declaration

This dissertation is the result of my own work and includes nothing which is the outcome of work done in collaboration except as declared in the Preface and specified in the text. It is not substantially the same as any that I have submitted, or am concurrently submitting, for a degree or diploma or other qualification at the University of Cambridge or any other University or similar institution except as declared in the Preface and specified in the text. I further state that no substantial part of my dissertation has already been submitted, or is being concurrently submitted, for any such degree, diploma or other qualification at the University of Cambridge or any other University or similar institution except as declared in the Preface and specified in the text. This dissertation does not exceed the prescribed limit of 60 000 words.

Eleftherios Ioannou
September 2018

Numerical study of detonation in solid explosives under hydrodynamic and elastic-plastic confinement

Eleftherios Ioannou

Initiation devices used in mining have strict requirements for safety and efficiency. However, the analysis of their operation is encumbered by their complex design which involves multiple explosive charges and inert materials. We use numerical simulations to study detonation in configurations involving complex geometry and multiple materials with the aim of revealing key features of their internal processes and improving their reliability and performance. The mathematical model is based on a two-phase reactive formulation and is extended with porosity and shock desensitization models. It is coupled with appropriate inert material models for fluids and solids to accurately capture their interaction with the detonation wave.

We initially consider detonation propagation in annular charges. The model and implementation are validated against experimental data for steady state propagation. Then, the numerical solution is used to obtain a detailed description of the speed of the detonation wave along the annular arc and a new description of the transition phase is proposed. Further, a parametric study is performed in which the dependence of the transition phase and steady state on the dimensions of the annulus is analysed.

The rest of the thesis examines detonation in explosive devices used in the initiation of tertiary explosives in mining. First, we consider the response of a detonator in isolation, guided by an underwater explosion test. Following validation, the strength of the blast wave is examined at several distances from the detonator. Results show that the blast wave in the near field is asymmetric and stronger along the axis of the detonator. Further, the near field blast wave varies considerably between detonators of different shell material and thickness while the pulse in the far field is similar. This indicates that the fine differences between detonators cannot be captured by tests that consider the blast wave at a single point in the far field.

Lastly, we study the complete configuration used to initiate explosives in mining blastholes which involves a detonator and a booster. The reactive model is extended to account for shock desensitization. The model is validated and a series of simulations of the detonator and booster configuration, with and without desensitization, are performed. These show that the influence of desensitization is significant and can lead to the formation of dead zones in the explosive which have a critical impact on booster performance. Depending on the material of the detonator shell, the initiation of the booster can result in only a small non-reacted region or in an extensive desensitized zone which prevents the detonation of a large portion of the explosive.

Acknowledgements

I would like to thank my supervisor Dr Nikos Nikiforakis for giving me the opportunity to do this work and for his continuous support throughout my postgraduate studies. I also thank Dr Alan Minchinton of Orica for useful discussions and advice as well as Dr Louisa Michael and Dr Stefan Schoch for their help and collaboration.

I gratefully acknowledge the funding received towards my PhD from the Engineering and Physical Science Research Council and from the Department of Physics at the University of Cambridge.

I also deeply thank the members of the LSC group who became good friends and enriched my life in Cambridge. In particular, my office mates Lukas Wutschitz, Nandan Gokhale and Murray Cutforth for intriguing discussions and fun times.

Lastly, I would like to thank my wife, Christiana and my parents, Despo and Spyros for their endless support and encouragement which made the whole effort easier.

Contents

Abstract	v
Acknowledgements	vii
Contents	xi
1 Introduction	1
1.1 Case studies	3
1.2 Computational framework	6
1.3 Outline of the thesis	7
1.4 Publications	7
2 A hybrid multiphase model	9
2.1 Conservative variables formulation	11
2.2 Closure conditions	13
2.3 Sound speed	13
2.4 Hyperbolicity	16
2.5 JWL equation of state	17
2.6 Reaction rate law	17
2.7 Numerical solution	19
3 Detonation propagation in annular explosive charges	23
3.1 Introduction	23
3.2 Mathematical model and numerical solution	29
3.2.1 Data set and non-dimensionalization	29
3.2.2 Detonation front detection	31
3.3 Validation and grid convergence	32
3.3.1 One-dimensional steady state detonation	32

3.3.2	Steady detonation in cylindrical charges	33
3.3.3	Convergence study	35
3.4	The Lyle and Hayes experiments	38
3.5	The effect of the boundaries of the annular charge	39
3.6	The effect of the dimensions of the annular charge	44
3.6.1	Steady state	44
3.6.2	Transition phase	49
3.7	Conclusions	51
4	Initiation capability of detonators	55
4.1	Introduction	55
4.1.1	Types of detonators	58
4.1.2	Tests of detonator initiation capability	60
4.1.3	European standard test	63
4.2	Equations of state	66
4.2.1	The snow plough porosity model for the JWL EOS	66
4.2.2	Stiffened gas EOS	69
4.2.3	Parameter set for the explosive	70
4.3	Problem setup and convergence	71
4.4	Validation	74
4.4.1	One dimensional steady detonation	74
4.4.2	Underwater initiation capability test	75
4.5	The nature of the blast wave	79
4.6	The effect of shell material	84
4.7	The effect of the shell thickness	88
4.8	Conclusions	91
5	Performance evaluation of boosters	95
5.1	Introduction	95
5.2	Shock desensitization of solid explosives	97
5.3	Mathematical model of desensitization	100
5.3.1	The desensitization model by DeOliveira et al.	102
5.4	Validation	105
5.4.1	Detonation diffraction around a rigid corner	105
5.4.2	Detonation diffraction around a solid corner	108
5.4.3	The Jack Rabbit experiments	111

5.4.4	Desensitization model parameters for composition B	118
5.5	The booster configuration	120
5.6	Initiation of the booster without desensitization	122
5.7	The effect of detonator shell material	125
5.8	The effect of detonator shell thickness	129
5.9	The effect of detonator positioning	129
5.10	Conclusions	132
6	Conclusions	135
6.1	Future work	137
	Bibliography	139

Chapter 1

Introduction

Explosive devices are used in a variety of civil applications ranging from mining and construction to welding and airbag deployment. They have seen rapid development driven by the growing interest of government agencies focusing on safety and security as well as of the private sector which strives for more efficient and cost-effective solutions. In addition, explosives are of interest to the academic community because of their complex micro-structure and dynamic response which can produce pressures and temperatures of extreme magnitude.

The advancements in explosive technology have led to more refined, precision devices. These have complex designs that involve multiple charges in arbitrary shapes and are confined with a variety of materials. In particular, the initiation of tertiary explosives in mining blastholes uses a three-step mechanism which involves a detonator and booster configuration. This means that the initiating impulse is generated by a process in which detonations are transmitted through multiple charges and undergo several wave phenomena such as diffraction and interaction with material interfaces before transmitting a shock wave into the blasthole explosive.

The explosives considered in this study belong to the category of high explosives in which reactions propagate at supersonic speed forming a detonation wave. In particular, we consider explosives in the physical forms of pressings, castings and polymer bonded which are blends of explosives and inert materials with tailored mechanical and reactive properties. These are solid, heterogeneous explosives with a complex micro-structure that may involve explosive grains of several sizes, pores and cracks. The micro-structure plays an important role in the behaviour of these explosives. It allows for a multitude of physical processes that lead to the formation of hotspots and influence the characteristics of the initiation and propagation of detonation in the explosive.

The scientific study of detonation spans over a century and began with the classic theories of Chapman-Jouguet (CJ) and Zel'dovich-von Neumann-Döring (ZND) [1]. These are one-dimensional analytic models that can determine the properties of a steady detonation wave. However, the study of more complicated configurations involving unsteady detonation waves and complex geometry requires the use of reactive models coupled with hydrodynamics and solved computationally.

Reactive models are concerned with the continuum scale and ignore the micro-structure of the explosives. Instead, they rely on phenomenological models which aim to capture the macroscopic behaviour of the explosive and are based on the underlying processes that govern the initiation and propagation of detonation. The formulation of these rate laws, makes them easy to incorporate in hydrodynamic codes which solve a set of equations derived from the conservation laws of mass, momentum and energy.

The calibration of these models relies on experimental data. Over the years, experiments have been performed for the purposes of providing parameter sets for different explosives. More recently, high quality data from experiments utilizing new diagnostic techniques have led to the development of high-fidelity reactive models and the extension of older ones. One of the most widely used models is the pressure-based Ignition and Growth [2] which has been used to simulate a large range of reactive experiments with considerable success. Its drawback is that some detonation processes require a different set of parameters to be accurately captured and the fact that it does not naturally account for shock desensitization (the effect of weak shocks on the reactive properties of the explosive). More recent models include the entropy-based CREST [3] and shock temperature dependant AWSO [4] which have shown encouraging results for modelling explosives in different initial conditions and account for shock desensitization without modifications. A review of reactive models along with their successes and challenges is presented in a recent review paper by researchers at AWE [5].

The work presented in this thesis uses reactive models to study detonation propagation in charges of complex geometry and its effects on the surrounding materials. The detonation in such geometries undergoes diffraction and interaction with material boundaries that introduce additional waves which influence the propagation of detonation. The complexity of the resulting flow makes these configurations difficult to tackle analytically and cumbersome to investigate experimentally. The success of reactive models in capturing a variety of detonation processes motivates the numerical study of such configurations which have the potential of providing useful insights and aid the experimental investigations in the development of safer and more efficient initiation devices.

The reactive model used in this work is Ignition and Growth (I&G) which was selected because of its extensive library of parameter sets for different explosives. For some of the applications considered, the model is extended with a porosity and desensitization model. The response of the detonation is heavily dependant on the inert confining materials. As such, appropriate models are used for the inert materials present in the simulation. These are an inviscid hydrodynamic model for fluids and an elastic-plastic formulation for metal materials. A multi-material methodology is employed that allows for the simulation of materials described by different models and captures their interaction. The numerical methods used for the solution of the material models and the multi-material algorithms are implemented within a parallel adaptive mesh refinement framework that allows for increased resolution at regions of interest and efficient use of computational resources.

1.1 Case studies

The first application considered is the propagation of detonations in annular charges. Experimental studies [6, 7] have shown that a detonation propagating from a straight to an annular charge will undergo a transition phase and eventually reach a new steady state of constant angular velocity. The study follows the configuration of experiments performed at Lawrence Livermore National Laboratory (LLNL) which used an unconfined annular charge of LX-17 [6]. The numerical solution is validated against experimental studies of steady detonation in one-dimensional and cylindrical charges before being used to examine the transition of detonation in the annular region. The numerical results show good agreement with the experimentally measured steady detonation angular velocity, however the evolution of the outer detonation speed during the transition phase deviates from the exponential model proposed by Souers et al. [6].

The deviation from the proposed model motivated further analysis of the transition phase to gain more insight into the underlying processes. We examined configurations in which the explosive charge has only one of the boundaries of the annulus. These reveal that the behaviour of the detonation in the transition phase can be divided into two regimes where the first is governed by local effects at the outer boundary and the second by the effects originating from the inner boundary. At initial times, the local effects dominate before the disturbances from the change in geometry at the inner boundary travel across the detonation front and influence the outer part of the detonation. Furthermore, the effect of the dimensions of the annulus is investigated for both the transition phase and steady state. The results confirm a size effect for

1.1. Case studies

the angular steady state speed of the detonation which is observed experimentally but show a more complex dependence for the transition phase.

The second application is an investigation of the initiation capability of detonators. A detonator is a cylindrical device made out of a thin metal shell filled with a small explosive charge and used to ignite larger, less sensitive explosive charges. The issue of which methods are most appropriate for estimating initiation capability has not reached consensus but most studies advocate for the use of indirect tests [8, 9, 10]. Indirect tests place the detonator within the explosive that is meant to initiate as opposed to direct tests that measure the blast wave from an isolated detonator inside an inert material. In this study we consider a direct test performed in water which is described by the European standard [11] for determining the equivalent initiation capability of the detonators. This test measures the pressure pulse generated by the ignition of the detonator at a single point 400 mm off the side of the detonator. Despite this being a direct test which is believed to not portray the complete picture of the initiation capability, it is a widely used test and the existence of experimental data allows for the comparison with the numerical solution. Further, the numerical study of this configuration will provide certain insights which demonstrate the shortcomings of such tests.

The detonator design is based on the i-kon II detonators made by Orica which has a copper shell and PETN (Pentaerythritol tetranitrate) base charge. The manufacturing process of the detonators leaves the explosive highly porous (void fraction of approximately 15%) which influences its detonation characteristics. Thus, the reactive model is extended with the snow plough porosity model along with an adjustment of the parameters to match experimental values of CJ detonation. Further, we consider additional materials for the metal shell which include aluminium and steel.

The numerical solution is compared with experimental data from Klapötke et al. [12] which used similar detonators. Then we examine the blast wave generated by the detonator at several distances in the directions along and normal to the axis of the detonator. The results show that the blast wave is asymmetric and is stronger in the axial direction. The difference is significant since the blast wave peak pressures along the axis have twice the magnitude of the normal direction. In addition, the investigation into different materials for the shell of the detonator indicates that the near field blast wave varies greatly between materials. The aluminium detonator generates a blast wave that has double the peak pressure of the blast wave produced by the copper and steel detonator. However, this difference does not persist in the far field where the blast wave from all detonators is similar.

The asymmetric nature of the blast wave generated by detonators and the differences between materials in the near field, indicate that tests of initiation capability that consider a single point in the far field do not capture the fine features of it. This agrees with arguments presented in several experimental studies that the detonators should be investigated through indirect tests that consider the explosive it is meant to ignite. In the case of the mining detonators, this is the booster explosive.

The study of the initiation process of a booster device is the last application considered. A booster is the second part in the initiation train of a tertiary explosive. It consists of an insensitive high explosive placed in a plastic shell. The detonator is placed within the booster charge and its purpose is to provide an impulse that will generate a detonation in the booster which in turn will provide a strong stimulus for the initiation of the insensitive explosive in the blasthole.

The directional variation in the strength of the shock wave produced by the detonator makes the booster explosive susceptible to shock desensitization. This phenomenon has been observed in all polymer bonded explosives and has different manifestations [5]. During double shock initiation, if the first shock is not strong enough to initiate reaction, it will make the explosive harder to initiate by the subsequent shock. In detonation propagation, an established detonation can be quenched when it enters a region that has been desensitized by the prior passage of a weak shock. This will result in a portion of explosive remaining non-reacted, commonly called dead-zone.

The cause of shock desensitization is not completely understood and two explanations exist [13]. By extension, there are also different ways of modelling it depending on the reactive model. For the pressure-base model I&G used in this study, capturing the desensitization effect requires the use of a desensitization model. We use the model proposed by DeOliveira et al. [14] which has shown encouraging results in capturing dead zone formation.

The booster design also follows an actual booster, the 400 g Global Booster produced by Orica. The explosive inside is selected to be composition B which has been widely used in boosters and also because of the availability of a reaction parameter set and of experiments required to determine the desensitization parameters. The study considers the initiation of the booster with and without desensitization and for a range of different detonators. The numerical results indicate that desensitization is significant and leads to the formation of dead-zones. In the case of aluminium, the dead zone is small and has minimal impact on the performance of the booster. However the copper detonator causes a slower formation of the detonation that allows for a more extensive desensitization and eventually inhibits the detonation of the majority of the explosive.

1.2. Computational framework

The study concludes with the examination of thicker detonator shells and an alternative design which places the detonator closer to the top of the booster.

1.2 Computational framework

The reactive model presented in the study is implemented within a general Computational Fluid Dynamics (CFD) code developed by the Laboratory for Scientific Computing (LSC) at the University of Cambridge. This framework provides the required data structures and numerical methods required for solving hyperbolic systems of equations using finite volume methods in an Eulerian frame of reference. It incorporates parallel Adaptive Mesh Refinement (AMR) which enables increased resolution in areas of interest as well as the ability to run on multiple processors.

Further, the LSC code implements a multi-material methodology which enables the simulation of materials described by different models and their interaction. This is achieved by the combined use of level-set algorithms for interface tracking and ghost-fluid methods for capturing the interaction between materials. Each material is represented by a separate model and can be solved by an independent solver. A level-set function is used to track the boundaries of each material as it moves in the domain. The interaction between materials is captured through mixed Riemann solvers. These allow the solution of the Riemann problem between two different types of materials. The computed solution is used to populate the ghost fluid cells outside the material and to advect the level-set of the material. Thus, every material model within the LSC framework must be accompanied by the appropriate mixed Riemann solvers depending on the materials it interacts with.

The explosive materials considered in this study are modelled using a hybrid diffuse-interface and corresponding equations of state, reaction and desensitization rate. The implementation of this model and accompanying solvers was performed by the author for the purposes of this study. The inert materials make use of material models already implemented within the LSC computational framework. The fluid materials such as water are represented with the inviscid Euler equations and appropriate equations of state. The metal materials are modelled with an elastic-plastic formulation based on the Godunov-Romenskii formulation [15] and follow the work of Barton and Drikakis [16] for the elastic part and Miller and Colella [17] for the plastic update. The model represents an Eulerian formulation of the equations of solid mechanics and allows for an accurate description of the elastic and plastic response of the material. Further details on the implementation of this model within the LSC computational framework

can be found in previous works by members of the laboratory [18, 19].

1.3 Outline of the thesis

The next chapter presents the mathematical model used for the explosive materials. The focus is on deriving the expressions for the partial derivatives used in the calculation of sound speed for the case of a general equation of state. These expressions are used both in the calculation of the time step as well as for the estimation of the wave speeds in the HLLC approximate Riemann solver. The chapter also presents the I&G reactive model which includes the JWL equation of state and the reaction rate.

Chapter 3 presents the numerical study of detonation propagation in annular charges. It is preceded by an extensive validation which considers steady state propagation of detonation in one-dimensional, cylindrical and annular geometries. The evolution of detonation speeds along the boundaries of the annulus is presented along with configurations omitting one of the boundaries of the annulus. The study concludes with the parametric study to determine the influence of the dimensions of the annulus on the transition phase and steady state.

The following two chapters (4 and 5) consider the three-step initiation train used to ignite the explosive in mining blastholes. It consists of the detonator and the booster. The detonator is studied in isolation in chapter 4 where the properties of the generated blast wave are identified. This is in addition to an investigation into the differences between detonators of different shell material and thickness. There is also a description of the snow plough model used to account for the porosity of the explosive used in industrial detonators. The complete detonator and booster configuration is considered in chapter 5. The desensitization model used in this part is introduced and validated against several test cases. Subsequently, the investigation considers the effects of desensitization in the initiation of the booster as well as the differences in the initiation by different detonator designs.

The last chapter is dedicated to conclusions and a discussion of future work.

1.4 Publications

Part of the work presented in this thesis has already been published in the following:

1. Ioannou, E., Schoch, S., Nikiforakis, N. and Michael, L., 2017. *Detonation propagation in annular arcs of condensed phase explosives*. *Physics of Fluids*, 29(11),

1.4. *Publications*

p.116102.

2. Ioannou, E., Nikiforakis, N. and Michael, L., 2018. *Modeling of Detonation and Desensitization in Condensed Phase Explosives of Complex Geometry*. Sixteenth International Detonation Symposium.

Chapter 2

A hybrid multiphase model

Numerical simulations involving explosives under confinement require a mathematical formulation that can model the physical properties of multiple materials and capture their interactions. Modelling heterogeneous explosives poses a particular challenge because resolving their complex micro-structure in a mesoscale numerical simulation is beyond the current computational capabilities. Instead, it is common to use a homogenized treatment at the continuum scale which averages the fine scale features of the explosive and accounts for the heterogeneous effects through a phenomenological reaction rate law.

The hydrodynamic model employed in this work was proposed by Michael and Nikiforakis [20] and follows the approach described above. It is a hybrid formulation for interfaces between immiscible homogeneous fluids, where one of the materials is further divided into two phases following the augmented Euler approach for modelling two phase explosives. It assumes a continuum hydrodynamic representation of the materials and allows for the modelling of an explosive with distinct equations of state for the reactants and products, and also for an additional inert material.

This formulation is particularly suitable for modelling explosives under compliant confinement because it can handle high density gradients across interfaces, without the generation of spurious oscillations in the solution. In addition, it allows for the use of most types of equations of state and can be used for both ignition and detonation propagation studies.

The mathematical model is defined by the following system of equations

$$\begin{aligned}
\frac{\partial z\rho_1}{\partial t} + \nabla \cdot z\rho_1\mathbf{u} &= 0, \\
\frac{\partial(1-z)\rho_2}{\partial t} + \nabla \cdot (1-z)\rho_2\mathbf{u} &= 0, \\
\frac{\partial\rho\mathbf{u}}{\partial t} + \nabla \cdot (\rho\mathbf{u} \otimes \mathbf{u} + p\mathbf{I}) &= 0, \\
\frac{\partial\rho E}{\partial t} + \nabla \cdot (\rho E + p)\mathbf{u} &= 0, \\
\frac{\partial z}{\partial t} + \mathbf{u}\nabla z &= 0, \\
\frac{\partial z\rho_1\lambda}{\partial t} + \nabla \cdot z\rho_1\lambda\mathbf{u} &= z\rho_1\mathcal{R}.
\end{aligned} \tag{2.1}$$

It features two continuity equations which represent the discrete conservation of mass for each material as well as conservation laws for the momentum and energy of the mixture. Quantities ρ_1 and ρ_2 correspond to the density of the explosive and the inert material respectively. Quantities ρ , \mathbf{u} , p and E are the mixture density, velocity, pressure and total specific energy defined as

$$E = e + \frac{\|\mathbf{u}\|^2}{2},$$

where e is the specific internal energy of the mixture.

The composition of the mixture is determined by the quantity $z \in [0, 1]$ which represents the volume fraction of the explosive and is governed by an advection equation. Equivalently, quantity $1 - z$ is the volume fraction of the inert material. The explosive material is further divided into two phases, which represent the reactants and the products. We define $\lambda \in [0, 1]$ as the mass fraction of the reactants. This is also governed by an advection equation with a source term \mathcal{R} describing the chemical reactions that turn reactants into products. However, it is combined with the continuity equation of the explosive material and put into a conservative form which represents the conservation of mass of the reactants in the absence of reactions. The equations do not include any terms for viscous friction or heat conduction as it is assumed that their effect is negligible in the considered case studies.

The formulation allows for the interface to diffuse on a small number of computational cells over which a set of mixture rules has to be defined. These rules relate the thermodynamic variables of the mixture to those of the individual constituents.

2.1. Conservative variables formulation

Considering mass and energy as additive quantities, the mixture variables are given by

$$\begin{aligned}\rho &= z\rho_1 + (1 - z)\rho_2, \\ \rho e &= z\rho_1 e_1 + (1 - z)\rho_2 e_2,\end{aligned}\tag{2.2}$$

where quantities with subscript 1 and 2 correspond to the explosive and the inert material respectively. Subsequently, the density and the specific internal energy of the two-phase explosive are given by

$$\begin{aligned}\frac{1}{\rho_1} &= \lambda \frac{1}{\rho_a} + (1 - \lambda) \frac{1}{\rho_b}, \\ e_1 &= \lambda e_a + (1 - \lambda) e_b,\end{aligned}\tag{2.3}$$

where subscripts a and b denote quantities of the reactants and the products that comprise the explosive.

In addition to the mixture rules, the system requires closure conditions to be fully determined. Between the explosive and the inert material only one closure condition is necessary, as the density of each material is readily available from the state variables of the equations. Between the reactants and the products, two mixture rules are required as only the total explosive density is known and root finding procedures are required to determine the individual reactants and products densities. Here, the closure conditions chosen are isobaric between the explosive and inert material as it has been proven to give better stability at the interfaces [21], and isobaric and isothermal between the reactants and products as in similar studies [22, 23, 24, 25].

We note the convention of using the term *materials* to refer to the explosive and inert material which have individual mass conservation equations and the term *phases* to refer to the reactants and products of the explosive.

2.1 Conservative variables formulation

The system of equations needs the definition of a relation between pressure and the rest of the thermodynamic variables to be complete. In single material models this is given by the EOS, however in the case of multiple materials one has to define an equivalent *generalized equation of state* for the mixture. This definition is based on the individual EOS for each material and the selected closure conditions. In general, we can assume that pressure will be a function of variables $\rho_1, \rho_2, e, z, \lambda$.

The analysis of the formulation begins by expressing the system in quasi-linear form

2.1. Conservative variables formulation

and examine the Jacobian flux matrix. We restrict the analysis in one dimension for simplicity and reformulate the equations to an equivalent, fully conservative form. The homogeneous system in vector form

$$\mathbf{q}_t + f_x(\mathbf{q}) = 0, \quad (2.4)$$

has vectors

$$\mathbf{q} = \begin{bmatrix} z\rho_1 \\ (1-z)\rho_2 \\ \rho u \\ \rho E \\ \rho z \\ \rho \lambda \end{bmatrix} \quad \text{and} \quad f(\mathbf{q}) = \begin{bmatrix} z\rho_1 u \\ (1-z)\rho_2 u \\ \rho u^2 + p \\ (\rho E + p)u \\ \rho z u \\ \rho \lambda u \end{bmatrix}. \quad (2.5)$$

The above system is then expressed in a quasi-linear form

$$\mathbf{q}_t + J_{f(\mathbf{q})}\mathbf{q}_x = 0, \quad (2.6)$$

where $J_{f(\mathbf{q})}$ is the Jacobian matrix. The Jacobian matrix represents the partial derivatives of the flux vector with respect to the conserved variables of the state vector and thus the flux vector elements must be expressed as a function of the conserved variables. This calculation makes use of a general form of the pressure relation $p(\rho_1, \rho_2, e, z, \lambda)$ to relate pressure to the rest of the variables.

The derivation of the Jacobian matrix was performed using Wolfram Mathematica along with the calculation of its eigenvalues. These are $u, u, u, u - c, u + c$ where c is given by

$$c^2 = \frac{p}{\rho^2} \left(\frac{\partial p}{\partial e} \right)_{\rho_i, z, \lambda} + \sum_i^{1,2} \frac{\rho_i}{\rho} \left(\frac{\partial p}{\partial \rho_i} \right)_{e, z, \lambda}, \quad (2.7)$$

and corresponds to the mixture sound speed.

As can be seen, the sound speed calculation involves partial derivatives of the mixture pressure function. Determining this function requires the definition of the closure conditions that complete the system.

2.2 Closure conditions

The selected closure conditions are isobaric between materials and isobaric and isothermal between the phases of the explosive.

$$p_1 = p_2 = p_a = p_b \quad (2.8)$$

$$T_a = T_b \quad (2.9)$$

The above relations, combined with the mixture rules (2.2) and (2.3) result in a system of three equations

$$\begin{aligned} \rho_1^{-1} &= \lambda \rho_a^{-1} + (1 - \lambda) \rho_b^{-1} \\ \rho e &= z \rho_1 [\lambda e_a(\rho_a, p) + (1 - \lambda) e_b(\rho_b, p)] + (1 - z) \rho_2 e_2(\rho_2, p) \\ T_a(\rho_a, p) &= T_b(\rho_b, p) \end{aligned} \quad (2.10)$$

with three unknowns (ρ_a, ρ_b, p) . Having complex equations of state, such as those used in modelling condensed phase explosives will result in a nonlinear system which can be difficult to solve. In most cases an analytical expression of the solution cannot be found and an iterative numerical method is used.

2.3 Sound speed

The mixture pressure function $p(\rho_1, \rho_2, e, z, \lambda)$ is implicitly defined by a system of equations given in (2.10) which complicates the derivation of the partial derivatives.

One way of deriving them is to use an expression for the EOS such as the Mie-Grüneisen form, which is a general form that most EOS can be written into. A second way is to use implicit differentiation of system (2.10). Alternatively we follow the analysis in [21] and consider the total differential of the general pressure function

$$dp = \sum_i^{1,2} \frac{\partial p}{\partial \rho_i} d\rho_i + \frac{\partial p}{\partial e} de + \frac{\partial p}{\partial z} dz + \frac{\partial p}{\partial \lambda} d\lambda. \quad (2.11)$$

If such expression can be found it will provide the required partial derivatives.

The EOS of each single material can be written in the form of differential

$$de_i = \frac{\partial e_i}{\partial \rho_i} d\rho_i + \frac{\partial e_i}{\partial p_i} dp_i \quad i = a, b, 2, \quad (2.12)$$

2.3. Sound speed

but in the case of material 1, it is a mixture of two phases so the expression will also include the mass fraction variable λ

$$de_1 = \frac{\partial e_1}{\partial \rho_1} d\rho_1 + \frac{\partial e_1}{\partial p_1} dp_1 + \frac{\partial e_1}{\partial \lambda} d\lambda. \quad (2.13)$$

Expanding the differentials of the mixture rules (2.2) yields

$$d\rho = \sum_i^{1,2} d(z_i \rho_i) = \sum_i^{1,2} z_i d\rho_i + \sum_i^{1,2} \rho_i dz_i, \quad (2.14)$$

$$d(\rho e) = \sum_i^{1,2} d(z_i \rho_i e_i) \rightarrow \rho de + e d\rho = \sum_i^{1,2} z_i \rho_i de_i + \sum_i^{1,2} e_i d(z_i \rho_i). \quad (2.15)$$

Replacing the expressions of the differentials (2.12), (2.13) and (2.14) into (2.15) we obtain

$$\begin{aligned} \sum_i^{1,2} z_i \rho_i \frac{\partial e_i}{\partial p_i} dp_i = \rho de + \sum_i^{1,2} z_i (e - e_i - \rho_i \frac{\partial e_i}{\partial \rho_i}) d\rho_i \\ + \sum_i^{1,2} (e - e_i) \rho_i dz_i - z_1 \rho_1 \frac{\partial e_1}{\partial \lambda} d\lambda, \end{aligned} \quad (2.16)$$

and by applying the isobaric closure condition $dp = dp_i$ and using $dz = dz_1 = -dz_2$, simplifies the expression to

$$\begin{aligned} \Theta dp = \rho de + \sum_i^{1,2} z_i \left(e - e_i - \rho_i \frac{\partial e_i}{\partial \rho_i} \right) d\rho_i \\ + [(e - e_1) \rho_1 - (e - e_2) \rho_2] dz - z_1 \rho_1 \frac{\partial e_1}{\partial \lambda} d\lambda \end{aligned} \quad (2.17)$$

where

$$\Theta = \sum_i^{1,2} z_i \rho_i \frac{\partial e_i}{\partial p} \quad (2.18)$$

Expression (2.17) is the total differential of the generalized pressure function from which we can obtain the required partial derivatives.

The derived partial derivatives of the generalized pressure function are replaced

into the mixture sound speed expression (2.7) yielding

$$\begin{aligned}\Theta c^2 &= \sum_i^{1,2} y_i \left(e - e_i - \rho_i \frac{\partial e_i}{\partial \rho_i} \right) + \frac{p}{\rho} \rightarrow \\ \Theta c^2 &= \sum_i^{1,2} y_i \left(\frac{p}{\rho_i} - \rho_i \frac{\partial e_i}{\partial \rho_i} \right) \rightarrow \\ \Theta c^2 &= \sum_i^{1,2} y_i \frac{\partial e_i}{\partial p} \rho_i c_i^2, \quad (2.19)\end{aligned}$$

where

$$y_i = \frac{z_i \rho_i}{\rho}, \quad (2.20)$$

is the mass fraction and

$$c_i^2 = \frac{p}{\rho_i^2} \left(\frac{\partial p}{\partial e_i} \right)_{\rho_i} + \left(\frac{\partial p}{\partial \rho_i} \right)_{e_i}, \quad (2.21)$$

the sound speed of each material.

Expression (2.19) implies that the mixture sound speed is a weighted average sound speed of each material. This sound speed expression allows the calculation of the eigenvalues of the system of equations that make up the mathematical model. The eigenvalues calculation is required for the numerical solution of the system using finite volume methods and are not necessarily related to a physical sound speed of the mixture.

Material 2 is a single phase material and its sound speed is readily available from its EOS. However, material 1 is a two-phase material and has a form of generalized EOS which is implicitly defined by the mixture rule (2.3) and the closure conditions.

Similar to the system of equations in (2.10), we can define a subsystem which relates the thermodynamic variables of each phase of material 1.

$$\begin{aligned}\rho_1^{-1} &= \lambda \rho_a^{-1} + (1 - \lambda) \rho_b^{-1} \\ e_1 &= \lambda e_a(\rho_a, p) + (1 - \lambda) e_b(\rho_b, p) \\ T_a(\rho_a, p) &= T_b(\rho_b, p)\end{aligned} \quad (2.22)$$

In general, this is a nonlinear system of equations and an analytical expression of the solution is not possible. Thus, the derivation of the partial derivatives requires the

2.4. Hyperbolicity

use of implicit differentiation. For a system of m equations and $m + n$ variables

$$F_i(x_1, \dots, x_n, y_1, \dots, y_m) = 0 \quad i = 1, \dots, m \quad (2.23)$$

where x_1, \dots, x_n are the independent variables and y_1, \dots, y_m are the dependent variables, the partial derivatives of the dependent variables with respect to an independent variable x_k are given from the solution of the linear system

$$\frac{\partial F_i}{\partial y_j} \frac{\partial y_j}{\partial x_k} = -\frac{\partial F_i}{\partial x_k}. \quad (2.24)$$

The implicit differentiation of system (2.22) was performed using Wolfram Mathematica and produced the following expressions of partial derivatives

$$\left(\frac{\partial e_1}{\partial \rho_1} \right)_{p,\lambda} = \frac{\rho_a^2 \rho_b^2 \left(\lambda \frac{\partial e_a}{\partial \rho_a} \frac{\partial T_b}{\partial \rho_b} + (1 - \lambda) \frac{\partial e_b}{\partial \rho_b} \frac{\partial T_a}{\partial \rho_a} \right)}{\rho^2 \left(\lambda \rho_b^2 \frac{\partial T_b}{\partial \rho_b} + (1 - \lambda) \rho_a^2 \frac{\partial T_a}{\partial \rho_a} \right)} \quad (2.25)$$

$$\left(\frac{\partial e_1}{\partial p} \right)_{\rho_1,\lambda} = \lambda \frac{\partial e_a}{\partial p} + (1 - \lambda) \frac{\partial e_b}{\partial p} - \frac{\lambda(1 - \lambda) \left(\rho_a^2 \frac{\partial e_a}{\partial \rho_a} - \rho_b^2 \frac{\partial e_b}{\partial \rho_b} \right) \left(\frac{\partial T_a}{\partial p} - \frac{\partial T_b}{\partial p} \right)}{\left(\lambda \rho_b^2 \frac{\partial T_b}{\partial \rho_b} + (1 - \lambda) \rho_a^2 \frac{\partial T_a}{\partial \rho_a} \right)} \quad (2.26)$$

which are used to compute the sound speed of the two-phase material 1.

It is useful to note that it is possible to use implicit differentiation on the system of equations (2.10) to directly derive the partial derivatives required in the sound speed calculation (2.7). However, this results in more complicated and computationally expensive expressions. The method shown in this section decouples the two materials and requires the use of implicit differentiation only for the partial derivatives of material 1 which leads to simpler and faster computations. In addition, the calculation of the sound speed of each phase is also required in the calculation of the wave speeds at a cell interfaces.

2.4 Hyperbolicity

The system is hyperbolic if the mixture sound speed expression (2.7) is positive

$$c^2 \geq 0.$$

As shown in section 2.3, the sound speed expression with the isobaric closure

conditions is a weighted average of the sound speed of each material (2.19). So if the phase sound speeds are well defined by their individual material EOS, then the mixture sound speed will also be well defined.

2.5 JWL equation of state

The definition of an equation of state (EOS) for each material is required to close the system of equations of the mathematical formulation presented in this chapter. Following the standard Ignition and Growth formulation, reactants and products are modelled using two distinct Jones-Wilkins-Lee (JWL) equations of state.

The JWL equation of state can be written in the Mie-Grüneisen form

$$e - e_{\text{ref}}(\rho) = \frac{p - p_{\text{ref}}(\rho)}{\rho\Gamma(\rho)}, \quad (2.27)$$

$$T = \frac{e - e_{\text{ref}}(\rho)}{c_v}, \quad (2.28)$$

with a constant Grüneisen coefficient $\Gamma(\rho) = \Gamma_0$ and the following reference curves

$$p_{\text{ref}}(\rho) = A \exp\left(-R_1 \frac{\rho_0}{\rho}\right) + B \exp\left(-R_2 \frac{\rho_0}{\rho}\right), \quad (2.29)$$

$$e_{\text{ref}}(\rho) = \frac{A}{\rho_0 R_1} \exp\left(-R_1 \frac{\rho_0}{\rho}\right) + \frac{B}{\rho_0 R_2} \exp\left(-R_2 \frac{\rho_0}{\rho}\right) - Q, \quad (2.30)$$

where A , B , R_1 and R_2 are parameters calibrated for the particular explosive.

For the explosive products, the pressure reference curve of the JWL EOS represents the isentrope through the Chapman-Jouguet (CJ) point and is fitted to experimental data, usually from cylinder tests [1]. The energy reference curve is determined by integrating the pressure reference curve, since $de = -pdv$ for an isentropic process. For the reactants, the parameters are fitted to measurements of the Hugoniot locus through an initial state.

2.6 Reaction rate law

The reaction rate law used in this study is Ignition and Growth (I&G) [2] and plays an important role in capturing the reactive properties of the granular explosive within the homogeneous representation of the material. The heterogeneity of the explosive material is accounted for through this multi-stage, pressure-based reaction rate, which

2.6. Reaction rate law

provides a phenomenological description of the effects of the micro-structure of the explosive using macroscopic material parameters.

The I&G reaction rate model is given by

$$\mathcal{R} = \mathcal{R}_I + \mathcal{R}_{G_1} + \mathcal{R}_{G_2}, \quad (2.31)$$

and the three terms are defined as,

$$\mathcal{R}_I = I(1 - \phi)^b(\rho - 1 - a)^x H(\rho/\rho_0 - 1 - \alpha) H(\phi_{ig} - \phi), \quad (2.32)$$

$$\mathcal{R}_{G_1} = G_1(1 - \phi)^c \phi^d p^y H(\phi_{G_1} - \phi), \quad (2.33)$$

$$\mathcal{R}_{G_2} = G_2(1 - \phi)^e \phi^g p^z H(\phi - \phi_{G_2}), \quad (2.34)$$

where $H(x)$ is the Heaviside step function, $\phi = 1 - \lambda$ is the mass fraction of the products and ρ and p are the density and pressure of the explosive respectively. The rest of the parameters are constants that are calibrated for each particular explosive.

The I&G model captures the complex ignition and burning processes in heterogeneous explosives by using three terms to represent the processes occurring in the initiation and propagation of detonations in such explosives [23]. In the shock to detonation transition process, ignition occurs due to shock-induced heating and friction as well as hotspot formation through cavity collapse in porous explosives. These initiation mechanisms are represented in the ignition term (2.32) which is activated when density increases above a threshold α and is used only in the initial stages of the reaction.

The remaining two terms are called growth terms and have different interpretations depending on whether the application involves initiation or propagation of detonation [23]. In the first case, the second term represents the slow reactions starting at the hotspots and expanding into the surrounding explosive while the third term describes the quick transition to detonation induced by the coalescence of the growing hotspots. In the case of detonation propagation, the growth terms represent the formation of the products. In particular, term (2.33) models the rapid formation of gas products and term (2.34) the slow diffusion-controlled formation of solid carbon.

The JWL and I&G parameters are selected and adjusted jointly to accurately represent a specific explosive and regime of detonation. For example the parameters can be different between applications that involve either ignition or propagation of detonation, even for the same explosive.

2.7 Numerical solution

The mathematical formulation presented in this chapter constitutes a nonlinear hyperbolic system with source terms and is solved computationally using a series of numerical methods. Starting from the initial conditions, the numerical solution is advanced in time through the process of operator splitting. This allows for the separate solution of the homogeneous part using an appropriate hyperbolic solver and the independent use of an ODE solver to compute the effect of the source terms.

The hyperbolic part is solved using the finite volume method MUSCL-Hancock [26]. It is a high-resolution, shock capturing, Godunov-type reconstruction scheme which is second order accurate in time and space. To avoid spurious oscillations near steep gradients in the flow that would otherwise occur in high order schemes, we use the van Leer slope limiter [27], set on the primitive variables. The scheme requires a Riemann solver for calculating fluxes at cell interfaces for which we use HLLC [28]. The reaction rate source term, as well as geometric source terms arising from axisymmetric problems in cylindrical coordinates are solved using a 4th order Runge-Kutta method.

The multiphase nature of the hybrid model requires additional numerical methods and procedures that are beyond the classical methods for hyperbolic conservation laws mentioned above. In fact, the hybrid model is a fusion of two multiphase paradigms. The first uses a non-conservative volume fraction equation and two continuity equations, one for each of the partial densities of the two materials (reactive and inert). In contrast, the two phase densities of the explosive (reactive material) are not explicitly tracked, but are implicitly defined by the mass fraction and the total density of the mixture which are directly represented in the equations of the model. Each paradigm has its own advantages and challenges and requires different numerical treatment.

In the case of the non-conservative formulation, the equation that governs the volume fraction is solved with the Godunov method for advection equations [29]. This method reformulates the advection equation into the form

$$\frac{\partial z}{\partial t} + \frac{\partial uz}{\partial x} - z \frac{\partial u}{\partial x} = 0 \quad (2.35)$$

where only one dimension was considered for simplicity. The equation is then discretized following the finite volume method which uses the cell interface values

$$z_i^{n+1} = z_i^n - \frac{\Delta t}{\Delta x} \left[(uz)_{i+\frac{1}{2}}^n - (uz)_{i-\frac{1}{2}}^n - z_i^n \left(u_{i+\frac{1}{2}}^n - u_{i-\frac{1}{2}}^n \right) \right]. \quad (2.36)$$

2.7. Numerical solution

The above scheme updates the volume fraction and can be incorporated within a finite volume method by considering that quantity

$$f_{i\pm\frac{1}{2}}^n = (uz)_{i\pm\frac{1}{2}}^n - z_i^n u_{i\pm\frac{1}{2}}^n \quad (2.37)$$

represents the flux. It is apparent that this flux is not conservative since it depends on the value of the cell that is being updated. At each interface between neighbouring cells, two fluxes are calculated which correspond to the amount that exits one cell and enters the other. Since these two values are not the same, the quantity is not conserved in the flow. This scheme guarantees volume fraction positivity during the hyperbolic step and can be extended to second order with the use of a reconstruction scheme.

The second multiphase paradigm involves conservative equations only which can be solved with the classic finite volume methods, but the calculation of the phase densities and pressure of the mixture requires the solution of a nonlinear system of equations. This system was introduced in section 2.2 and is expressed by equation (2.10). The challenging aspect of this formulation is that it does not guarantee a unique solution. In fact, it is possible to have as many as five solutions when the explosive is represented by empirical equations of state, such as the JWL. Most of the solutions are not physical, either because of having negative pressure or imaginary sound speed. Thus, the procedure of obtaining a solution requires that each solution is assessed and rejected if not physical.

For the solution of the system, we first use the substitution method in which all equations are condensed into one single variable function. This is a function of one of the phase densities of the explosive and is solved with a root finding procedure. The particular phase, that the system will be solved for, is selected according to the mass fraction value. This is done to avoid loss of significance errors in the calculation of one phase density from the other. This calculation makes use of the densities mixture rule

$$v_0 = \lambda v_a + (1 - \lambda)v_b \quad (2.38)$$

where $v = \rho^{-1}$ is the volume, and involves the subtraction of the total volume of the explosive with the phase volume multiplied by its mass fraction. If the solution is computed for the dominant phase of the cell, then the subtraction may involve similar values which will lead to loss of accuracy due to catastrophic cancellation.

The root finding procedure combines the Newton-Raphson method with the bisection method to benefit from the speed of the first and the robustness of the second. Further,

the methods are set to iterate over a series of starting values and ranges respectively, until a physical solution is found. In the case of the Newton-Raphson method, the initial point is the solution in the previous time step. The Newton-Raphson method is sensitive to the starting point and thus, if an unphysical solution is returned, the procedure moves to a different starting point in an attempt to reach a new solution. It was found that the previous value, the total density and the reference (initial) density provide enough variation to eventually lead to the physical solution for the great majority of the cells.

The bisection method is used if all Newton-Raphson attempts fail. The range of phase density is set to an upper limit of 10-times the initial density (well above the maximum expected compression of the von Neumann point) and a corresponding lower limit is set according to the state of the cell. Any physical solution is expected to lie in this range. Additional solutions can exist outside this range, but are more likely to be unphysical. In practice, the initial range has been successful in leading to a physical solution whenever the solver had to resort to the bisection method. Nevertheless, the implemented algorithm does extend the range incrementally to cover for the general case, but it is not required for the simulations performed in this study.

The numerical procedure for the solution of the nonlinear system is a result of practical considerations and does not eliminate cases where only unphysical solutions are computed. This is a weakness of the mathematical formulation which does not guarantee that a physical solution is always available. In particular, the use of empirical equations of state will not be physical if the flow conditions move outside the range they were calibrated against. Thus, the robustness of this numerical algorithm will depend on the material models and initial conditions of a particular simulation. However, this procedure has proven to be a reliable way of obtaining a physical solution if it exists and has allowed the simulation of a wide range of explosive applications not limited to the ones considered in this study.

2.7. *Numerical solution*

Chapter 3

Detonation propagation in annular explosive charges

3.1 Introduction

Arbitrarily-shaped explosive charges are used in a variety of modern applications. The propagation of detonation waves in such charges is influenced by the geometry of the charge and exhibits different behaviour from the well-studied case of straight charges. This study uses numerical simulations to investigate detonation propagation in unconfined annular explosive charges in air. The aim is to identify the characteristic features of detonation in such geometries and to determine its dependence on the dimensions of the annular charge.

This work is guided by two experimental studies on annular charges. The first was performed by Lyle and Hayes at the Lawrence Livermore National Laboratory (LLNL) in the 1980s and is presented in a study by Souers et al. [6]. These used unconfined charges of various compositions of LX-17 shaped as a 90° annular arc with a square cross section. The detonation was initiated in a straight charge and was left to reach steady state before entering the annular section, as illustrated in figure 3.1. A series of electrical pins were used at the edges of the charge to measure arrival times of the detonation wave, in addition to a streak camera used to capture the shape of the detonation front as it exits the charge. The second experiment was performed by Lubyatinsky et al. [7] who presented results of arrival times and front break-out traces of detonation waves propagating in 180° annular arcs of an unspecified high explosive. This experiment involved explosive annuli of various widths and radii confined by two types of material, steel and PMMA.

3.1. Introduction

Experiments on annular charges were also performed for the purpose of calibrating and validating mathematical models for detonation propagation such as Detonation Shock Dynamics (DSD). Tonghu et al. [30] studied 60° , 90° and 125° annular arcs of a TATB-based explosive. They obtained detonation arrival times and front shapes using arrays of electrical pins and high speed photography and compared them against numerical results from a DSD computational code. Similarly, Bdzil et al. [31] measured the speed and front shape for a detonation exiting a 135° unconfined annular arc of PBX-9502. This was used for the validation of time-dependent [32] and steady [33] DSD calculations and were found to be in good agreement with the experimental results.

Similar experiments have been performed for gaseous explosives motivated by the development of rotating detonation engines. Nakayama et al. [34] studied annular configurations of different inner radii and same width for a range of characteristic detonation cell width. They classified detonation propagation in different modes; unstable, critical and stable depending on the magnitude of the variation of inner normal detonation velocity. A condition for stable propagation was determined based on the ratio of inner radius to characteristic cell width. In addition it was found that a scaled $D_n(k)$ relation exists which is almost independent of the configuration parameters, inner radius and characteristic cell width.

A common outcome of the aforementioned studies is that detonation propagation in annular charges settles to a steady state. This is characterized by constant angular velocity of the detonation wave as opposed to constant linear velocity observed in straight charges. Furthermore, there is a dependence of the steady angular velocity on the charge dimensions, similar to the diameter effect seen in straight charges. In particular, the reciprocal steady angular velocity has an affine dependence on the inner radius of the annular arc [7].

The shape of the detonation front in annular charges is asymmetric, in contrast to straight charges which is symmetric about the centre line. Its leading peak is close to the inner edge as seen in figure 3.1. Its position depends on the confining material which also affects the speed of the leading peak. Materials with high impedance induce higher leading peak speeds and smaller distances between the leading peak and the inner edge [7].

The condition of constant angular velocity results in notably different detonation speeds at each edge of the front. Denoting the steady detonation speed measured along the inner edge as V_S and along the outer edge as W_S , the constant angular velocity

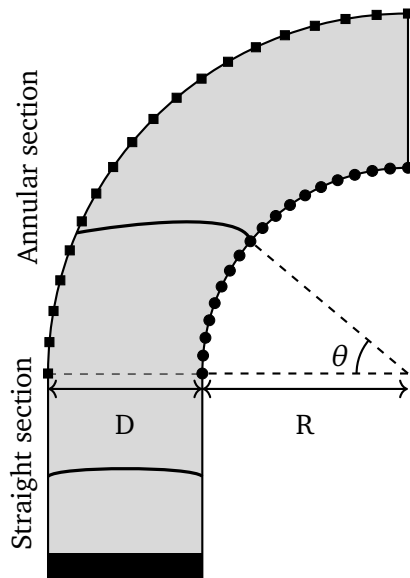


Figure 3.1: Illustration of the annular charge configuration. The annulus is of width D and inner radius R . The angular position is defined by angle θ . The detonation is initiated by a high pressure region shown as the dark region at the bottom of the charge and the solid thick lines represent the detonation front. The square and circular points represent the electrical pins used to measure detonation arrival times in the Lyle experiment.

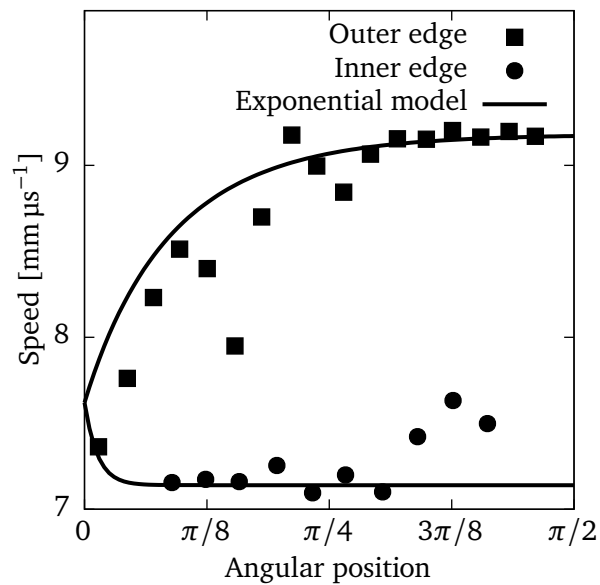


Figure 3.2: Experimental measurements of detonation speeds along the outer and inner boundaries of the explosive annulus adopted from the Lyle experiment [6]. The black curves correspond to the exponential model suggested by Souers et al. [6] to describe the evolution of the detonation speed along the annulus.

3.1. Introduction

condition translates to

$$W_s = \left(1 + \frac{D}{R}\right) V_s, \quad (3.1)$$

where R and D are the inner radius and width of the arc respectively, as depicted in figure 3.1. It is evident that depending on the ratio of width to radius, steady state velocity measured along the outer edge of the charge can have a significantly larger magnitude than at the inner edge.

There is a fundamental difference in the nature of speeds measured along the inner and outer edge of the annulus. At the inner edge, the detonation front velocity is tangent to the boundary of the annular charge and the measured speed is the actual speed at which the detonation propagates along that edge. However, the detonation velocity at the outer edge is not tangent to the boundary of the annulus and does not propagate along the outer boundary. Instead, the outer edge of the detonation at any moment has originated from a previously interior part of the detonation front. Thus, the measured speed is an apparent speed that the detonation front exhibits along the curve defined by the outer boundary as if it is moving across it. This explains why the speed measured at the outer boundary can be significantly higher than the ideal CJ velocity, which would otherwise be considered not physical for self-propagating detonations.

The transition phase is defined as the period beginning when the detonation enters the annular section until steady state is reached. The inner part of the detonation reaches steady state earlier than the outer part which has a longer transition phase, as can be seen from the results of the Lyle experiment in figure 3.2.

Although the dynamics of the detonation wave during the transition phase are not completely understood, it is suggested to involve a process where equilibrium is achieved through an energy flow across the detonation front [35]. Souers et al. [6] suggest that the evolution of the inner and outer speeds during the transition to steady state follows an exponential function of time given by

$$u(t) = U_s + (u_s - U_s) \left(1 - \exp\left(\frac{-t}{\tau}\right)\right), \quad (3.2)$$

where u is the wave speed at either edge, u_s is the corresponding steady speed, U_s is the steady speed in the straight section and τ is a time constant. The time constant is different for the inner and outer edge and it determines the extent of the transition period. It is derived by approximating the speed of sound as three quarters of the

steady detonation speed in the straight section and is given by

$$\tau = \frac{4\Delta D}{3U_S}, \quad (3.3)$$

where ΔD is the distance of the corresponding edge from the leading peak of the detonation front. Plots of the exponential functions that are suggested to describe the detonation front speed at the inner and outer edge of the explosive charge are shown in figure 3.2.

The uncertainty in the measurements of the Lyle and Hayes experiments is not provided in the work of Souers et al. [6] but is assumed to be significant since several parts of the data show unphysical behaviour. The outer speeds show oscillations during the transition phase which have not been observed in any of the related experiments and there is no indication of a physical mechanism that would lead to such instabilities during the acceleration of the detonation front. The inner speeds also show oscillating behaviour, but at a later time, well after the detonation has reached steady state. This also has no physical basis since the detonation is steady in that region. In fact, the original study ignores the last three points of the inner velocity and the steady inner velocity is calculated from the steady outer velocity and the condition of constant angular speed of the detonation. Overall, these oscillations are not considered physical and are caused by imperfections of the experimental apparatus which are further amplified by the numerical calculation of the speed of the detonation.

The large uncertainty in the experimental data also hinders the assessment of the exponential model for the evolution of the detonation speed during the transition phase. Nevertheless, the curve defined by the model is consistently above the experimental data for the transition phase, as can be seen in figure 3.2, which suggests an overprediction of the outer detonation front speeds. In addition, the exponential form of the model is an assumption that is not based on any physical considerations. These two facts raise doubts about whether the exponential model is the true description of the transition phase of the detonation.

Detonations in annular charges have also been investigated by a number of numerical studies. Short et al. [33] studied steady solutions of the DSD model for a 2D annular charge using both numerical methods and asymptotic analysis. The results showed a multi-layer structure of the detonation and determined the dependence of angular speed and front structure on the size of the annulus and on different degrees of confinement. The analysis distinguishes between thin and thick arcs where different approximations are made for the ratio of width to inner radius. For thick arcs, the steady angular speed

3.1. Introduction

corresponds to the Huygens limit with correction terms which depend only on the inner confinement.

Souers et al. [6] compared results from the Lyle and Hayes experiments against numerical simulations using LLNL production codes VHEMP with program burn and DYNA2D with the Ignition and Growth reaction rate model. The simulations were performed with a resolution of $\Delta x = 500 \mu\text{m}$ at most and show good agreement with the experimentally measured times to steady state. However, detonation speed is overestimated by VHEMP and underestimated by DYNA2D and detonation fronts have larger curvatures compared to the experimental results.

Similarly, Vágenknecht and Adamík [36] performed three-dimensional numerical simulations of the same experiments using LS-DYNA and the beta burn model. They used a resolution of $\Delta x = 500 \mu\text{m}$ and reported good agreement with the experimental detonation front curvature parameters but they also under-predicted the steady speed values compared to the experiment. Tarver and Chidester [37] used the Ignition and Growth model and a resolution of $\Delta x = 50 \mu\text{m}$ to simulate several of the aforementioned experiments on detonations in annular charges. The focus was on the steady state speeds of the detonation front for which they showed good agreement with experimental data.

The work presented here extends on the outcomes of previous studies on detonations in annular charges. It uses direct numerical simulations to present a complete description of the propagation of detonation along the annular arc. Particular focus is given to the transition phase and the identification of the effects that govern the evolution of the detonation wave during this phase.

The numerical solution is used to calculate the detonation speed along the inner and outer edge of the annular charge with respect to angular position and to time. The steady state speeds show good agreement with experimental results. However, the evolution of outer detonation speed during the transition phase deviates from the suggested exponential model. We propose a new description of the transition phase and show that it can be divided into two regimes. In the first regime, the outer detonation speed is governed by local effects at the outer boundary which lead to a dependence of detonation speed on angular position. In the second regime, effects originating from the inner boundary reach the outer edge and bring the detonation to steady state.

This work concludes with a parametric study where the inner radius and width of the annular charge are varied. This reveals the dependence of the transition phase and the steady state on the dimensions of the annular arc. We show that the reciprocal steady angular velocity has an affine relation with inner radius of the arc which was

3.2. *Mathematical model and numerical solution*

also observed by Lubyatinsky et al. [7]. The dependence of the extent of the transition phase on the dimensions of the annular charge is studied in terms of angle and time to steady state. Both increase with width, whereas larger radii lead to a decrease of the angle at which steady state is reached. In terms of time, there is opposing behaviour between configurations of small and large widths. The transition duration increases with radius for large widths but decreases for smaller widths.

The system is modelled using the recently proposed diffuse-interface method of Michael and Nikiforakis [20]. The explosive considered is LX-17 (92.5% TATB, 7.5% Kel-F) which makes the results directly comparable to the Lyle and Hayes experiments [6]. It is modelled using two JWL equations of state and the Ignition and Growth reaction rate law [2]. This choice was facilitated by the existence of widely used sets of parameters for the particular explosive, as well as by the availability of accessible experimental data that can be used to validate the mathematical model and implementation of the numerical methods.

Particular care was given in ensuring that the numerical simulations are adequately resolved because the phenomenology of the Ignition and Growth model depends on the resolution of the computations. This is facilitated by the use of a parallel, hierarchical, block-structured adaptive mesh refinement framework.

3.2 Mathematical model and numerical solution

The physical system considered in this chapter is modelled with the hybrid multiphase formulation which was described in chapter 2. The reactive material is the explosive LX-17 and the inert is air. These are modelled with the JWL EOS, presented in 2.5, and the ideal gas EOS respectively. The parameter set for the aforementioned materials along with the reference values for the non-dimensionalization of the equations are presented below. The section concludes with the description of the procedure followed to detect the position of the detonation front from the simulation output.

3.2.1 Data set and non-dimensionalization

The parameter sets found in literature for the equation of state and reaction rate of a particular explosive can often vary. The variation is attributed to the different experiments to which the parameters were fitted but also to the particular process that the parameter set intends to model. The data set for the explosive LX-17 used in this study is taken from the work of Tarver [24] and has been used in similar studies [23, 25].

3.2. Mathematical model and numerical solution

Parameters	LX-17	
	Reactants	Products
Γ_0	0.8938	0.5
A [10^{11} Pa]	778.1	14.8105
B [10^{11} Pa]	-0.050 31	0.6379
R_1	11.3	6.2
R_2	1.13	2.2
c_V [$\text{m}^2 \text{s}^{-2} \text{K}^{-1}$]	1305.5	524.9
Q [$10^6 \text{m}^2 \text{s}^{-2}$]	0	3.94
ρ_0 [kg m^{-3}]	1905	1905

Table 3.1: JWL EOS parameters for LX-17 [24].

The parameters for the JWL EOS are shown in table 3.1 and the reaction rate parameters in table 3.2. This set is suggested to be more suitable for detonation propagation rather than initiation [24].

The equation of state and reaction rate parameter sets are often given in a non-dimensional form, where particular parameters related to the application are used as reference values in the non-dimensionalization process. Following the example of Kapila et al. [23] we use the CJ detonation speed of the explosive as one of the reference values. This is calculated analytically using the CJ theory [38]. The reference values used for non-dimensionalization are

$$\begin{aligned}
 \rho_0 &= \rho_{\text{ref}} = 1905 \text{ kg m}^{-3} \\
 D_{\text{CJ}} &= u_{\text{ref}} = 7.6799 \text{ mm } \mu\text{s}^{-1} \\
 t_{\text{ref}} &= 1 \text{ } \mu\text{s}.
 \end{aligned} \tag{3.4}$$

From the above, the reference values for the rest of the flow variables can be calculated as

$$\begin{aligned}
 \rho_0 D_{\text{CJ}}^2 &= p_{\text{ref}} = 112.359 \text{ GPa} \\
 D_{\text{CJ}}^2 &= e_{\text{ref}} = 58.98 \text{ mm}^2 \mu\text{s}^{-2} \\
 D_{\text{CJ}} t_{\text{ref}} &= l_{\text{ref}} = 7.6799 \text{ mm}.
 \end{aligned} \tag{3.5}$$

3.2. Mathematical model and numerical solution

	\mathcal{R}_{ig}		\mathcal{R}_{G1}		\mathcal{R}_{G2}	
I [s^{-1}]	4.0×10^{12}		G_1 [$\text{GPa}^{-3} \text{ms}^{-1}$]	4500	G_2 [$\text{GPa}^{-1} \text{ms}^{-1}$]	30
a	0.22	b	0.667	c	0.667	
d	1	e	0.667	g	0.667	
x	7	y	3	z	1	
ϕ_{ig}	0.02	ϕ_{G1}	0.8	ϕ_{G2}	0.8	

Table 3.2: Ignition and Growth parameters for LX-17 [24].

3.2.2 Detonation front detection

This study focuses on the analysis of the speed of a detonation wave and therefore, it requires accurate detection of the wave front and calculation of its speed. The position of a detonation front in the simulation output can only be accurate to within one grid cell at best. In addition, the use of a shock capturing numerical method means that discontinuities are smeared over a few grid cells which introduces additional uncertainty in the position of the shock.

The algorithm used in this study for detecting shock position from the numerical solution relies on the large pressure gradients across shock waves compared to the rest of the domain. After every time-step, the normalized gradient of pressure is calculated for every cell. The position and state of cells that are above a predefined threshold

$$\frac{\|\nabla p\|}{p} > 10, \quad (3.6)$$

are output along with the simulation time. The extracted cells are then grouped into cells that are at the same distance from the centre of the annulus within a range of the cell size Δx . The positions of all cells in a group are then averaged and the calculated points mark the detonation front position. The obtained data will unavoidably have an error variance of a few computational cells but the above method provides a consistent way of detecting front location which does not depend on how the discontinuity is smeared over the cells.

The values of position over time are then used to calculate the instantaneous speed of the detonation using a central differences scheme. The calculation of derivatives from experimental or simulation data greatly increases the noise levels in them. Thus, the stencil used in this scheme is chosen to be wide, using up to ten data points in each

3.3. Validation and grid convergence

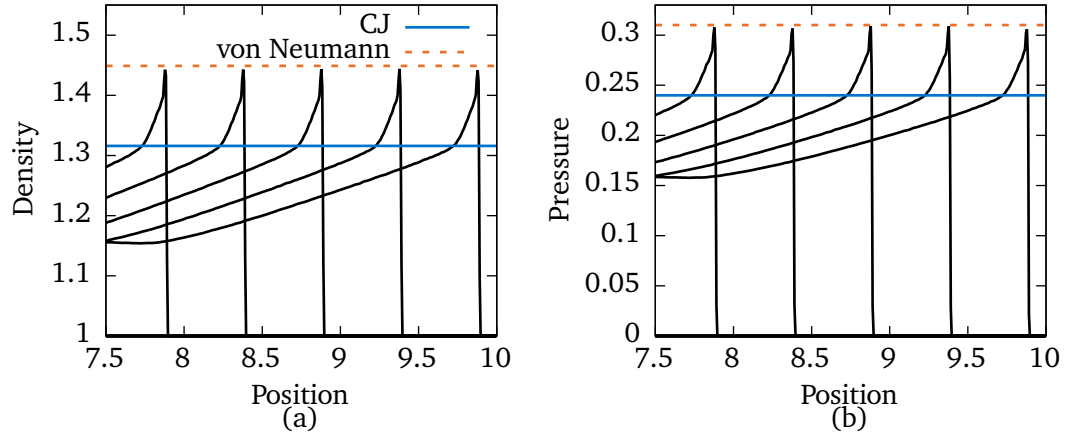


Figure 3.3: The numerical solution of the one-dimensional steady detonation in LX-17. The results are plotted at constant time intervals of $t = 0.5$. The horizontal lines represent the analytically calculated values at the CJ and von Neumann points.

direction in order to provide a smooth representation of the detonation front speed.

3.3 Validation and grid convergence

The mathematical model and implementation of the numerical methods are assessed through a series of test problems to ensure their validity and suitability for the considered application. These include the study of the one-dimensional steady detonation and of the diameter effect in cylindrical charges. In addition, a grid convergence study is performed to establish the resolution for which the solution has sufficiently converged.

3.3.1 One-dimensional steady state detonation

We consider the numerical solution of a one-dimensional steady detonation. The structure of the detonation wave is described by the ZND detonation model [38]. Characteristic quantities, such as the states at the von Neumann and CJ points are calculated analytically and are used to verify the implementation of the model.

The setup is one-dimensional and contains the explosive only. The initial conditions consist of a small region of high pressure placed at the left end of the domain and the rest of the explosive is at ambient conditions. The pressure in the high pressure region is set to 0.24 (27 GPa) which is close to the expected CJ pressure of the explosive. This causes the rapid expansion of the explosive in this region, which compresses and ignites the explosive ahead, leading to the quick formation of a steady detonation wave.

3.3. Validation and grid convergence

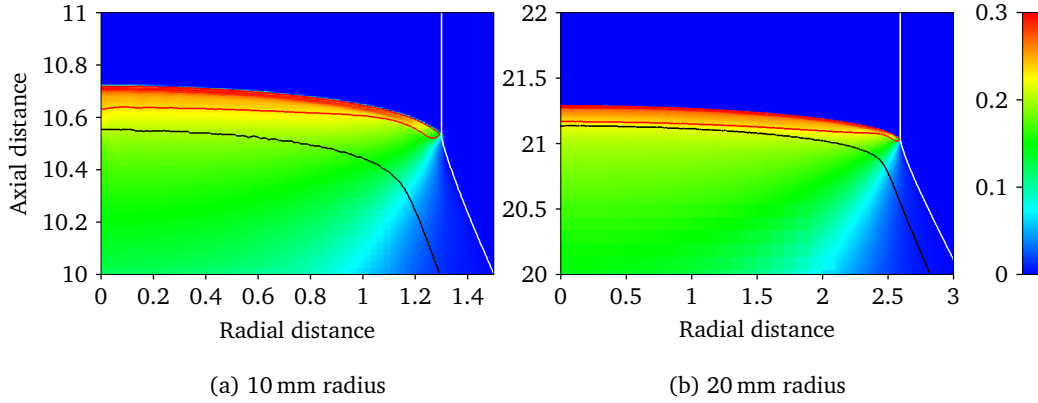


Figure 3.4: Pressure plots of the structure of steady detonation waves propagating in cylindrical charges of different radii. The white line is the explosive-air interface, the black line corresponds to the reaction zone end (RZE) and the red line to the sonic locus which outlines the detonation driving zone (DDZ).

The numerical solution of the one-dimensional detonation wave is shown in figure 3.3 for a resolution of $\Delta x = 6.25 \times 10^{-3}$. The solution is presented in a series of density and pressure plots, for times after the detonation has settled to steady state. The von Neumann and CJ points of the numerical solution match the values calculated analytically.

3.3.2 Steady detonation in cylindrical charges

The two-dimensional implementation is validated using an unconfined rate stick configuration. The configuration is three-dimensional axisymmetric and is solved in a two-dimensional domain with the addition of geometric source terms. Each rate stick is defined by its radius R and has a length of $L \approx 10R$ which was found to be sufficient for the detonation to settle to steady state before it reaches the end of the charge. The detonation is initiated through a region of high pressure, similar to the case of the 1D steady detonation.

A base grid resolution of $\Delta x = 0.1$ is used, with two levels of refinement, each with a refinement factor of 4, yielding an effective resolution of $\Delta x = 6.25 \times 10^{-3}$. It was ensured that the solution has converged by performing a convergence study, as presented in section 3.3.3 for the case of annularly shaped charges.

The numerical solutions of steady state detonation in rate sticks of radius 10 mm and 20 mm are shown in figure 3.4. As the detonation wave propagates, the explosive products expand against the surrounding material which results in a diverging flow as

3.3. Validation and grid convergence

evidenced by the position of the explosive-air interface. Also depicted is the reaction zone end (RZE) locus, defined as the contour $\lambda = 0.001$ and the sonic locus, defined as the curve which satisfies

$$M \equiv \frac{\|\mathbf{v}\|}{c} = 1,$$

where \mathbf{v} is the flow velocity in the frame of the detonation and c is the local speed of sound.

The sonic locus outlines the region behind the shock in which the flow is subsonic and is often referred to as the detonation driving zone (DDZ). Outside the DDZ, the flow is supersonic and does not influence the propagation of the detonation. In the steady detonations of figure 3.4, the sonic locus intersects the detonation front and not the explosive-air interface. This means that the detonation wave is completely decoupled from the surrounding material because the flow along the explosive-air interface is supersonic. This classifies the configuration as unconfined, since the surrounding material has no effect on the propagation of the detonation.

The sonic locus being inside the reaction zone is characteristic of the diverging flow in charges of finite radius. This results in some of the chemical energy released in the reaction zone not being supplied to the detonation front. In charges of smaller radius, the curvature of the detonation front increases and the sonic locus moves further away from the RZE which results in the DDZ covering less of the reaction zone region. This translates to even less energy being used to drive the detonation wave and gives rise to the diameter effect in which the detonation slows down as the radius of the charge decreases and eventually leads to detonation failure. The difference in the position of the sonic locus with respect to the RZE for rate sticks of different radii can be seen in figure 3.4.

To assess the suitability of the mathematical model in capturing the dependence of detonation speed on charge radius, we compare the numerical results of detonation speeds against experimental results. The experiments were performed at the Lawrence Livermore National Lab [39] and used LX-17 charges confined by thin shells of either copper or PMMA, as well as bare charges. They measured the average detonation speed over the last third of the charge in which the detonation is assumed to be in steady state. The PMMA shells had thickness between 1 mm – 3.25 mm which is at most 25% of the charge radius. These configurations are considered unconfined and are used to compare against the results of the numerical simulations.

The experimental and numerical detonation speeds can be seen in figure 3.5. The diameter effect curve obtained from the numerical solution is concave downwards

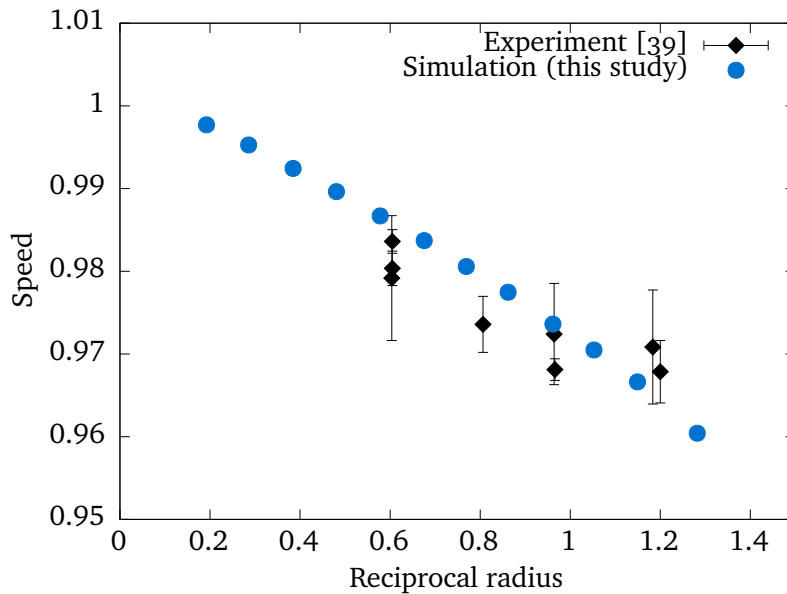


Figure 3.5: Numerical and experimental [39] steady detonation speeds over reciprocal radius for unconfined cylindrical LX-17 charges.

which is typical of heterogeneous condensed phase explosives [40]. The numerical detonation speeds are within the range of values of the experiment. The calculated failure radius is between 5.5 mm – 6 mm which agrees with the numerical results from Tarver and McGuire [41] and with their reported experimental value of 6 mm. The large error margins of the experimental values do not allow for assessing the accuracy of the numerical results. Experimental measurements of higher accuracy are required for a more conclusive validation of the model and parameters. Nevertheless, this test establishes the ability of the model to capture the diameter effect for condensed phase high explosives.

3.3.3 Convergence study

The use of sufficient resolution for the computations is essential in capturing the phenomenology of the Ignition and Growth model. If the reaction zone is not adequately resolved, it does not exhibit the intended phenomenological description of the reaction processes in the explosive and leads to critical loss of accuracy in the solution. Bdzil et al. [31] studied a simplified pressure-based reaction rate law and determined that predicting the detonation speed of a straight cylindrical charge within 1 m s^{-1} of the actual value requires 50 or more cells in the reaction zone.

3.3. Validation and grid convergence

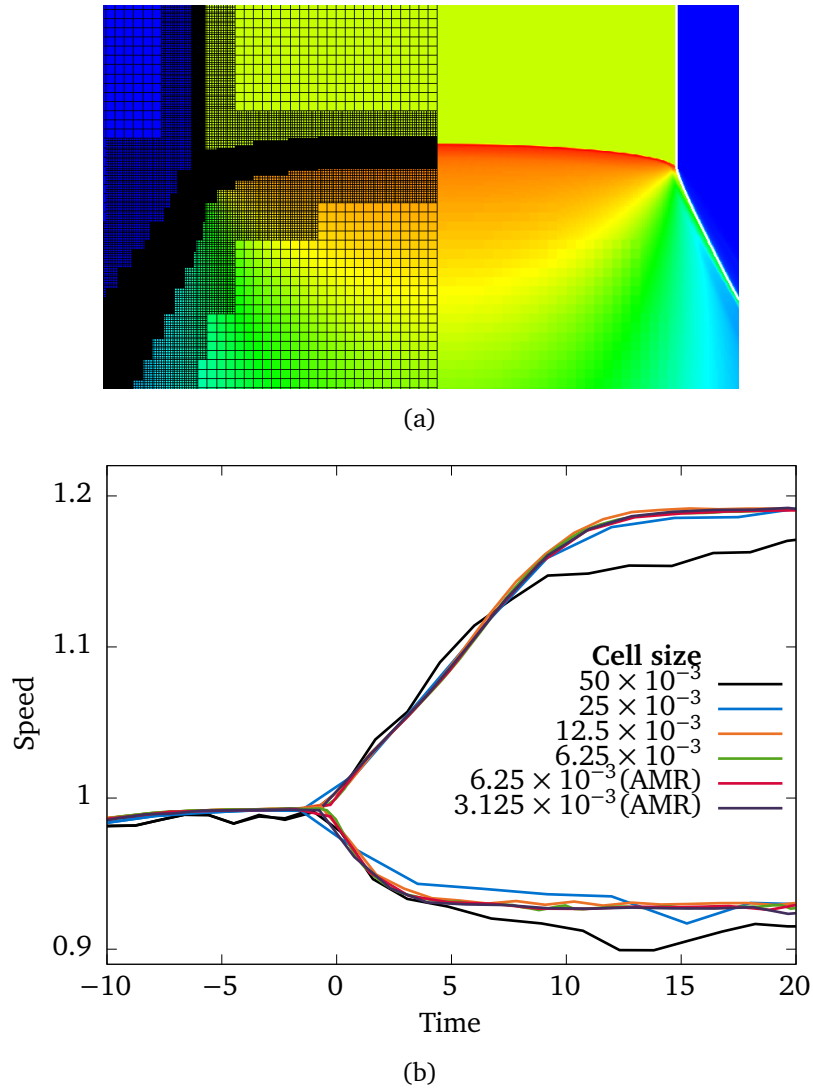


Figure 3.6: Convergence and AMR coverage study for the annular arc configuration. (a) Depiction of two levels of AMR covering the detonation front and material interface. (b) Detonation speed over time at the inner and outer boundary of the explosive, calculated from solutions of increasing resolution.

3.3. Validation and grid convergence

The convergence of the numerical solution is assessed by examining the detonation speed over time for a series of simulations of increasing resolution. We use the annular charge configuration and the detonation speed is calculated along the inner and outer parts of the charge. The domain boundary conditions are set to transmissive [28] to allow for waves to exit the domain without any effect on the flow inside. This condition is not perfectly satisfied in multi-dimensional problems and partial reflections occur which influence the flow inside the domain. Thus, we ensured that the domain boundaries are sufficiently far as to not influence the reaction zone and interfere with detonation propagation.

The initial resolution is set to $\Delta x = 0.05$ which corresponds to $384 \mu\text{m}$ and is halved for every subsequent simulation. In addition, we ensure sufficient coverage of the important regions by the adaptive mesh refinement (AMR) process. This is done by comparing the numerical solution obtained using a uniform grid with one that used an AMR grid at the same effective resolution. The refinement criterion is set using the density gradient, i.e.

$$\frac{\|\nabla\rho\|}{\rho} > 1.$$

This results in refining the detonation front and the reaction zone, as well as the interface between the explosive and air due to the sharp density difference between the two materials.

Figure 3.6 shows the speed of the detonation wave over time at the inner and outer edge of the explosive charge for the set of resolutions used. The solution gives indistinguishable detonation speeds for resolutions higher than $\Delta x = 6.25 \times 10^{-3}$ ($48 \mu\text{m}$) which is the resolution selected for this study. Moreover, identical solutions are also obtained when utilizing AMR which ensures that the refinement criterion results in sufficient coverage of the appropriate regions.

Having validated the mathematical model and the numerical algorithms we now turn to the study of the propagation of detonations in annularly shaped explosive charges. The configuration is as shown in figure 3.1 and consists of an unconfined explosive charge of rectangular cross section with a straight and an annular section. The annular arc extends to 90° and is defined by the inner radius R and width D . We assume that the explosive charge is sufficiently long in the direction of the axis of curvature to allow modelling the system as two-dimensional.

The explosive is ignited by the rapid expansion of a high pressure region placed at the low end of the straight charge. This leads to the quick formation of the detonation wave, which reaches steady state in the straight section and subsequently enters the

3.4. The Lyle and Hayes experiments

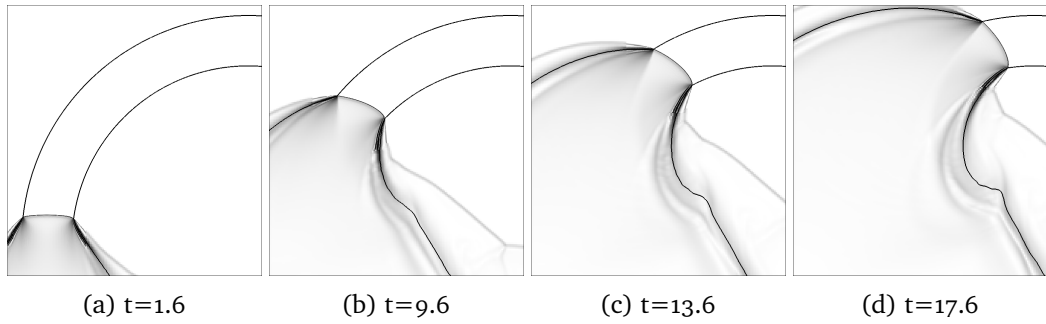


Figure 3.7: Density gradient plots of the propagation of a detonation wave in an annularly shaped explosive. The dark lines represent the interface between explosive and air as well as the detonation wave front. The shock developed in the air is shown with a lighter shade. The charge is of radius $R = 11.578$ and width $D = 3.308$ which corresponds to the Lyle experiment.

annular section of the explosive charge. The detonation speed is measured along the edges of the annulus and angular position is given by angle θ , also shown in figure 3.1.

3.4 The Lyle and Hayes experiments

We initially study the configurations used in the Lyle and Hayes experiments [6] for which experimental results are available. These used unconfined LX-17 charges of different dimensions. The Lyle experiment had an annular charge of inner radius $R = 88.9$ mm and width $D = 25.4$ mm, while the Hayes configuration had $R = 63.5$ mm and $D = 38.1$ mm. The straight section was of length $L = 116$ mm, which allowed enough travel distance for the detonation to reach steady state before entering the annular section.

Figure 3.7 shows density gradient plots of the detonation wave propagating in the annular section of the explosive for the case of the Lyle configuration. These plots highlight the interface between the explosive and air as well as the detonation wave front. The shock wave in air is shown with a lighter shade. The results show the development of an apex in the explosive-air interface. This is an effect of the different geometry between the straight and annular sections. A steady detonation wave exerts a constant force on the interface in the direction normal to the interface. In the straight section this keeps the interface straight, whereas in the annular section each point of the interface is pushed in a different direction and the resulting interface is curved. Thus, an apex develops at the point where the charge geometry changes.

3.5. *The effect of the boundaries of the annular charge*

The detonation wave is initiated and propagates steadily in the straight section at a constant speed. As it enters the annular arc every part of the front has the same linear speed and hence the outer segments have lower angular velocity compared to the inner parts. Thus, the inner parts propagate faster along the arc. This results in the deformation of the shape of the front with its peak shifted towards the inner wall. Figure 3.8 shows the evolution of the detonation front for the configuration of the Hayes experiment. The curvature of the detonation front shape increases during the transition period until steady state is reached, in which the front moves at constant angular velocity and maintains its shape.

Figure 3.9 shows the numerical results for the speed of the detonation wave along the inner and outer boundaries of the annular charge against the experimental values and the exponential time-dependent model suggested by Souers et al. [6]. The inner part of the detonation moves to steady state quicker than the outer part, which has a larger transition period, consistent with the experimental results. The steady state values of the speeds are also matched well. However, the numerical results do not follow the exponential description of the transition phase. The speed at the inner edge follows a slower exponential decay than predicted by the model. At the outer edge, the detonation speed exhibits multiple stages of distinct behaviour. There is a short initial period where the speed increase appears to be linear. Then the detonation exhibits increasing acceleration and eventually, the acceleration decreases until zero where the detonation has reached constant steady state speed.

This behaviour is notably different to the exponential model and is also within the scatter of the experimental points. However, the comparison with the experimental results cannot not affirm that the observed behaviour is a more accurate description than the exponential model due to large uncertainties in the experimental measurements. A more definite assertion requires higher quality experiments that make use of more accurate techniques for the determination of the characteristics of detonation propagation in annular arcs.

3.5 The effect of the boundaries of the annular charge

The study of the Lyle configuration indicates that the evolution of the detonation speed deviates from the suggested exponential model. This section provides further analysis of the transition phase by considering the physical processes involved and examining the effect of each of the two boundaries of the annular charge separately.

We consider two test cases where one of the two boundaries of the two-dimensional

3.5. The effect of the boundaries of the annular charge

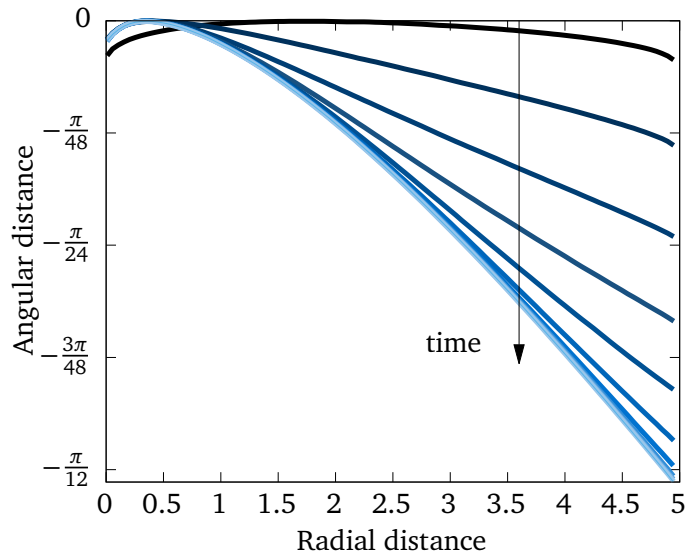


Figure 3.8: Evolution of the detonation front for the Hayes configuration. The fronts are shown at constant time intervals starting when the detonation enters the annular section (black) and move from dark to light colour as time progresses. Radial distance is measured from the inner edge of the charge and angular distance from the leading peak of the front.

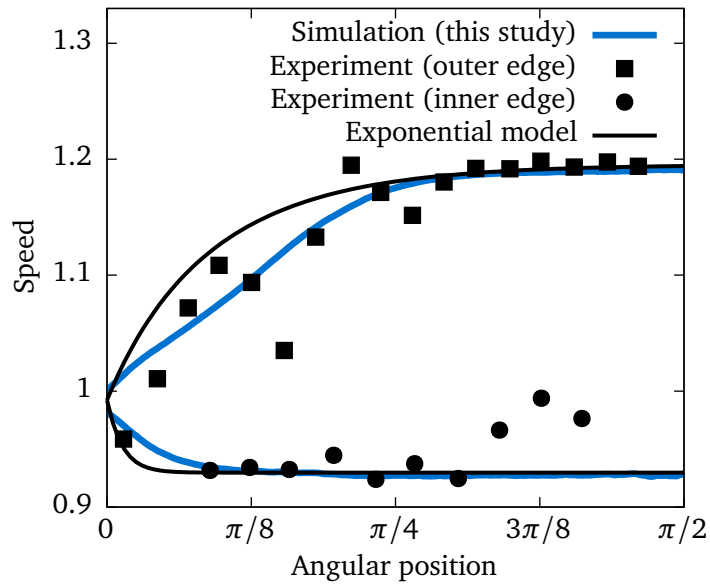


Figure 3.9: Detonation speeds at the inner and outer edge of the annular charge calculated in this numerical study along with experimental results and the exponential model suggested by Souers et al. [6]. The speeds are plotted against angular position θ defined in figure 3.1.

3.5. The effect of the boundaries of the annular charge

annular charge is removed and the remaining space is filled with the explosive. This results in a semi-infinite explosive charge with a single edge, as shown in the illustrations of figure 3.10. The configurations also include a straight section where the detonation is initiated and left to reach steady state. In both test cases, we calculate the speed of the detonation wave along the curve defined by the outer boundary of the original arc configuration. These curves are illustrated in figure 3.10 and the resulting detonation speeds for each test case are shown in figure 3.11.

In the case of inner-only boundary, the detonation along the outer curve initially accelerates at an increasing rate. It then reaches an inflection point and the acceleration decreases until it becomes zero and the detonation travels at constant speed. The evolution of the detonation speed in this case can be divided into two regimes based on the physical processes involved. The change of geometry at the inner edge alters the detonation dynamics and its effects travel along the front at a finite speed. The first regime corresponds to the period before the effects from the inner boundary reach the outer part of the detonation front. An inflection point signals the start of the second regime where the inner boundary effects have reached the outer part and progressively move the detonation to steady state.

During the first regime, the outer part of the detonation is yet to be affected by the changes in the geometry of the explosive charge and the change in detonation speed is a result of local effects at the curve representing the outer boundary of the original configuration. A mathematical description of the first regime can be deduced by considering that the detonation wave during this period is simply a plane wave propagating in the direction normal to the front. Assuming a constant straight section speed U_S , the speed measured along the curve defined by the outer boundary W will follow

$$W = U_S \sec \theta, \quad (3.7)$$

where θ is the angular position along the arc. Hence, the measured speed is not the actual speed at which each part of the detonation front propagates in the explosive, but rather the rate at which the detonation front reaches the curve as it travels across it.

In the second regime, the effects from the inner boundary reach the outer part causing a change in the curvature of the detonation front and in the direction of propagation. This results in the observed decrease in the acceleration of the detonation which eventually reaches steady state.

In the case of outer-only boundary, the speed exhibits an initial stage where it appears to increase linearly. This is followed by a stage of increasing acceleration of the

3.5. The effect of the boundaries of the annular charge

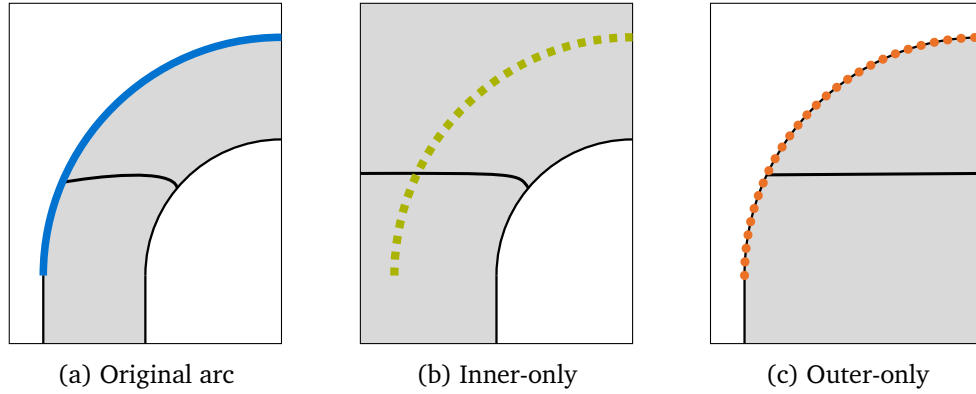


Figure 3.10: Depiction of the original annular configuration and of the test cases devised to examine the influence of the boundaries of the annulus. The shaded area represents the explosive and white space is air. Detonation speed measurements are made along the curves defined by the thick lines and are pattern and colour coded to match the plots of figure 3.11.

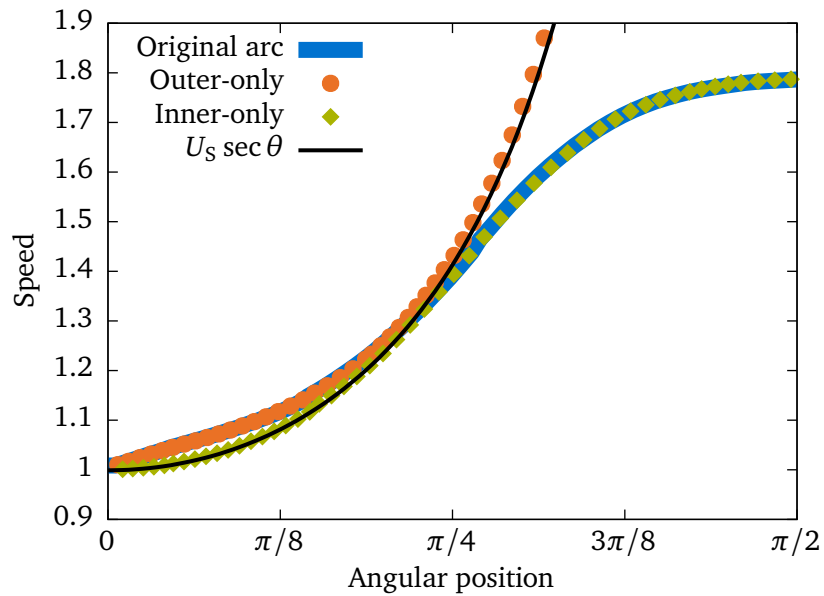


Figure 3.11: Detonation speed over angular position for the devised test cases and original annular arc setup. The configuration is of radius $R = 6.616$ and width $D = 6.616$.

3.5. *The effect of the boundaries of the annular charge*

detonation leading to very high speeds. The detonation front is flat and travels at the same direction as in the straight section.

We expect the propagation of the detonation wave in the outer-only case to be similar to the first regime of the inner-only boundary configuration because in both cases the front propagates at a constant velocity and measurements are taken along a 90° arc. Hence, the detonation speed will follow equation (3.7). This is indeed seen in the second stage, but with an offset, because of the observed linear increase in detonation speed during the initial stage.

The existence of the initial stage is attributed to the curvature of a small segment of the detonation front next to the outer boundary of the straight section. As discussed in section 3.3.2 the front of a steady detonation in charges of finite size is curved and its curvature depends on the diameter of the charge. In the case of outer-only boundary, the explosive charge is semi-infinite and the detonation front has a small curved segment only at the edge of the charge while the rest is flat. Due to this convex curvature, the front reaches the outer boundary faster than if it were flat, resulting in the observed linear increase. The fact that this curvature is limited to a small segment of the front next to the boundary means that only a short initial stage is influenced by it.

The detonation speed along the outer boundary for the original annular configuration is also shown in figure 3.11. Based on the test case of inner-only boundary, we again distinguish between two regimes in which the change in detonation speed is caused by different effects. The first regime is caused by local effects at the outer boundary of the annular charge. This leads to the behaviour seen in the case of outer-only boundary, where the outer detonation speed depends on angular position; it increases linearly at first and then as $\sec \theta$. The second regime is induced by the effects of the inner edge. When these reach the outer edge of the annulus, the outer speed goes through an inflection point and the acceleration of the detonation decreases until it reaches constant steady state speed in a way that exactly follows the second regime of the inner-only test case. This shows that steady state is caused solely by the effects originating from the inner edge. Similar findings have been reported by the asymptotic analysis of a DSD model [33]. In the thick arcs approximation $D/R \sim \mathcal{O}(1)$, the dependence of steady angular velocity on inner radius and degree of inner confinement is caused by a small boundary layer region along the inner arc surface. Also, the outer radius and degree of confinement do not enter in any terms that determine the steady angular velocity.

3.6. The effect of the dimensions of the annular charge

Radius	6.616	8.27	9.924	11.578	13.232
Width	1.654	3.308	4.962	6.616	

Table 3.3: The values for inner radius and width used in the parametric study to study the effect of the dimensions of the annulus

3.6 The effect of the dimensions of the annular charge

The dependence of detonation propagation on the dimensions of the annular charge is investigated through a parametric study in which the width and inner radius of the annulus are varied. A set of values for the radius and width are selected as multiples of the greatest common factor of the radius and width used in the Lyle and Hayes experiments. The set of values used is shown in table 3.3.

Simulations were performed for all twenty combinations of the values above. The obtained inner and outer speeds against angular position along the annular section are presented in two sets of figures. Figure 3.12 arranges the results in configurations of the same radius whereas the graphs of figure 3.13 correspond to configurations of the same width.

We note that stable detonation was observed in all configurations. Experiments with gaseous explosives performed on similar configurations showed unsteady propagation for certain configurations [34]. However, the minimum width employed in this study is double the failure radius of the considered explosive and any unsteady or failing detonation was not observed.

3.6.1 Steady state

We initially consider the steady state of detonation in annular arcs and investigate its dependence on the dimensions of the explosive charge. The plots of figure 3.12 show a clear increase of outer steady state speed W_S with width. The values are consistent with the condition of constant angular velocity given by

$$W_S = \kappa(R, D)V_S, \quad (3.8)$$

3.6. The effect of the dimensions of the annular charge

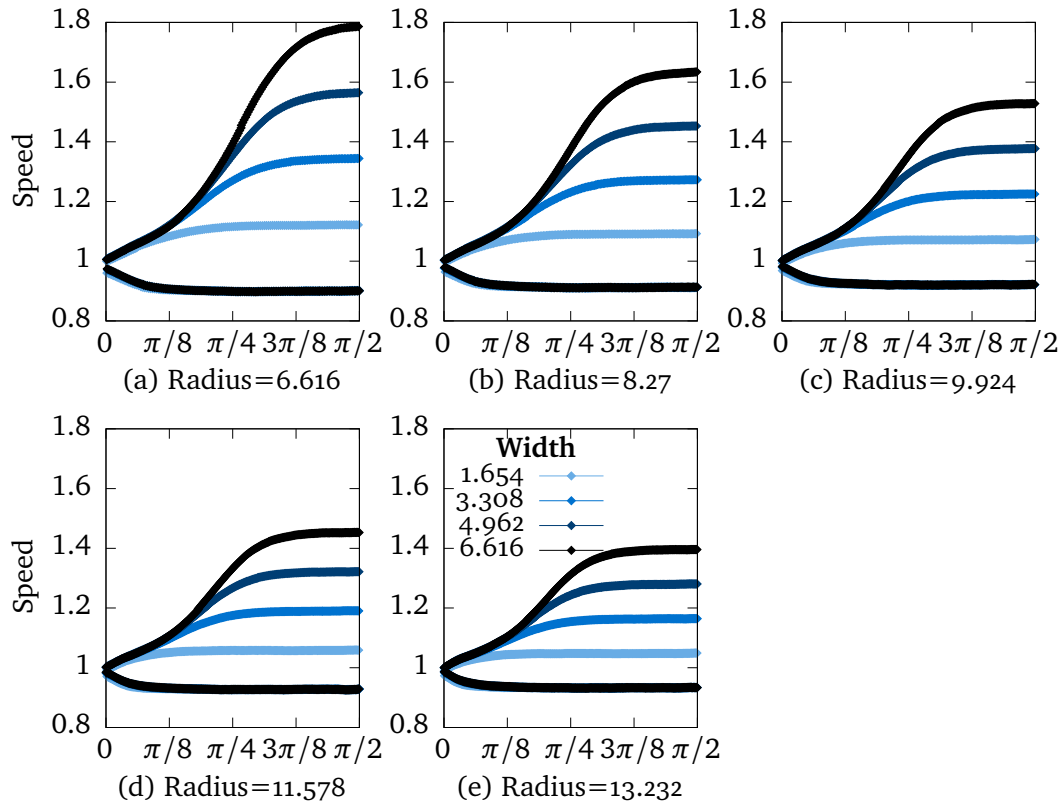


Figure 3.12: Detonation speeds over angular position along the inner and outer edge of the annular arc. The plots correspond to configurations of different radii in which the width varies from small (lighter colour) to large (darker colour).

3.6. The effect of the dimensions of the annular charge

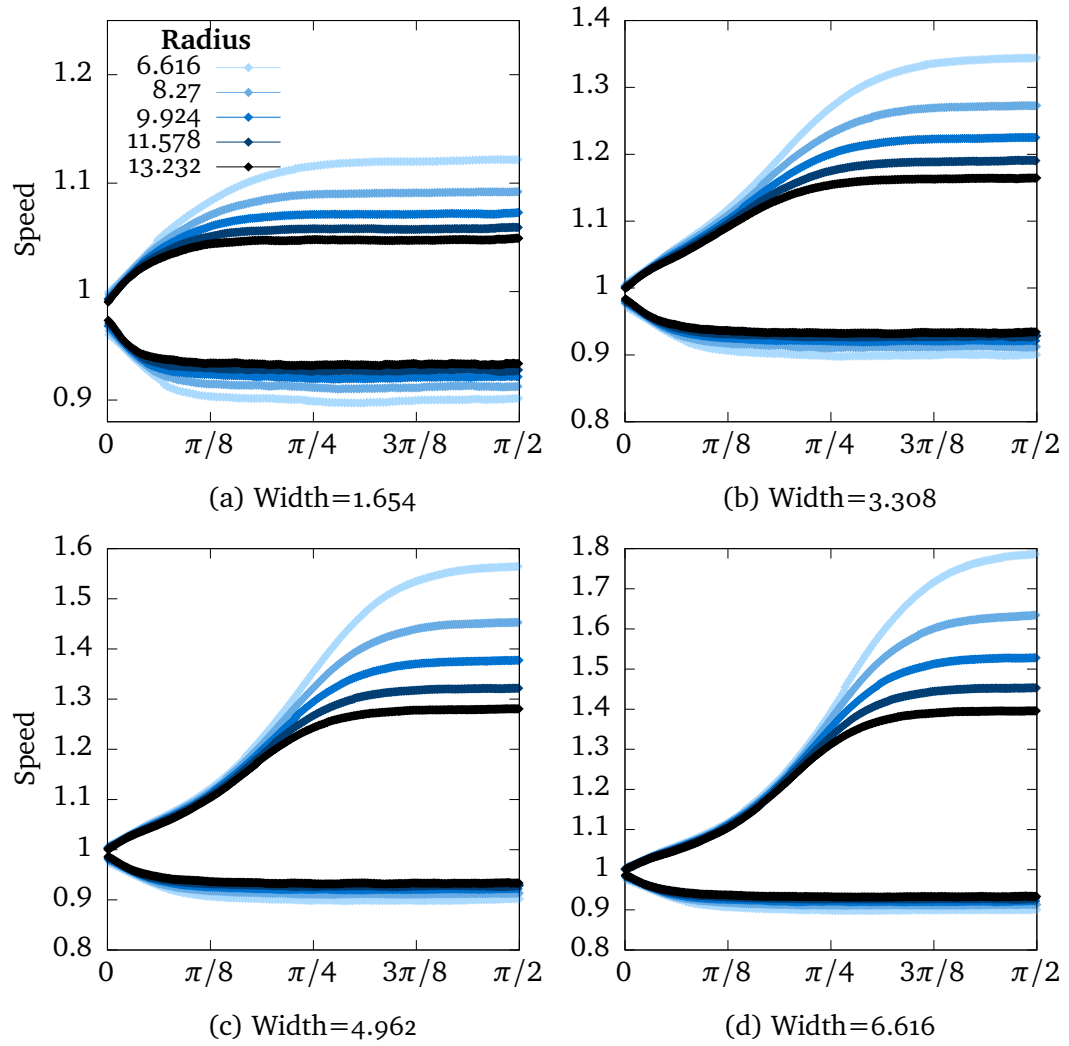


Figure 3.13: Detonation speeds over angular position along the inner and outer edge of the annular arc. The plots correspond to configurations of different width, in which the radius varies from small (lighter colour) to large (darker colour).

3.6. The effect of the dimensions of the annular charge

where V_S is inner steady state speed and κ is defined as the magnification coefficient which depends on the dimensions of the arc

$$\kappa(R, D) = 1 + \frac{D}{R}. \quad (3.9)$$

In contrast, inner steady speeds do not differ for explosive charges of different width and same radius. Despite the fact that steady detonation speed in the straight section increases with width due to the diameter effect, once the detonation reaches steady state in the annular section, the inner speed is the same for all configurations of the same radius. This implies that the steady state angular velocity, ω_S , is also independent of width since it can be expressed as

$$\omega_S \equiv \frac{V_S}{R}. \quad (3.10)$$

The independence of steady angular velocity on the outer radius is also seen in the asymptotic analysis of the DSD model performed by Short et al. [33] for arcs where $D/R \sim \mathcal{O}(1)$ as in this study.

The dependence of steady angular velocity on the dimensions of the annulus is seen in figure 3.14. Due to the independence of the angular velocity on width, configurations of the same width fall on the same point in the plot. Furthermore, we observe an affine dependence of the reciprocal angular velocity on inner radius which agrees with the results by Lubyatinsky et al. [7]. We perform a linear fit on the data using the model function

$$\omega_S^{-1} = \frac{R + \Delta_0}{D_\infty}, \quad (3.11)$$

and obtain the values

$$\begin{aligned} D_\infty &= 0.9707(11), \\ \Delta_0 &= 0.537(12), \end{aligned}$$

which are characteristic of the combination of explosive and confining material considered here. Parameter D_∞ represents the upper limit of detonation speed at the inner edge as $R \rightarrow \infty$. Parameter Δ_0 resembles the behaviour of failure thickness of a straight explosive slab because it decreases with increasing impedance of the confining material as reported by Lubyatinsky et al. [7].

Expression (3.11) allows for the relations between inner or outer steady state speeds and the dimensions of the annulus to be determined analytically. From figure 3.13 we

3.6. The effect of the dimensions of the annular charge

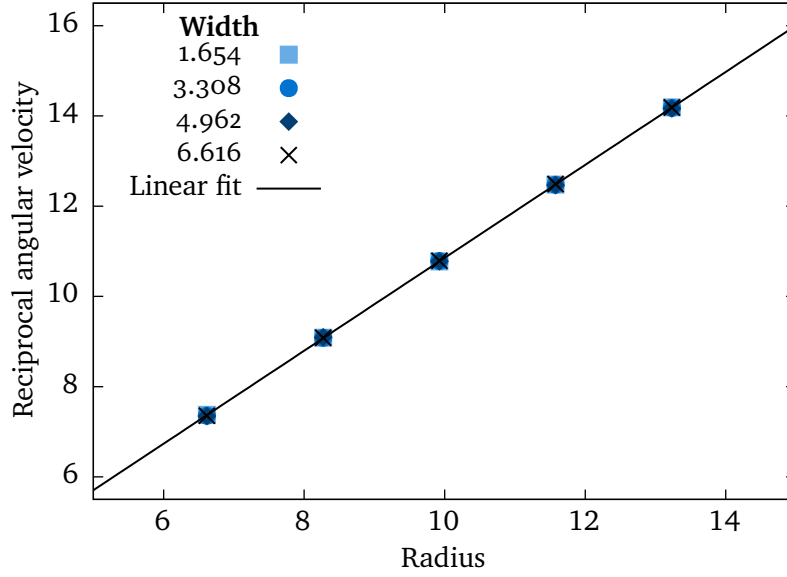


Figure 3.14: The reciprocal steady state angular velocity over inner radius for all studied configurations. These show an affine dependence of the reciprocal angular velocity on the inner radius of the annulus but no dependence on the width of the annulus.

can deduce that the inner steady state speed increases with arc radius,

$$\frac{dV_s}{dR} > 0. \quad (3.12)$$

Utilizing equation (3.11), we see that the above expression holds when $\Delta_0/D_\infty > 0$, which has to be satisfied to ensure positive angular velocity as $R \rightarrow 0$.

The dependence of the outer steady state speed on the annulus dimensions is also seen in the plots of figures 3.12 and 3.13. It increases with width

$$\frac{\partial W_s(R, D)}{\partial D} > 0, \quad (3.13)$$

and decreases with radius

$$\frac{\partial W_s(R, D)}{\partial R} < 0, \quad (3.14)$$

in contrast to the increase of steady inner speed (3.12). Combining relation (3.11) with the condition for constant angular velocity (3.8) shows that expression (3.14) holds when width is larger than a threshold,

$$D > \Delta_0. \quad (3.15)$$

3.6. The effect of the dimensions of the annular charge

For the explosive and confining material considered here this value is $\Delta_0 = 4.12$ mm and the condition holds for all configurations used in this study.

As expressed by (3.8), outer speed depends on the magnification coefficient and inner speed. These two quantities change with radius in opposite ways. The magnification coefficient decreases while the inner speed increases. Expression (3.15) means that when the width of the annulus is larger than a threshold, the magnification part of equation (3.8) is dominant and decreases more with radius than the inner speed increases, whereas the opposite applies for widths smaller than the threshold.

3.6.2 Transition phase

The transition phase is the period during which the detonation shifts from a steady state of constant linear speed in the straight section to a steady state of constant angular speed in the annular section. The inner part of the detonation front reaches steady state earlier than the outer edge of the front, which is the last segment to reach steady state speed and determines the extent of the transition phase.

The dimensions of the annulus influence the inner and outer speeds of the detonation front during the transition phase in different ways. Figure 3.12 indicates that configurations of different inner radius have qualitatively similar evolution of speeds whereas figure 3.13 shows distinct acceleration profiles of the outer detonation front for configurations of different width. In particular, configurations of larger widths demonstrate more pronounced local effects at the outer boundary and more extensive transition phases. The inner radius of the annulus only influences the last stage of the transition phase and leads to reaching steady state at smaller angles with increasing radius.

The extent of the transition phase is a function of the acceleration profile during the transition phase and of the difference between the steady speeds in the annular and straight section. Thus, its dependence on the dimensions of the annulus can be deduced from knowing the respective dependence of these two quantities. The dependence of steady speeds on the dimensions of the annulus is well understood and is presented in section 3.6.1, but the acceleration of the outer front is only known qualitatively, as discussed in section 3.5 and no exact function that describes the whole process is known.

We consider the extent of the transition phase in terms of angle and time. We define the equilibration angle and time as the points at which steady state is reached and thus they mark the transition phase extent. Angle is measured as shown in figure 3.1 and

3.6. The effect of the dimensions of the annular charge

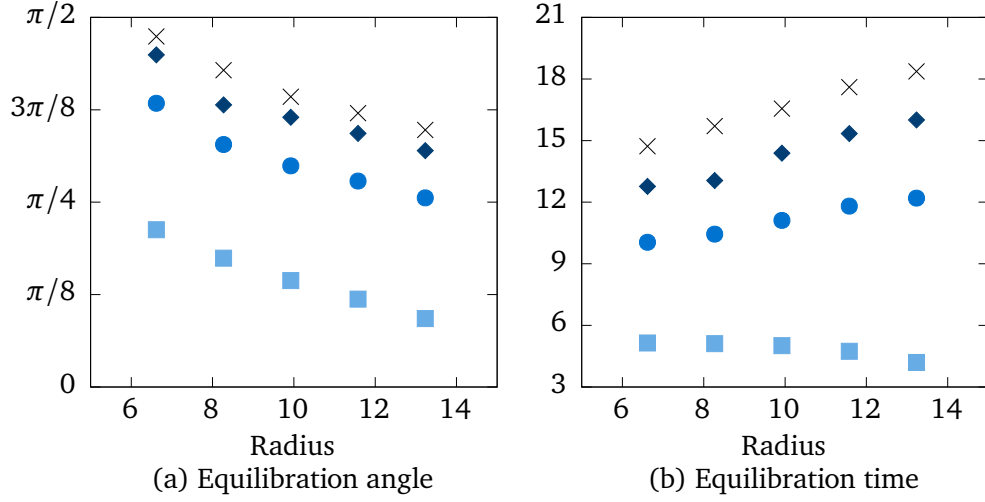


Figure 3.15: Equilibration angle and time for annular arcs of different inner radius and width. Time is zero when the detonation enters the annular arc. Configurations of different width are represented as seen in the legend of figure 3.14.

time is set to zero when the detonation wave enters the annular region. The criterion used to determine when steady state is reached is

$$W \geq 0.99W_s,$$

where W is the speed at the outer edge. The value of steady outer speed W_s , is defined in equation (3.8) and requires knowledge of the inner steady state speed V_s . This value is obtained from the numerical solution by averaging the speed values measured at the inner edge well after it has reached steady state.

Figure 3.15 presents equilibration angles and times for the studied configurations. The results indicate that both the equilibration angle and time increase with the width of the explosive annulus. Charges of larger width require more time for the effects of the inner edge to reach the outer parts which results in a more extensive transition phase in terms of both angle and time. In addition, the first regime is also more extensive and the distinctive $\sec \theta$ evolution is more prominent. In contrast, configurations of small width have a less extensive first regime and transition phase in general. In fact, for the configurations of the smallest width considered (figure 3.13a), steady state is reached early enough that the local effects of the outer edge do not develop significantly and the transition to steady state can be described solely by a bounded growth function.

The influence of the inner radius on the transition phase is more complex. Equilibra-

tion angle decreases with radius for all configurations but in the case of equilibration time we see opposing behaviour between configurations of different width. The exponential time dependent model predicts that the transition phase duration increases with steady outer speed. If this was a valid description of the transition phase and using expression (3.14), the transition phase duration should decrease with inner radius. Instead the equilibration time increases with radius, with the exception of small widths.

The increase of the transition duration despite the reduction of steady speed indicates that the acceleration of the wave front decreases with inner radius. As seen in section 3.5, the outer speed during the first regime of the transition phase depends on angular position which translates to a dependence on the dimensions of the annulus since,

$$\frac{dW(\theta)}{dt} = \frac{dW(\theta)}{d\theta} \frac{d\theta}{dt} = \frac{dW(\theta)}{d\theta} \frac{W}{R+D}. \quad (3.16)$$

The acceleration is inversely proportional to the inner radius of the annulus and hence, large radii have slower acceleration which results in reaching steady state at later times but not at larger angles. This can also be seen in figure 3.16, which shows detonation speeds over time during the propagation of detonation in the annular section.

The discrepancy between equilibration angles and times is a result of the local effects at the outer boundary. Thus, it is observed in configurations of sufficiently large width, where the effects of the outer edge are pronounced. If outer speed followed the suggested time-dependent exponential function during the transition phase, the transition phase duration would decrease with inner radius. This is indeed seen in small width configurations in which the local effects at the outer boundary are not developed and for which both equilibrium angle and time decrease with radius.

3.7 Conclusions

This study presented in this chapter is concerned with detonation propagation in condensed phase explosive charges consisting of a straight and an annular section. When a steady detonation in a straight charge enters the annular section, it goes through a transition phase and eventually reaches a new steady state of constant angular velocity. The characteristic features of both phases of detonation propagation in annular charges are identified and examined, as well as their dependence on the dimensions of the annular arc.

A diffuse-interface formulation [20] is employed for the calculations herein, which allows the modelling of a two-phase explosive with distinct equations of state for the

3.7. Conclusions

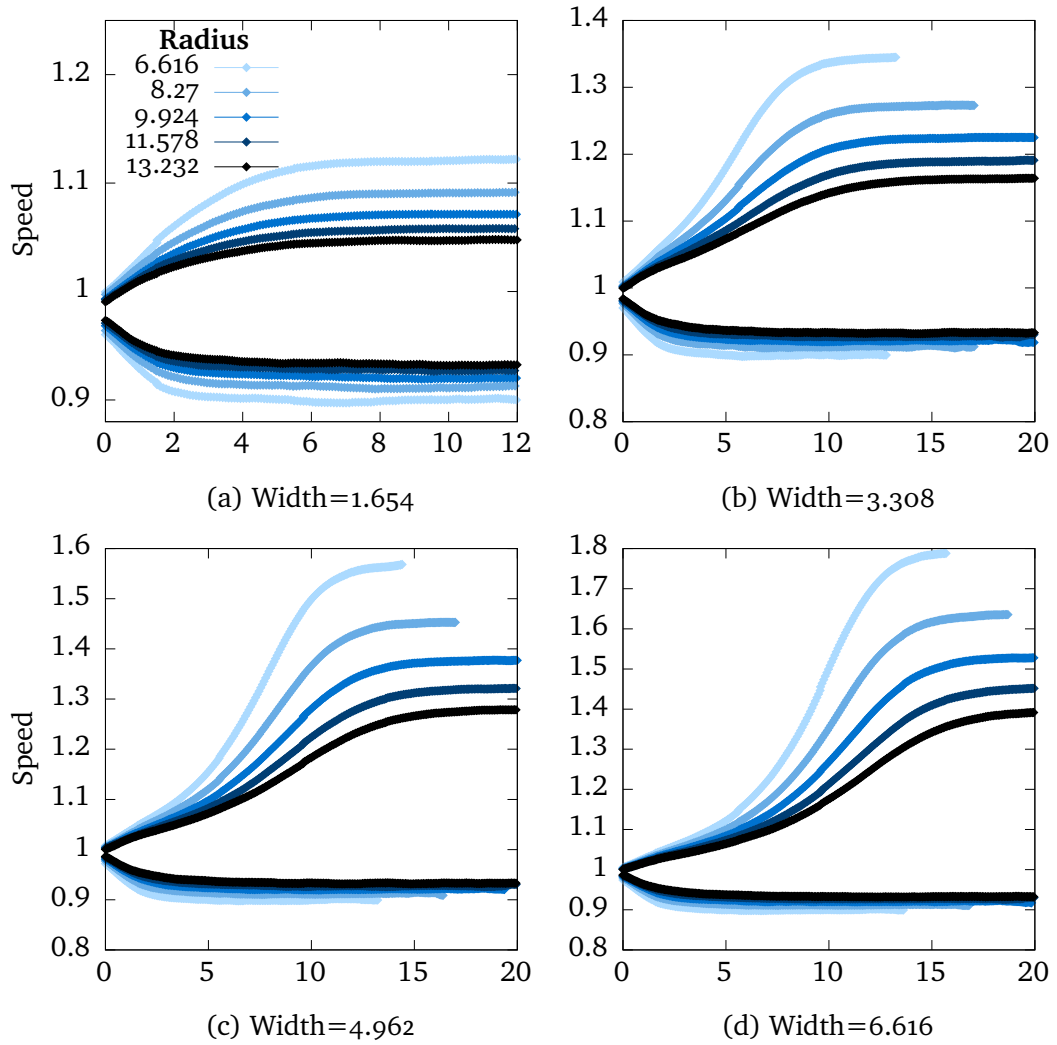


Figure 3.16: Detonation speeds over time along the inner and outer edge of the 90° annular arc. The plots correspond to configurations of different width, in which the radius varies from small (lighter colour) to large (darker colour). Time is zero when the detonation wave enters the annular region.

3.7. Conclusions

reactant and products and of an additional inert material. The explosive considered is LX-17 which is a granular, porous, polymer bonded explosive. It is modelled by two JWL equations of state and the Ignition and Growth reaction rate law. This provides a macroscopic description of the effects of the micro-structure of a heterogeneous high explosive and enables the homogeneous treatment of the explosive.

The computations in this study were performed within a parallel adaptive mesh refinement framework which allows the use of high resolution with small computational cost. Convergence studies were performed for all configurations studied to ensure that the solution is independent of the grid resolution.

The mathematical model and numerical methods were validated through several tests. These included the study of steady detonation in one-dimensional and cylindrical charges. The structure of the steady detonation obtained from the numerical solution was consistent with theory and was compared against analytic solutions in the one-dimensional case. In addition, a study of detonation speed over radius in cylindrical charges was performed. This showed good agreement with experimental values and demonstrated the capability of the model to capture the diameter effect curve of the explosive.

The study of annular charges follows the configurations used in the Lyle and Hayes experiments [6]. The steady state detonation speeds show good agreement with the experimental values but the transition phase deviates from the suggested exponential model. The numerical solution of the transition phase indicates that the outer speed increases linearly at the beginning, then at an increasing rate and in the final stage the acceleration decreases to zero and the detonation reaches steady state. These results are within the scatter of the experimental points but the strong oscillations present in the experimental measurements renders them unable to be used for the validation of the suggested description of the transition phase. Even though these experiments were conducted over thirty years ago, there have been no later experiments on detonation in annular charges that can provide more accurate measurements of the evolution of the detonation wave velocity. High quality data from experimental studies that utilize embedded gauges are required to provide a better depiction of the transition phase and to assess the numerical results of this study.

The effects that govern the evolution of detonation speed during the transition phase are investigated through configurations with only one of the boundaries that make up the annular arc. These indicate that steady state is induced by effects originating from the inner edge and travel along the front at a finite speed. Thus, the transition phase of the outer speed can be divided into two regimes. In the first regime, the effects of

3.7. Conclusions

the inner edge have not yet reached the outer part of the detonation and the outer speed is governed by local effects at the outer edge. These lead to a dependence of the detonation speed on the angular position along the arc. The second regime begins when the effects from the inner edge reach the outer part of the detonation. These change the curvature of the detonation front and lead the detonation speed towards the steady state value in a bounded growth manner.

The dependence of detonation propagation on the dimensions of the annular charge was investigated through a parametric study. We varied the inner radius and width of the charge and obtained the corresponding detonation speeds along the annulus. Results show that steady angular velocity depends only on the inner radius. In particular we observed an affine dependence of steady state angular velocity on the inner radius which has also been reported by Lubyatinsky et al. [7]. The width of the annulus does not influence the steady angular velocity but it affects the outer steady speed which increases with width due to the condition of constant angular velocity.

The dimensions of the annulus influence the transition phase as well. The width of the charge determines the extent of the first regime of the transition phase with larger widths leading to more pronounced local effects at the outer boundary. The inner radius influences only the second regime of the transition phase. Increasing radius brings the shape of the charge closer to a straight charge and results in less difference between inner and outer steady detonation speeds, as well as reduced angles at which steady state is reached.

The extent of the transition phase was studied in terms of the angle and time at which steady state is reached. Both equilibration time and angle increase with width for configurations of the same inner radius. For annuli of the same width, increasing inner radius leads to a decrease in equilibration angle. However, the equilibration time shows different behaviour depending on the width of the configuration. It increases with radius for large widths and decreases for the configuration of the smallest width.

This discrepancy is attributed to the first regime of the transition phase. The dependence of detonation outer speed on angular position during this regime leads to an inversely proportional relation between the acceleration of the outer part of the detonation and the inner radius of the annulus. This results in longer transition duration as the inner radius is increased in contrast to the decrease in equilibration angle. In the configurations of the smallest width, the equilibration time decreases with inner radius because the first regime is small and does not develop sufficiently to influence the transition duration.

Chapter 4

Initiation capability of detonators

4.1 Introduction

Detonators (or blasting caps, in mining terminology) are devices used to ignite insensitive explosive charges. They contain small quantities of sensitive high explosives and are designed to generate a shock that induces a detonation wave in a secondary explosive. One of the first versions of a detonator was invented in 1864 by Alfred Nobel when he observed that a small quantity of powerful explosive in a metal cup provided a more reliable and effective method for detonating nitroglycerine than simply using a flame [8].

Since then, safety concerns have led to the use of increasingly more insensitive explosives. To ensure their reliable ignition without requiring large quantities of sensitive explosives, a procedure called *explosive initiation train* is employed. This makes use of multiple explosives of increasing sensitivity in decreasing quantities. The sensitive explosives are used in small amounts, just enough to ignite a larger charge of a less sensitive explosive, and thus minimize the impact of an accidental ignition. Modern initiating trains can be either two-step, involving a detonator and the bulk explosive or three-step which also includes a booster between the detonator and bulk explosive. Three-step trains are commonly used in mining to initiate blastholes filled with ANFO which has very low sensitivity and cannot be ignited with a detonator alone.

A modern standard detonator has a cylindrical metal shell which is usually made out of aluminium, copper, steel or some alloy. The shell contains two different explosives, a sensitive primary charge called primer and a less sensitive explosive called base charge. In commercial detonators the most common explosives used are Lead Azide for the primary charge and PETN for the base charge.

4.1. Introduction

The reliable and efficient initiation of explosives is a matter of critical importance for the safety of explosion sites. A failure in the initiation of a blasthole filled with explosives will pose a severe post-blast hazard while an inefficient initiation will lead to a partial detonation with unpredictable outcomes. In addition, the failure of initiation can cause significant financial cost and delays especially in operations that involve time critical processes such as those designed to take advantage of the effect of multiple detonations.

There is continuous research and development of new detonators driven by the strict safety requirements, increasing environmental concerns, cost and better suitability to specific applications. This development is seen mostly in the synthesis of novel explosives with tailored properties, but aspects such as shell material and shape play an equally important role in detonator performance.

The impact of each part of the construction of a detonator on its initiating capability is not fully understood. Industry usually classifies detonators based on the type and quantity of base charge included. However, aspects such as the primary explosive, explosive density, the use of a confining cup, the material and design of the outer shell also influence the initiating power of a detonator [42, 43].

A range of tests have been devised to assess the initiating power of detonators but there has not been a clear consensus as to which is the most appropriate test and contradictory results have been reported [9, 10]. Bajpayee and Hay [10] suggest that the explosive energy output cannot be reduced to a single parameter and the differences between tests might be caused by orientation effects since certain tests concern only the axial direction whereas others consider the total energy output. They showed that detonators have different initiation capability when inserted in different orientations and that these differences vary between detonators as well.

Many studies that investigate the initiation power of detonators use the underwater test specified by the European standard EN 13 763-15:2004 [11]. The test determines the total energy output of a detonator in terms of the equivalent shock energy and equivalent bubble energy and provides expressions for their calculation from measurements of pressure over time at a specified distance from the detonator. The concept and assumptions behind this test will be discussed in a following section but its undisputed value is that it is widely used to compare the performance of detonators and experimental data is available for this configuration.

The study by Klapötke et al. [12] provides detailed data from the underwater test for a series of novel and common explosives used in detonators. They used aluminium shells and followed the methodology of the European standard which prescribes the

same pressing pressure for all detonators. The resulting density of the PETN charge was 1.5 g m^{-3} for detonators with base charge mass of 0.5 g and 0.7 g.

Orica, a leading manufacturer of mining products including detonators, underwent an effort to determine the energy output of its detonators according to the underwater test of the European standard [44]. They used the detonators of varying mass of PETN base charge and different shell material as well as the reference detonator 4 [11]. Their results show that the total energy output increases monotonically with the mass of the explosive charge and that detonators of the same mass and different shell materials have similar shock energy but differ in bubble energy. The shock energy of all considered detonators was equivalent to the reference detonator but the bubble energy of the copper/zinc detonator was found to be 5% lower than the reference detonator value while the aluminium detonator had 14% higher bubble energy. It also reports that previous experimental studies which measured detonator initiation power using different tests agree that the initiation capability of copper detonators is less than that of the corresponding aluminium detonators. However, the reasons behind this discrepancy are not known and the significance of the bubble energy with respect to the initiating capability is not understood.

The initiation capability of the detonator can also influence the strength of detonation in the receiving charge, especially in the case of highly non-ideal explosives such as ANFO. In a study by Bjarnholt and Holmberg [45], large ANFO charges showed differences in total energy output between the cases of initiation by detonators of different explosive mass. Bohanek et al. [46] studied the velocity of detonation (VOD) of ANFO initiated by detonators and boosters of increasing explosive mass. The detonators used followed the specifications of the reference detonators 1-5 described in the European standard [11] and were tested for their energy output according to the procedures of the standard. When the initiation was performed by the detonators, the VOD showed very low values and varied up to 150% between the smallest and largest detonator which implies that these were failed or partial detonations. In the case of boosters, the VOD also increased with increasing mass of explosive in the booster but only showed 13% variation between smallest and largest explosive mass. This is in agreement with the suggestion of explosive manufacturers that ANFO should be initiated with a booster and not just with a detonator.

The use of numerical methods in the analysis of detonator initiation capability provides the means to study complex configurations in a safe and cost effective way. The subject of initiation power has many aspects which are often not captured by the experimental setups. This study follows the underwater test procedure described in the

4.1. Introduction

European standard to investigate detonators of different shell materials and thickness.

4.1.1 Types of detonators

Simulating the response of a detonator requires knowledge of the structure and composition of such devices. Over the years, detonators have become more elaborate devices and the industry is now producing a range of detonators to suit different applications. This section gives a brief description of the characteristics of contemporary detonators including the technical specifications of detonators produced by the leading manufacturers in the mining industry.

The initiation of a detonator begins with a small impulse which ignites the primary explosive. The detonation of the primary charge ignites the base charge. Subsequently the detonation in the base charge generates a shock wave in the metal shell which is transmitted into the explosive outside and ignites it.

The design of a detonator can be broadly divided into four aspects. These are the mechanism of initiation, amount and type of priming charge, amount and type of base charge, and the material and shape of the metal shell. There are also secondary design features, such as the type of shielding to prevent accidental damage and electronic interference, the packaging and securing of the components and other choices that relate to the manufacturing process.

The mechanism of initiation is an aspect that has seen great development and several methods have been developed. One of the earliest types is the fuse which uses a slow burning material to initiate the primary charge. The most popular type of commercial detonators is the electric detonator where initiation is provided by a wire heated by an electric current. With the addition of delay compositions, these devices were able to have delays in the orders of milliseconds to seconds. For shorter delay periods, an exploding bridge wire was developed where higher intensity current is supplied and at a higher rate. This causes the vaporization of the wire which sends a shock wave into the primary explosive. The initiation delay is in the order of nanoseconds and is very precise. They are used in the initiation of nuclear weapons where the simultaneous initiation of explosives is required. Other types include shock tube for situations where electric circuits cannot be used and more modern types are the slapper and laser detonators.

The primary charge is an explosive that must be sensitive to small external stimulus while having low enough sensitivity to be safe for handling and transportation. It is required to be able to ignite by a simple initiating impulse (SII) which is a non-explosive

	i-kon II (Orica)	exel (Orica)	Electric Super SP [43] (Dyno Nobel)	Reference detonator 4 [11] (EU)	No. 8 [47] (USA)
Type	Electric	Non-Electric	Electric	Any	Any
Shell	Copper or alloy	Aluminium	Copper or Aluminium	Copper or Copper-Zinc	Aluminium
Length [mm]	89	89	63.5-96.5	65.5	31.8
Diameter (outer) [mm]	7.6	7.6	7.5	7	7.06
Thickness [mm]	0.5-1	0.5-1	0.42	0.42	0.19
Base charge	780 mg PETN	780 mg PETN	555 mg PETN	800 mg PETN	447 mg PETN
Primer charge	120 mg Lead Azide	120 mg Lead Azide	330 mg Unspecified	300 mg Unspecified	195 mg Lead Azide
Pressing pressure [MPa]				44	28
Output strength	Ref. 3	Ref. 4	No. 8	-	-

Table 4.1: Specifications of detonators used in the mining industry as well as of reference detonators.

4.1. Introduction

type of impulse, such as heat, impact, friction, spark. The primary explosives can be further divided based on whether they can detonate almost immediately after ignition and those that require some distance/time to develop a stable detonation [48]. The first substance to be used as primer was Mercury Fulminate but has now been replaced by Lead Azide as the most popular primary explosive. Other examples of primary explosives are lead styphnate and silver azide. Efforts to reduce the amount of lead, and other heavy metals emitted into the atmosphere have led to the development of DDNP (diazo dinitro phenol), but a suitable replacement of lead azide practically does not exist today [48].

The base charge is usually a secondary explosive such as TNT or tetryl for military detonators and PETN for commercial detonators. During the manufacturing of detonators, PETN is pressed into the detonator shell up to a specified compacting pressure. The value of the compacting pressure is an important aspect, since it controls the density of the explosive. In turn, the density affects the sensitivity of the explosive and the characteristics of the detonation wave such as velocity and CJ pressure and density. Subsequently, these affect the energy of the shock wave generated by the detonator and will influence its initiation capability. Thus, the estimation of the energy output of the detonator requires accurate specification of the density of the PETN charge. Unfortunately the manufacturing process of pressing the PETN in place means that the only available data is the compacting pressure and rarely is the density specified.

The last of the four main aspects of detonator design is the metal shell. This usually has a simple cylindrical shape with a small thickness of less than 1 mm. In some designs, the shell is tapered and has a slightly thicker upper part which gets progressively thinner towards the bottom. Another variation is having a dent at the bottom of the detonator shell. This creates a shaped charge effect where the metal forms a small jet of high velocity that enhances the initiation power of the detonator in the axial direction [10].

4.1.2 Tests of detonator initiation capability

There is an increasing need for standardized, reliable test procedures to assess and compare the efficiency of detonators, especially as more improvements in detonator design are being developed. This subject has been explored by the explosives community for more than a 100 years but it has yet to conclude on an effective and practical test that reliably correlates with the initiation capability of the detonator. The challenging aspect is that initiation efficiency cannot be represented by a single measurable parameter [10]. It depends on multiple factors of the detonator design as well as on the particular

application that is intended for. Thus, the most reliable test would be to study the detonator within the charge that is intended to initiate. However, such tests can be expensive and cumbersome which has led to the creation of multiple alternative tests.

Hall and Howell [8] classified detonator tests into direct and indirect methods. Direct methods measure the mechanical effect of the detonator directly, without inserting it into the insensitive explosive that is meant to initiate. Such tests, usually place the detonator in sand, water or next to a metal plate and measure its effect on the surrounding material. These tests are simpler and cost-effective to perform but may lead to grave inaccuracies if not verified by indirect methods [8]. Indirect methods place the detonator inside a charge of insensitive explosive and the configuration is tested as a whole.

A selection of direct tests used over the years are listed below.

Weight of explosive The most elementary direct test is to consider the weight of the charge. This was more useful when there was no variation of explosive compositions but nowadays, explosives have largely different characteristics and it is no longer relevant.

Lead-plate This test was used for quality control in factories that manufacture the detonators. The detonator is placed vertically on the centre of the plate. The performance of the detonator is assessed by measuring the size of the hole or the number and nature of radiating marks produced. There has been no evidence that the results of this test represent the initiation capability of the detonator [9].

Lead-block tests Similar to the lead plate test, but the detonator is placed in a tight cavity within a lead block. The test measures the increase of the volume of the cavity to assess the initiation capability. As with the lead plate test, it has not been shown that it correlates with initiation efficiency.

Sand test This test inserts a detonator in a barrel of specified mass of sand. After ignition the sand is screened and the amount of sand that was crushed is taken as a measure of the ability of the detonator to initiate an explosive. This test was compared to an indirect method by Grant and Tiffany [9] and showed contradictory results. The authors suggest that the sand test is generally misleading as a measurement of initiating efficiency.

Indirect tests place the detonator within a receptor explosive charge and examine its ability to initiate it. The original method can be traced back to Esop's method [49]

4.1. Introduction

which placed the explosive in an explosive mixture of adjusted sensitivity, specifically a mixture of cottonseed oil and picric acid, and determined the amount of oil that can be added without preventing detonation of the mixture. Several modified versions have been developed since then using different receptor explosive but also different criteria for determining the extent of detonation in it.

TNT-talc and a lead plate This test uses a mixture of TNT and talc (hydrated magnesium silicate) and examines the diameter of the cavity made into a 3 cm lead plate after firing the detonator within the explosive mixture. The talc in the mixture is increased until the cavity diameter in the lead plate is as small as the diameter of the charge itself, where it is assumed that the detonation was incomplete.

Miniature cartridge test This test places the detonator within a 5 g of TNT and iron oxide mixture contained in a paper cartridge of 12.5 mm in radius and 68.8 mm in length. The cartridge is then placed in a steel barrel filled with 1 kg of sand of specific distribution of particle size. The extent of the detonation is determined by measuring the crushed sand after the detonator was fired. This is determined using sieves to separate the sand particles that have been reduced to a lower than a specified value. An innovation of this method is the measurement of the crushed sand in the case of firing the detonator within an inert material of purely iron oxide and its subtraction from the results of the mixtures containing explosive. Thus, the results represent the effect of the detonator on the receptor charge and not of the detonator itself. Results from this test contradicted previous sand test results [9] and lead-plate results [42] which suggests that they are unreliable, since the miniature cartridge test is an indirect test which is considered more appropriate.

Liquid Nitromethane This test was proposed by Bajpayee and Hay [10] of the U.S. Bureau of Mines. It uses liquid explosive mixtures of Nitromethane and Ethylene Diamine where the sensitivity is adjusted using 2-Nitropropane. The use of a liquid mixture was chosen because it involves less uncontrolled variables relating to the homogeneity of the mixture. A solid granular explosive requires precise control of the particle size and bulk density while a liquid mixture is simpler to produce. The liquid is put in a steel tube of length 127 mm and diameter 35.1 mm and placed on a metal witness plate. The proportion of 2-Nitropropane was increased until the detonator could not detonate the desensitized mixture.

The criterion for detonation was whether a hole was punched in the witness plate. An innovation of this test is that it places the detonators in different orientations which are: fully immersed, end-on and side-on. Initial tests by the authors showed that the initiating capability of detonators was different for each orientation. This is suggested to explain the inconsistency between direct tests since some of them account for total energy while others measure the energy in the axial direction only.

The theme that direct tests have no proven correlation with initiation efficiency and that indirect tests should be preferred has been reported multiple times in the last century [8, 49, 9, 10]. Yet, the most popular test of recent years is the direct underwater test which has also been adopted as a European standard [11].

4.1.3 European standard test

A widely used test for rating detonators is described in the European standard EN 13 763-15:2004 [11]. This is a direct test which ignites the detonator inside a water tank and measures the blast wave produced in the water to determine the equivalent initiating capability of the detonators. A pressure gauge is placed at a specified distance from the detonator to measure values of pressure over time. Certain quantities are calculated from this signal and are compared to the results from a reference detonator of given characteristics.

Underwater explosions produce an initial blast wave in the water and an expanding gas bubble of detonation products. A blast wave consists of a sharp increase in pressure and other state parameters of the fluid followed by a decrease that is roughly exponential. The gas bubble initially expands rapidly into the surrounding water while pressure and temperature within reduces. The inertia of the moving water leads to the expansion of the gas bubble to pressures lower than the hydrostatic pressure which causes the reversal of water velocity and the contraction of the bubble. Similarly the contraction does not lead straight to pressure equilibrium but re-compresses the detonation products which results in another cycle of expansion and contraction and the emission of a secondary pressure pulse of smaller amplitude than the initial. The process is repeated while the gas bubble rises through the water until the energy losses cause the system to reach pressure equilibrium or the gas bubble reaches the water surface. The blast wave propagation and gas bubble oscillation occur at different timescales. In the case of reference detonators, the shock wave reaches the measuring point in μs whereas the gas bubble oscillation has period of the scale of ms [12].

4.1. Introduction

The data of pressure over time are used to calculate the energy output of the detonator using expressions taken from the classical work of Cole on underwater explosions [50]. As the author states, the relation between experimental shock wave pressures and possible forms of energy is not clear. In this case, the energy is calculated as the sum of the shock wave and the energy of the gas bubble oscillations.

The energy from the shock wave is determined by considering the work done on a spherical surface ahead of the shock

$$E_{sw} = 4\pi \int_0^\tau r^2 P u dt, \quad (4.1)$$

where r is the position of the surface, P is pressure, u is particle velocity. Considering the acoustic approximation, the particle velocity is replaced by

$$u(t) = \frac{P - P_0}{\rho_w c_w} + \frac{1}{\rho_w r} \int_0^\tau P(r, t) - P_0 dt, \quad (4.2)$$

where ρ_w is the water density and c_w is the speed of sound in water. The second term is dropped as it relates to kinetic energy of the water which will be returned when the gas bubble is compressed which results in

$$E_{sw} = \frac{4\pi R^2}{\rho_w c_w} \int_0^\tau P^2(t) dt. \quad (4.3)$$

There is an arbitrary selection of the time τ used as the upper limit of the integral. Cole [50] suggests that it should be of the order of the time constant θ for which $P(\theta) = P_{peak}/e$ and the European standard specifies integration up to one time constant.

The energy of the gas bubble is determined by the interval, t_b , between the first pressure peak and the first collapse of the bubble signified by a second blast wave. In the case where there are no effects from the boundaries this energy has a simple relation with the bubble period and the hydrostatic pressure

$$t_b \sim E_b^{\frac{1}{3}} P_h^{\frac{5}{6}}. \quad (4.4)$$

The test configuration described in the European standard uses a tank of specified minimum dimensions with added lining to absorb reflections from the walls. The detonator is fixed in a vertical position and the sensor is at a distance of 400 mm from it and at the same height. The conditions such as pressure and temperature should not vary more than some prescribed thresholds. Since the measurements are made with

the same configuration and conditions, then the energy expressions can be simplified to the equivalent energy quantities. These are

$$E_{sw} = \int_0^{\theta} P^2(t)dt, \quad (4.5)$$

for equivalent shock energy and

$$E_b = t_b^3, \quad (4.6)$$

for equivalent bubble energy.

The standard requires firing twenty detonators of each type tested and ten of the reference detonator and calculate the mean value and standard deviation. These values are then compared with the values from the reference detonator to assess whether they are of equivalent initiating energy. To classify as equivalent with a reference detonator, the mean shock energy of the test detonators shall be not less than the mean shock energy of the reference detonators and all single values of the shock energy shall be greater than 90% of the mean value of the reference detonators.

Even though this test provides useful standardization for comparing detonators, there are several arguments against its suitability for assessing the initiating capability of detonators. The test considers the shock wave in a single direction, off the side of the detonator. The reasoning is that the distance at which the shock wave is measured is in the far field (more than 100 times larger the radius of a reference detonator) where the blast wave has become spherical. However, measuring at the far field is also a disadvantage of the test, as these devices are in close contact with the explosive that needs to be ignited and the magnitude and shape of the blast wave in the near field is the most important factor of it. At large distances, the blast wave becomes spherical independent of the nature of its source [51] and eventually degenerates to a near acoustic wave which conceals the distinguishing characteristics that it had in the near field.

The underwater explosion test has been widely used to measure the brisance and heaving power of explosive charges, represented by the two types of energy described. However, while the connection of the shock wave with the initiation process of an explosive is evident, there is no such connection for the bubble energy. This process has a much slower timescale than the initiation process and there is no empirical or theoretical arguments for its influence on the initiation of an explosive. Furthermore, this test and the corresponding energy expressions have been designed to give a measure of the total energy of the explosive. However, the initiation capability of an explosive is

4.2. Equations of state

not merely an issue of energy magnitude but also of how this energy is released.

4.2 Equations of state

The physical response each material is described the equation of state (EOS). In this work, the PETN reactants and products are modelled using two distinct Jones-Wilkins-Lee (JWL) equations of state presented in section 2.5. In the next section we describe a modification to accommodate the snow plough porosity model. Also described is the stiffened gas equation of state used to model the water.

The elastic-plastic materials use a hyperelastic equation of state which is a function of the principal invariants of the Finger deformation tensor and entropy and is described in the work of Barton and Drikakis [16] along with the parameters for the materials aluminium, copper and steel. For plastic flow we use the perfect plasticity model of constant yield stress [17].

4.2.1 The snow plough porosity model for the JWL EOS

The classic expression of the JWL equation of state [1] written in the Mie-Grüneisen form

$$e - e_{\text{ref}}(\rho) = \frac{p - p_{\text{ref}}(\rho)}{\rho\Gamma(\rho)}, \quad (4.7)$$

has a constant Grüneisen coefficient $\Gamma(\rho) = \Gamma_0$ and the following reference curves

$$p_{\text{ref}}(\rho) = A \exp\left(-R_1 \frac{\rho_0}{\rho}\right) + B \exp\left(-R_2 \frac{\rho_0}{\rho}\right) + C \left(\frac{\rho_0}{\rho}\right)^{-(\Gamma+1)}, \quad (4.8)$$

$$e_{\text{ref}}(\rho) = \frac{A}{\rho_0 R_1} \exp\left(-R_1 \frac{\rho_0}{\rho}\right) + \frac{B}{\rho_0 R_2} \exp\left(-R_2 \frac{\rho_0}{\rho}\right) + \frac{C}{\rho_0 \Gamma} \left(\frac{\rho_0}{\rho}\right)^{-\Gamma}, \quad (4.9)$$

where A , B , C , R_1 and R_2 are parameters calibrated for the particular explosive.

The expressions of the reference curves are usually written without the third term because they cancel each other when replaced in equation 4.7. Without the third term, the $p_{\text{ref}}(\rho)$ and $e_{\text{ref}}(\rho)$ curves do not correspond to the isentropic values but this does not affect calculations which require only an incomplete EOS $p(e, \rho)$. However, the Hybrid formulation makes use of temperature of the materials and requires the definition of a thermal equation of state $T(p, \rho)$.

An extension to a complete EOS is achieved with the expression

$$T - T_{\text{ref}}(\rho) = \frac{p - p_{\text{ref}}(\rho)}{c_v \rho \Gamma(\rho)}, \quad (4.10)$$

which requires the use of a temperature reference curve [52]. It is evident that if expression $p_{\text{ref}}(\rho)$ does not correspond to the actual isentropic value and $T_{\text{ref}}(\rho)$ does, then the temperature value will be invalid. For example, for an isentropic process the temperature should follow the $T_{\text{ref}}(\rho)$ expression, but if $p_{\text{ref}}(\rho)$ does not represent the isentropic value then $(p - p_{\text{ref}}(\rho))$ will have a value other than zero and the retrieved temperature will differ from the value of $T_{\text{ref}}(\rho)$.

The reference curve for temperature can be determined by considering that it is an isentropic curve and must satisfy the thermodynamic identity

$$\frac{\Gamma(V)}{V} = -\frac{1}{T} \left(\frac{\partial T}{\partial V} \right)_S. \quad (4.11)$$

In the case of JWL EOS, Γ is a constant and the integration yields

$$T_{\text{ref}}(\rho) = T_0 \left(\frac{\rho_0}{\rho} \right)^{-\Gamma}, \quad (4.12)$$

where T_0 is the initial temperature.

It is interesting to note that expression 4.12 has the same form as the third term of the energy reference curve of expression 4.9. This means that the two terms may cancel each other when replaced in a thermal EOS of the form $T(e, \rho)$ if the parameters for an explosive are such. This would allow the use of reference curves that omit the temperature curve and the third term of the pressure and energy reference curve without leading to the calculation of unrealistic temperature values. However, the proximity of the calculated values to the appropriate temperature values depends on the particular parameters and a general set of parameters for an explosive may not produce physical temperatures without the use of appropriate reference curves.

The manufacturing process of detonators involves pressing the explosive in the shell up to a specified pressure which results in a porous material. The porosity of the explosive influences the velocity of detonation and CJ state as well as the von Neumann spike which justifies the use of a porosity model. A porous material of density ρ_0 is characterized by a skeletal density ρ_{00} of the material without the pores. In the case of an explosive, the skeletal density corresponds to the theoretical maximum density

4.2. Equations of state

(TMD) that the explosive can be pressed into a charge. During the compression of porous material the closing of the voids happens first and requires little work compared to compression above the skeletal density.

The porosity model chosen in this study is the snow plough model [53] which considers the work required to compress a porous material up to its skeletal density to be negligibly small. Evidently, this assumption is more accurate for strong shocks that compress the material to high densities but is less appropriate for weak shocks where difference between the work for compressing up to the skeletal density and beyond that is not high. A detonation wave compresses the material to densities much higher than the skeletal density which justifies the use of the snow plough model. In addition, it is simple to implement and does not introduce additional parameters that would require calibration.

The compression work is defined by the integral of pressure over volume. To minimize the work for compressing up to the skeletal density, the pressure reference curve is set to zero for densities lower than the TMD. To maintain continuity of the reference equations, pressure should be zero at the TMD value as well. However, the condition $p_{\text{ref}}(\rho_{00}) = 0$ is not generally satisfied by the form of the JWL reference curves and it is up to the parameters to satisfy this condition. In this work, the value of C is adjusted so that it satisfies the above condition.

The complete expressions for the reference curves with the snow plough porosity model are

$$p_{\text{ref}}^{\text{sp}}(\rho) = \begin{cases} 0 & \rho \leq \rho_{00} \\ p_{\text{ref}}(\rho) & \rho > \rho_{00} \end{cases}, \quad (4.13)$$

$$e_{\text{ref}}^{\text{sp}}(\rho) = \begin{cases} e_0 = e_{\text{ref}}(\rho_{00}) & \rho \leq \rho_{00} \\ e_{\text{ref}}(\rho) & \rho > \rho_{00} \end{cases}, \quad (4.14)$$

$$T_{\text{ref}}^{\text{sp}}(\rho) = \begin{cases} T_0 & \rho \leq \rho_{00} \\ T_{\text{ref}}(\rho) & \rho > \rho_{00} \end{cases}. \quad (4.15)$$

and the parameters for PETN are given in table 4.2.

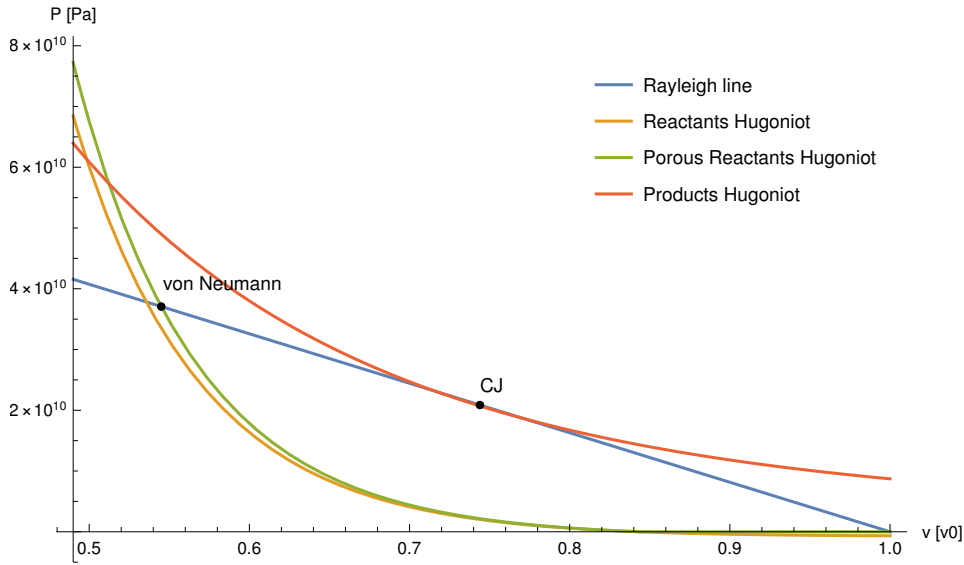


Figure 4.1: Comparison of the regular and porous reactants Hugoniot plotted in the $p - v$ phase space for the PETN parameters used in this study. The von Neumann pressure is reduced for the porous explosive. Also plotted is the products Hugoniot and the Rayleigh line.

4.2.2 Stiffened gas EOS

The water is modelled by the stiffened gas EOS which is given by

$$p(\rho, e) = (\gamma - 1)\rho e - \gamma p_\infty \quad (4.16)$$

where γ and p_∞ are empirically determined constants. The stiffened gas EOS has been extensively used to model water especially in underwater explosion applications and a large range of parameters exist in literature. The parameters used in this study are taken from Shyue [54] and are shown in table 4.3. These parameters were chosen because they yield a sound speed value of 1450 m s^{-1} which corresponds to water at 10°C [55] as were the conditions in the experiment by Klapötke et al. [12].

The stiffened gas EOS emulates an ideal gas that is already at pressure p_∞ . In the case of water, this value is of the order of 1000 atm and thus requires a similarly large change in pressure to produce a significant change in density which explains the common assumption of incompressibility of water.

4.2. Equations of state

The expression of speed of sound is

$$c^2 = \frac{\gamma(p + p_\infty)}{\rho} \quad (4.17)$$

and is well defined for negative pressures or tension. While this is physical in general, the accuracy of the EOS in the range of negative pressures is debatable. Negative pressures would most likely lead to cavitation.

4.2.3 Parameter set for the explosive

The explosive used most widely in industrial-grade detonators is PETN. However, the manufacturing and packing process varies significantly within the industry which results in explosives of different characteristics. During manufacturing, the PETN is machined or hand pressed in the detonator shell. The result is a porous explosive with a density around 1.5 g cm^{-3} . Given that the density of PETN crystals is 1.778 g cm^{-3} [56], the void fraction is approximately 15%.

The porosity of the explosive has a great impact on the characteristics of the explosive. Critically, it sensitizes the explosive since the voids and grains that make up a porous explosive are locations where hotspots are formed. These hotspots eventually coalesce and lead to the formation of a detonation wave in the explosive. The sensitizing effect is valid for small levels of porosity. At larger values it actually has the opposite effect and causes the desensitization of the explosive. The initial density of the explosive also influences the CJ and von Neumann states of the detonation wave. The pressure of both states reduces with increasing porosity as the reactants Hugoniot steepens and the energy density reduces. Thus it is critical to use explosive equations of state and parameters that produce the experimental detonation properties of the explosive in order to accurately simulate the underwater explosion of the detonator. For the explosive considered here, the difference between the regular and porous Hugoniot can be seen in figure 4.1 and results in a 11% difference in the pressure of the von Neumann spike.

The explosive characteristics of pure PETN crystals have been extensively studied and there exist well verified parameters for PETN at the theoretical maximum density (TMD) of $\rho_{\text{TMD}} = 1.778 \text{ g cm}^{-3}$ [56]. In the case of porous versions of PETN the data are not so extensive. The LLNL High Explosives Handbook [57] provides JWL parameters for a range of porous versions of PETN. However, Green and Lee [58] reported flaws in the calculations of the study that the LLNL EOS parameters are based on and redid the

4.3. Problem setup and convergence

experiments with significantly different results. They provide revised values for the velocity of detonation (VOD) and CJ density and pressure for a range of initial densities which are mostly lower than the original study. Thus appropriate calibration of the explosive parameters is required.

In the two phase model, the CJ state and the VOD are controlled by the products equation of state. The initial parameter set is taken from the LLNL High Explosives Handbook [57] but the coefficients A and B are adjusted to match the CJ state from the study of Green and Lee [58]. Since the study has no data for the exact initial density of $\rho_0 = 1.5 \text{ g cm}^{-3}$, the values are interpolated from the two closest densities and are given in table 4.2. The coefficient C is determined from the condition $p_{\text{ref}}(\rho_0) = 0$ for the porous reactants and $p_{\text{ref}}(\rho_{\text{CJ}}) = p_{\text{CJ}}$ for the products. The parameters for the reactants are taken from a study of Tarver et al. [56] and correspond to PETN of density $\rho_0 = 1.778 \text{ g cm}^{-3}$ which is close to TMD. The snow plough model is used to model the porous PETN of density $\rho_0 = 1.5 \text{ g cm}^{-3}$. Lastly, the parameter set for the reaction rate is taken from the study of Lee and Tarver [2] which matched initiation experiments for porous explosive at density $\rho_0 = 1.6 \text{ g cm}^{-3}$.

4.3 Problem setup and convergence

The problem setup follows the underwater detonator test described in the European standard. The basic components are a detonator and a pressure gauge placed in a water tank and separated by a distance of 400 mm. The setup is axisymmetric around the axis of the detonator and the equations are solved in cylindrical coordinates in a two-dimensional domain.

The detonator is made of a column of explosive of radius $R = 3.3 \text{ mm}$ and the length of the charge is determined from the mass and density of the explosive for each simulation. The charge is confined by a thin metal shell of thickness $T = 0.5 \text{ mm}$ which is representative of most industrial detonators. A metal cup of thickness $C = 6.2 \text{ mm}$ is placed above the explosive charge to emulate the actual cup and additional components placed on top of the charge in detonators. The length of the simulated detonator shell is shorter than in industrial detonators and covers only the explosive charge and cup. A longer detonator shell does not change the solution since the blast wave depends only on the section that includes the explosive. Real detonators have longer shells for practical reasons such as for housing the circuitry required for operation and for the insulating and safety materials.

The rest of the domain is filled with water. The domain size is 500 mm by 400 mm.

4.3. Problem setup and convergence

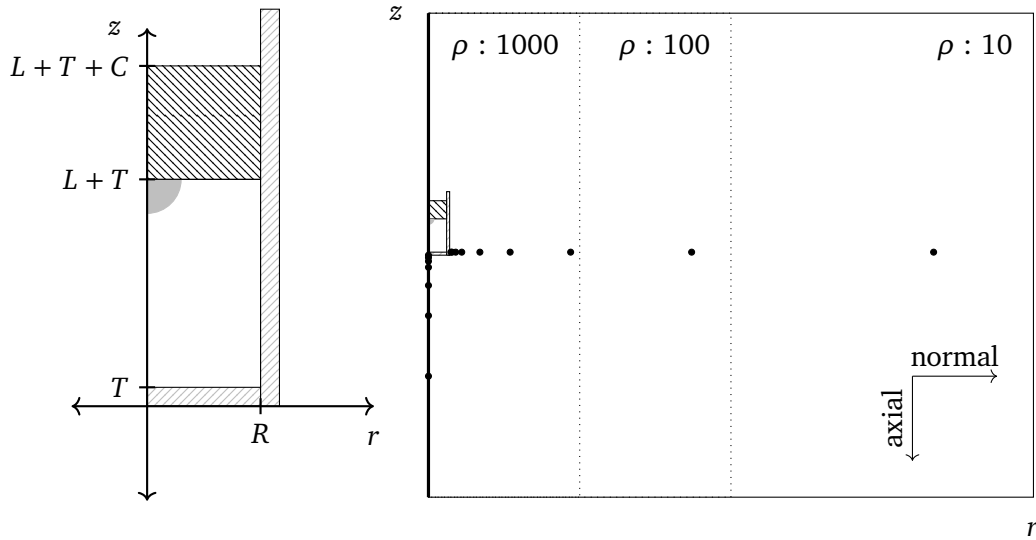
Parameters	PETN	
	Reactants	Products
Γ_0	0.5675	0.28
A [10^{11} Pa]	202.80	6.51712
B [10^{11} Pa]	-0.03752	0.19187
C [10^9 Pa]	0.4596	1.308
R_1	10	6
R_2	1	2.6
Q [10^6 m ² s ⁻²]	0	5.975
c_V [m ² s ⁻² K ⁻¹]	1528.4	625
T_0 [K]	293	3811
ρ_0 [kg m ⁻³]	1500	1500
ρ_{00} [kg m ⁻³]	1778	-
D [m s ⁻¹]	7370	
ρ_{CJ} [kg m ⁻³]	2016.2	
p_{CJ} [10^9 Pa]	20.86	
ρ_{vN} [kg m ⁻³]	2752.4	
p_{vN} [10^9 Pa]	37.07	

Table 4.2: JWL EOS parameters for PETN [56, 57, 58].

Parameters	Water
γ	7
p_∞ [10^9 Pa]	0.3

Table 4.3: Parameters of the stiffened gas EOS for water [54].

4.3. Problem setup and convergence



(a) A close-up of the detonator configuration.

(b) The full domain used in the study.

Figure 4.2: The detonator configuration involves an explosive charge of radius R and length L placed in a metal shell of thickness T and enclosed by a cap of thickness C . This is placed in water in a domain of dimensions 500 mm by 400 mm along with gauges at several points in the axial and normal direction. The refinement criterion is reduced in areas of the domain that are further from the detonator to ensure proper refinement of the expanding blast wave.

The boundary conditions are reflective along the axis of the detonator and transmissive at the rest. The transmissive condition is not perfect in multi-dimensional problems and partial reflections occur which can influence the flow inside the domain. Thus, we ensured that the domain boundaries are sufficiently far as to not influence the blast wave in areas of interest.

The charge in the detonator is initiated by a hemispherical high pressure region of radius $0.3R$ and pressure 20 GPa. This leads to a prompt formation of a detonation in the base charge of the detonator. The detonation propagates in the explosive and induces a shock in the confining metal which is subsequently transmitted in the water.

The domain is considerably extensive compared to the length-scale of the detonator. The distance of 400 mm at which the pressure is measured is more than 100 times the radius of the detonator and four orders of magnitude larger than the resolution required to adequately resolve the reaction zone of the explosive. Such simulations are made possible with the use of adaptive mesh refinement (AMR). The grid is refined

4.4. Validation

Material	Variable	Threshold
Explosive	λ	10^6
Metal	μ	10^6
Water	ρ	$10^3 - 10$

Table 4.4: The refinement criterion uses a different variable for each material. The area is refined if the normalized gradient of the variable $(\nabla v/v)^2$ exceeds the prescribed threshold.

according to refinement criteria shown in table 4.4 which increase the resolution around the detonation and shock waves in the metal and water in addition to continuous refinement at material interfaces. In the case of water, the refinement criterion is lowered for regions further from the detonator, as shown in figure 4.2b, to keep the blast wave refined as it expands.

The convergence of the numerical solution is assessed by examining the blast wave in water for a series of simulations of increasing resolution. The detonator has an aluminium shell and the comparison is on pressure over time at a distance of 400 mm which will also be used for validating the solution against experimental data. The initial resolution is set to $\Delta x = 200 \mu\text{m}$ and is halved for every subsequent simulation.

Figure 4.3 shows pressure over time in water for increasing resolution. The solution converges in an expected rate and the difference between resolution $\Delta x = 50 \mu\text{m}$ and $\Delta x = 25 \mu\text{m}$ is very small in the context of this study. Thus the selected resolution is $\Delta x = 50 \mu\text{m}$ which is adequate for comparing the experimental results and for assessing the differences in the blast wave strength between different detonators.

4.4 Validation

4.4.1 One dimensional steady detonation

The structure of the steady one-dimensional detonation wave is described by the ZND detonation model [38] and characteristic quantities, such as the states at the von Neumann and CJ points are calculated analytically and used to verify the implementation of the model.

The setup considered in this section is one-dimensional and contains solely the explosive. The initial conditions consist of a small region of high pressure, equivalent to a booster, placed at the left end of the domain and the rest of the explosive is at

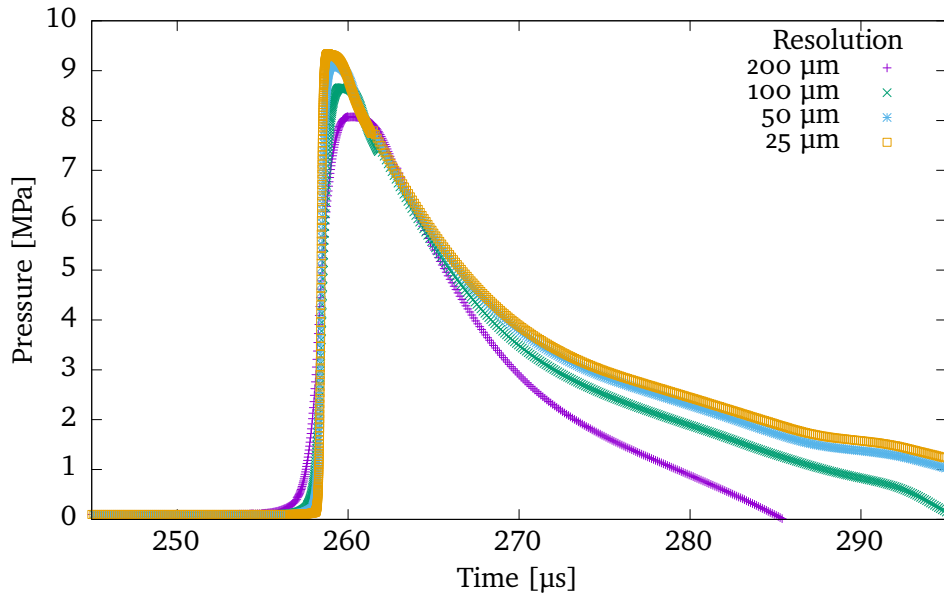


Figure 4.3: Convergence study for the numerical solution of the pressure pulse measured at 400 mm for the case of 0.5 mm thickness aluminium shell detonator.

ambient conditions. The pressure in the booster region is set to 20 GPa which is close to the CJ pressure of the explosive. This causes the rapid expansion of the explosive in this region, which compresses and ignites the explosive ahead, leading to the quick formation of a steady detonation wave.

The numerical solution of the one-dimensional detonation wave is shown in figure 4.4 for a resolution of $\Delta x = 25 \mu\text{m}$. The solution is presented in a series of pressure plots, for times after the detonation has settled to steady state and the density, pressure and mass fraction profile of a single instance of the wave. The solution demonstrates the almost ideal detonation of PETN with a very thin reaction zone of approximately $150 \mu\text{m}$ or 20 ns. The von Neumann and CJ points of the numerical solution match the values calculated analytically.

4.4.2 Underwater initiation capability test

The complete configuration of the detonator underwater is validated against the experimental work of Klapötke et al. [12]. The experiments follow the methodology of the underwater initiation capability test described in the European standard EN 13 763-15:2004 [11]. The detonators have an aluminium shell and are filled with different amounts of PETN charge. The European standard specifies the pressure that

4.4. Validation

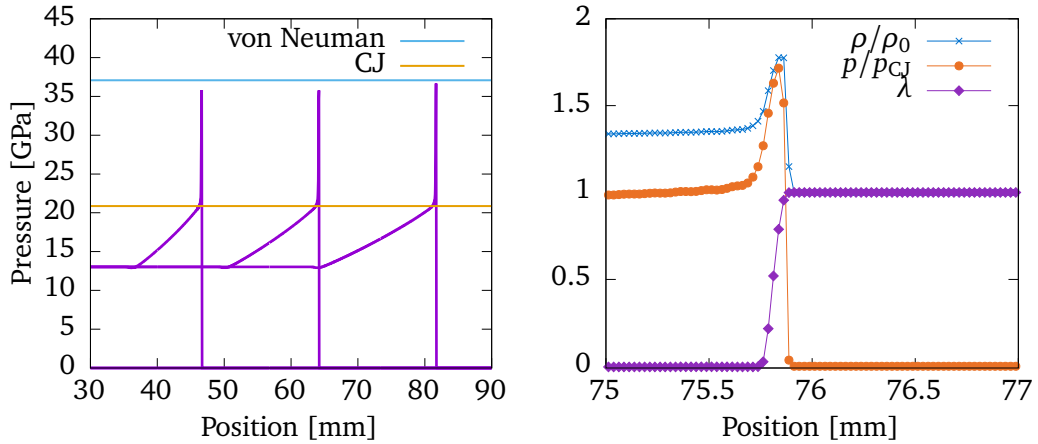


Figure 4.4: Plots of the numerical solution of the one-dimensional steady detonation wave in PETN. The left graph shows pressure of the propagating wave along with the von Neumann and CJ values determined analytically. The right graph shows an instance of the steady detonation wave in PETN showing scaled values of density and pressure and the mass fraction of the reactant.

the charge is pressed into the shell. This leads to different density depending on the mass of the explosive. The density for the detonators with explosive mass of 500 mg and 700 mg was measured at $\rho_0 = 1.5 \text{ g cm}^{-3}$ which is the density that corresponds to the explosive parameters presented in section 4.2.3.

Figure 4.5 shows the pressure trace measured experimentally against the results of the simulation. The numerical solution shows stronger blast waves than reported experimentally for both amounts of explosive. The differences can be seen quantitatively in table 4.5. The numerical peak pressure differs by approximately 10% and the equivalent energy by almost 30%. A higher energy output is expected from the numerical simulation because some of the energy released by the explosive is spent in fracturing the metal shell which is not modelled in this study. However, this cannot account for the whole difference since the amount of energy lost in fragmenting the shell is not more than 7% of the shock wave energy, even with the most favourable metrics [43].

Furthermore, the blast wave from the experiments appears significantly diffused. Experimental studies of blast waves in water estimate the shock front thickness between $10^{-8} \text{ m} - 10^{-7} \text{ m}$ and a rise time of less than 1 ns [59, 50] even for a weak wave travelling close to the speed of sound. The numerical solution shows a sharp discontinuity that is expected as a weak solution of the Euler equations which do not include viscous or heat

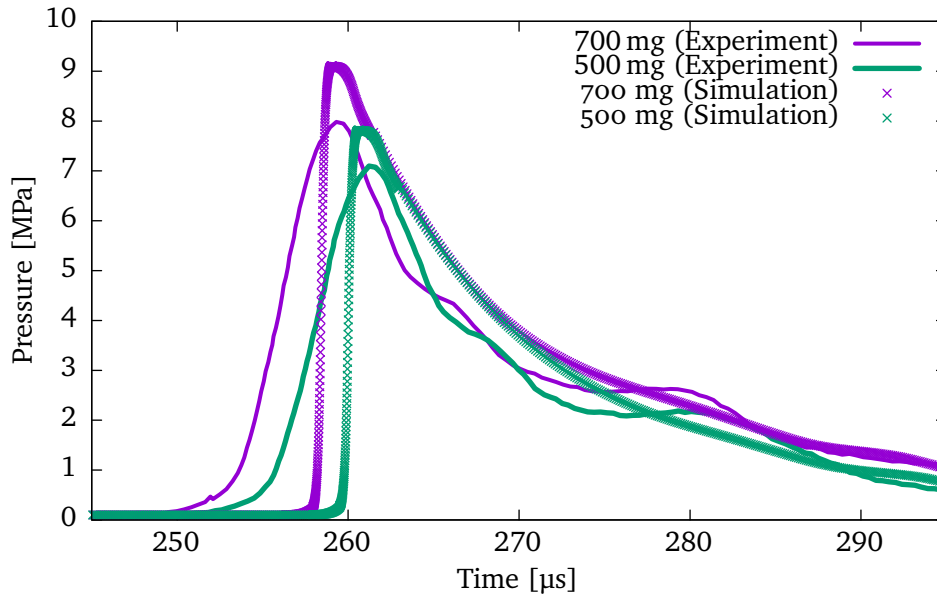


Figure 4.5: Comparison between experiment and numerical solution for the blast wave pressure measured at 400 mm for detonators containing different amounts of explosive.

	Mass	Experiment	Simulation	Difference
peak P [MPa]	700 mg	8.06 (0.04)	9.02	11.9%
	500 mg	7.12 (0.12)	7.73	8.6 %
equiv E_S [$10^6 \text{ Pa}^2 \text{ s}$]	700 mg	463 (5)	598	29.2%
	500 mg	339 (5)	430	26.8%

Table 4.5: Comparison of the numerical and experimental values for maximum pressure and equivalent shock wave energy.

4.4. Validation

conduction terms. The choice for omitting these terms is justified for this application as the Reynolds number is of the order of a million and the inclusion of diffusion terms would have negligible results.

However, the experimental data show a more extensive front with a rise time of around $5\ \mu\text{s}$ which is not explained physically. The cause of this appeared diffusion is the limitations of the pressure gauge. Even though the European standard specifies the use of gauges with response time of less than $2\ \mu\text{s}$ this usually corresponds to static load and the transient response characteristics are worse due to the finite size of the sensor.

The distortion of the blast wave because of their finite size is a fundamental problem of piezoelectric sensors [50]. This distortion manifests as increased rise times and lower peak pressures because the shock wave requires time to cover the entire piezoelectric crystal. This leads to increased rise time of the order of the time required for the shock wave to cover the entire sensor. In addition, since the electric signal generated is proportional to the total compression of the piezoelectric crystal this leads to reduced pressure measurements as well.

The pressure sensor used in the experimental study is the PCB Piezotronics Inc, model 138A5. It uses a cylindrical tourmaline crystal of 3.2 mm in diameter and 1 mm in length. It has a rise time of less than $1.5\ \mu\text{s}$ and a bandwidth of $2.5\ \text{Hz} - 10^6\ \text{Hz}$. A study by Zhou et al. [60] analysed the performance of two commercial piezoelectric pressure sensors (one of which was the sensor used in the experiment) in capturing blast waves in water generated by electric wire explosions. Results showed that the PCB sensor severely distorted the wave forms resulting in a more extensive front and a lower and rounder peak compared to the sensor of smaller size and lower response time.

The limitations of the pressure gauge is thus the main cause of the discrepancy between the experimental and numerical results of table 4.5. Cole [50] reported that measurements of the blast wave produced by a 25 g explosive charge had an error of 17% for the peak pressure and Zhou et al. [60] reported lower peak pressures for the PCB sensor ranging from 9% up to 27%. Several studies considered reconstruction techniques for obtaining the correct blast wave from the gauge data but these have been application specific and are validated by actual measurements using sensors of higher specifications. A study of the blast wave using sensors of ns response time and large frequency bandwidth would be beneficial in revealing the true characteristics of the blast wave produced by detonators.

4.5. The nature of the blast wave

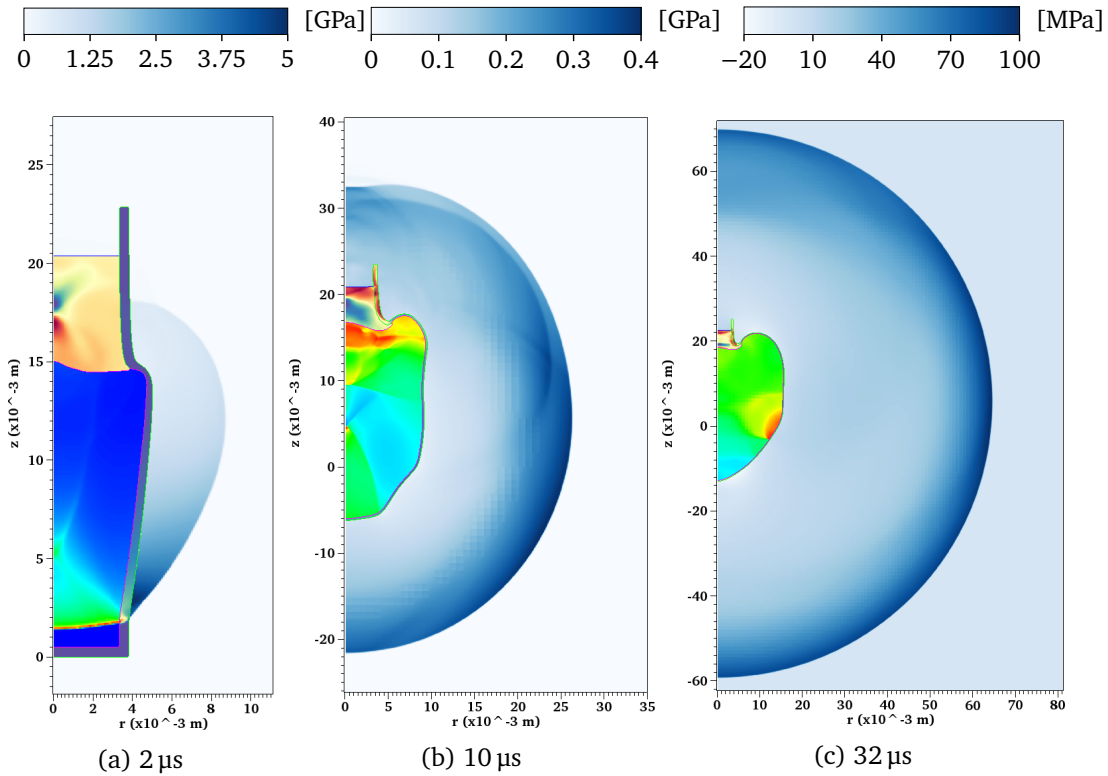


Figure 4.6: Plots of pressure from the numerical solution of the blast wave generated by the detonation of the explosive charge in a detonator with 0.5 mm aluminium shell. The blast wave is asymmetric in the near field and becomes progressively more spherically symmetric as it expands.

4.5 The nature of the blast wave

We examine the blast wave produced by a detonator placed underwater. This configuration has an aluminium shell of 0.5 mm in thickness and a base charge of 700 mg of PETN which is sealed by a copper cup placed on top of it. Figure 4.6 shows selected times in the formation and expansion of the blast wave. Initially, the blast wave is ellipsoidal due to the geometry of the charge. The major axis of the ellipse is in the direction of the axis of symmetry of the detonator and the blast wave is stronger and faster in this direction. As the blast wave expands, the magnitude of the shock decays at different rates in each direction and eventually, the difference between the axial and normal direction is minimized, leading to a spherical blast wave.

The initial stages of the blast wave are characterized by a complex wave structure which varies along the front of the blast wave. As can be seen in figure 4.6b, certain

4.5. *The nature of the blast wave*

sections of the blast wave show additional wave fronts behind the primary blast wave which have higher pressures than the leading blast wave. These secondary waves are produced by the internal reflections inside the base charge and shell of the detonator. Hence, the generated blast is formed by the coalescence of several blast waves of different strength and radii. As these expand, they equilibrate and form a regular blast wave with a single shock discontinuity followed by falling flow parameters.

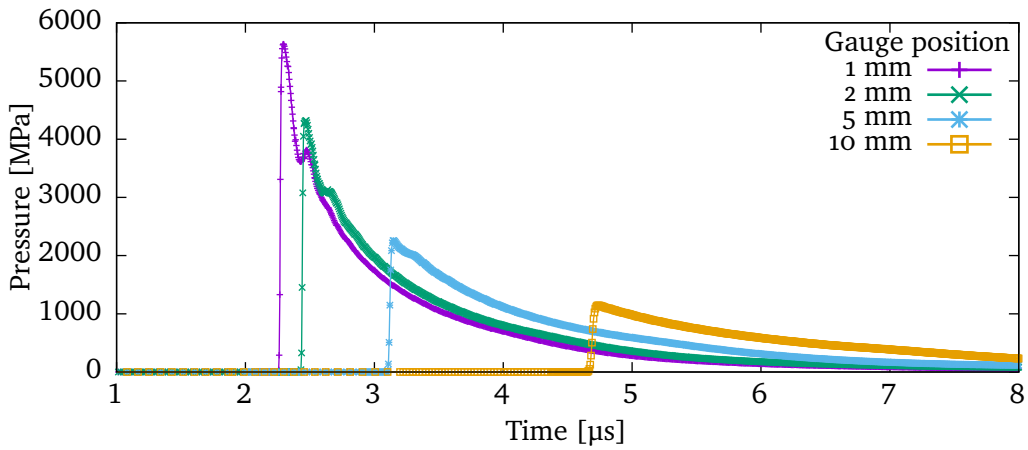
Along with the formation of the blast wave, the shell and cup of the detonator are compressed and deformed by the detonation wave and the expanding gaseous products. Initially, the detonation propagating in the base charge pushes the surfaces of the shell in the normal and axial direction, causing the formation of an inverse corner. Then, the isotropic expansion of the products takes over and causes extreme elongation of the metal shell while leading to a more rounded shape that persists until the late stages. The metal cup is also compressed but is significantly less deformed compared to the shell of the detonator. Since the mathematical formulation does not include a fracture model, the metal flows without breaking which would be expected in these conditions.

The pressure traces from the gauges positioned along the normal direction are shown in figure 4.7. The explosion of the detonator produces a pulse in the water with peak pressure of almost 6 GPa at a distance of 1 mm from the side of the detonator. As the wave propagates to larger distances, the peak pressure falls and the pulse width increases. In the first few mm (near field), the blast wave shows two peaks resulting from reflections of the shock wave within the metal shell. The first peak has larger magnitude and travels faster than the following peak. As they propagate, the peaks move away from each other and are eventually incorporated into a single peak blast wave at a distance of approximately 10 mm.

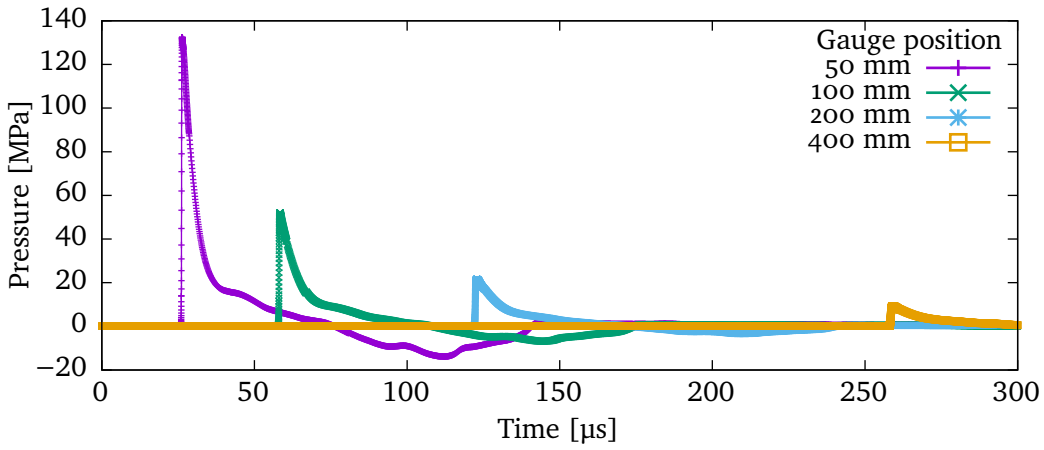
The pressure pulse in the axial direction is significantly stronger and has peak pressure of more than twice the values in the normal direction as can be seen in figure 4.8. This means that the blast wave is also faster in this direction which leads to the ellipsoidal shape of the blast wave with the major axis in the axial direction. The difference between the strength of the blast wave in the two directions persists until approximately 10 mm where the magnitude of the blast wave is approximately 1 GPa in both directions, but the blast wave has not attained a spherical front yet. Further, the blast wave in the axial direction also exhibits a secondary peak of lower magnitude. Similar to the normal direction, the two peaks move away from each other as they expand and eventually form a regular blast wave, but are seen to persist longer in this direction.

The decay of the peak pressure of the blast wave with distance is plotted in figure

4.5. The nature of the blast wave



(a) Near field



(b) Far field

Figure 4.7: Pressure plots of the blast wave measured at several points along the direction normal to the axis of symmetry of the detonator.

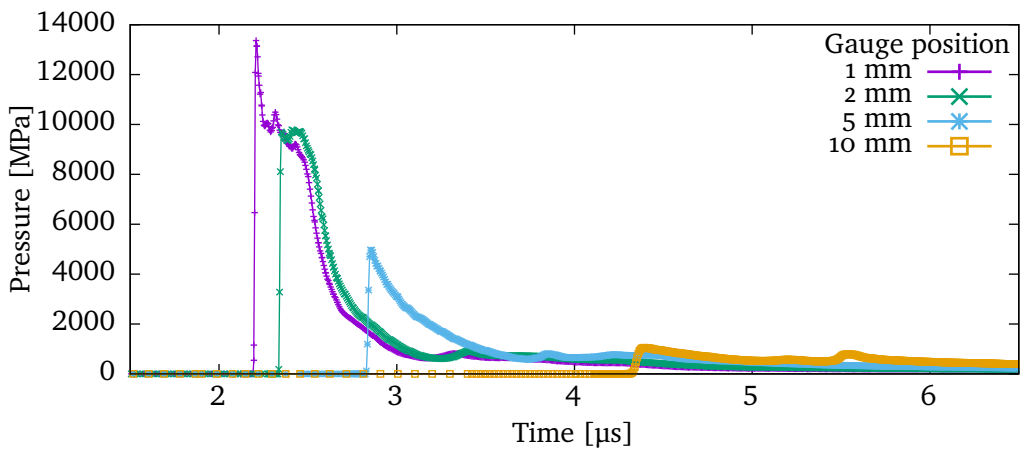


Figure 4.8: Plots of pressure obtained by gauges at several distances in the axial direction.

4.5. *The nature of the blast wave*

4.9. The plot compares the two directions considered and illustrates the persistence of higher peak pressure in the axial direction up to the distance of 10 mm where the peak pressure in both directions becomes similar. At larger distances, the blast wave in the normal direction exhibits slightly higher values, suggesting a slower rate of decay compared to the axial blast wave. Overall, the decay behaviour exhibits a similar trend in both directions. It starts with a slow decay rate which increases as the blast wave expands and reaches an approximately constant power law decay at the larger distances.

There is a clear distinction in the decay behaviour between the near and far field. The initial decay of pressure is not linear in the log-log plot and therefore cannot be described by a single power law. In addition, it is slower than the inverse first power law (r^{-1}). This behaviour has been observed in experiments and is a result of the finite time required for the energy transfer from the explosive to the surrounding material [61, 62]. The extent of this formation process depends on the ratio of energy release over the initial mass of the explosive. Brode [63] suggests that for a conventional explosive (TNT), the blast wave has fully formed when its radius engulfs a mass of the surrounding material that is roughly ten times the mass of the explosive. In the case of 700 mg PETN and water, which are considered in this study, this distance is at approximately 12 mm. This is the distance at which the change in the decay rate is observed in figure 4.9.

In the far field, the decay rate is increased and resembles a power law. A fit of the obtained peak pressures in the normal direction yields a power value of $-1.321(7)$ which also describes the axial values well. A value of higher than the inverse power law is expected for strong shock waves [50]. The rate of decay in this regime depends on the amplitude of the wave. The dissipation of energy at the shock front increases with shock pressure, therefore there is smaller loss of energy as the blast wave expands and its peak pressure is reduced. This explains the lower decay rate of the blast wave in the normal direction which has lower pressures in the near field and thus dissipates less energy as it expands. At even longer distances, the blast wave becomes an acoustic wave and the decay is expected to reduce further and converge to the inverse first power law which is the asymptotic solution for spherical acoustic waves.

It should be noted that the classic Sedov-von Neumann-Taylor similarity solution for a point source explosion predicts a decay rate of r^{-3} . However, as mentioned in the original work of Taylor [61], the range at which this solution can be compared to actual high explosives is limited. Firstly, the solution concerns point sources instead of an extensive explosive charge. This assumption sets a lower limit for the distance from the explosive charge that the solution applies, which is at the point where the involved mass

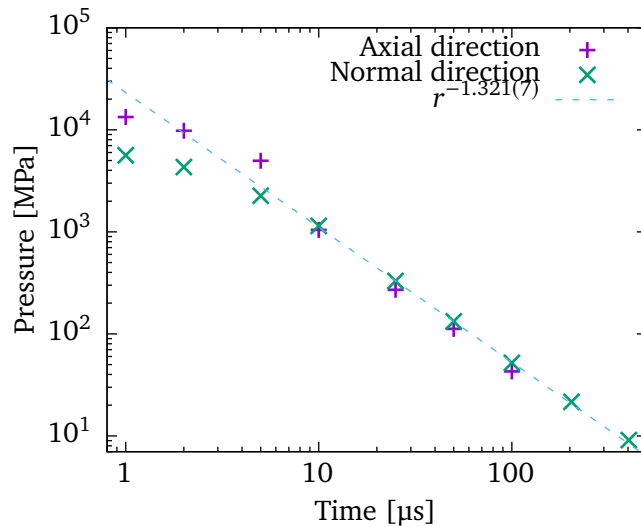


Figure 4.9: Logarithmic plot of the decay of peak pressures of the blast wave with distance in the two directions considered.

of the surrounding material is several times the explosive mass. Secondly, an upper limit is also introduced from the assumption of strong shock waves. Taylor [61] suggests that the solution is valid for shock pressures above 1 MPa in air. This corresponds to shock waves travelling with speed above Mach 3 or shock pressure of above 4.2 GPa in water. Shock waves of such strength are not observed after the blast wave has expanded beyond the lower limit and therefore, there is no range in which the similarity solution is applicable for the blast wave produced by the underwater detonator.

The differences in the nature of the blast wave in the near field compared to the far field should be considered in the assessment of the initiation capability of a detonator. Most experimental tests, including the widely used test specified by the European standard, consider only a single point in the far field. However, the asymmetric blast wave strength and low decay rate, that characterize the blast in the near field, do not persist in the far field. In addition, the overall decay rate is different between the two directions considered. The axial blast wave has higher pressure in the near field but decays faster and exhibits comparable and even slightly lower values of shock pressure than the normal direction in distances beyond 10 mm. Given that the initiation of the neighbouring explosive is heavily dependant on the shock pressure in the near field, tests that consider the blast wave only in the far field will not accurately capture the initiation capability of the detonator.

4.6 The effect of shell material

The material of the detonator shell is an important aspect of detonator design. The most commonly used metals are aluminium and copper, but manufacturers have been introducing new metal alloys in an effort to balance the requirements for low cost, efficiency and reliability. Experimental studies have shown that the initiation capability of the detonator is influenced by the type of the shell [42, 44], but the physical mechanism behind this effect is not well understood. The significance of the material of the shell is also evident when considering the physical processes involved in the generation of the blast wave. The detonation wave initiated in the base charge, induces a shock wave in the metal shell and subsequently in water through a series of transmissions and reflections at the material interfaces which depend on material properties. This section compares the blast waves generated from detonators of different metal shell in order to identify the nature and extent of the influence of the detonator shell.

The materials considered are aluminium, copper and steel. They differ in density with aluminium being the lighter (2710 kg m^{-3}) whereas copper (8930 kg m^{-3}) and steel (8030 kg m^{-3}) have approximately three times larger density. The materials also have different sound speed with copper having the lowest value (4600 m s^{-1}), aluminium the highest (6220 m s^{-1}) and steel approximately in the middle (5680 m s^{-1}). These translate to different specific acoustic impedance values which is a quantity that determines the ratio of transmitted and reflected wave at an interface. Lastly, these materials also differ in terms of yield strength. Copper has the lowest yield point at 140 MPa and will exhibit more plastic deformation, followed by aluminium (298 MPa) and steel (1370 MPa) which has the highest value.

The flow field after the initiation of the copper detonator is shown in figure 4.10. The generated blast wave is initially ellipsoidal and progressively transforms into a spherical wave as it expands, as in the case of the aluminium shell. However, the initial wave transmitted in water (figure 4.10a) is seen to have multiple secondary peaks of equivalent strength. This is caused by strong reflections at the interfaces of the shell and leads to typical reverberations or 'ringing' in the metal [64]. Once the reactions in the explosive have completed, the resulting blast wave has a complex structure and variable strength along its front which was observed in all materials. The deformation of the cup and shell is similar to the aluminium case for times up to $10 \mu\text{s}$. In later times, the copper shell continues to feature the inverse corner and has more anisotropic expansion compared to aluminium due to lower yield strength leading to more extensive plastic

4.6. The effect of shell material

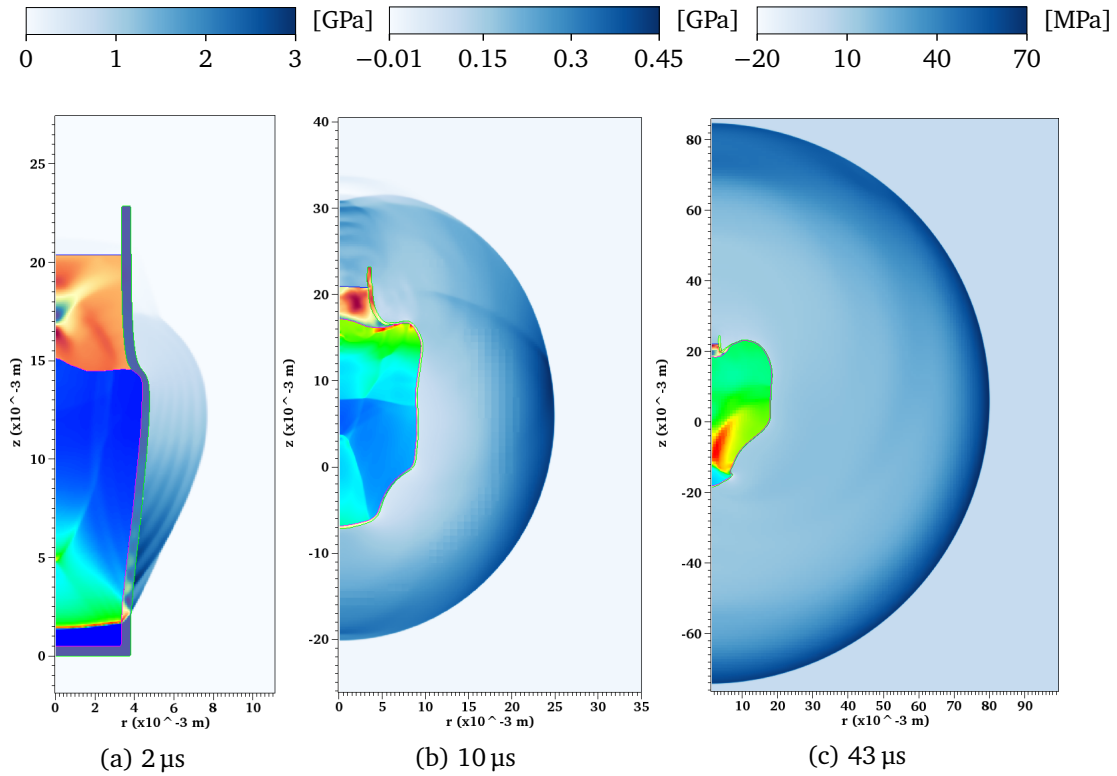
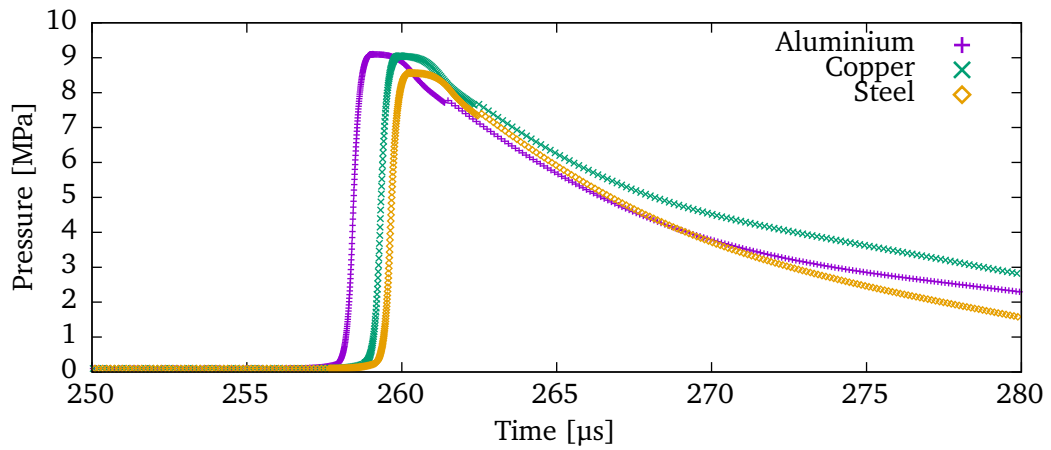
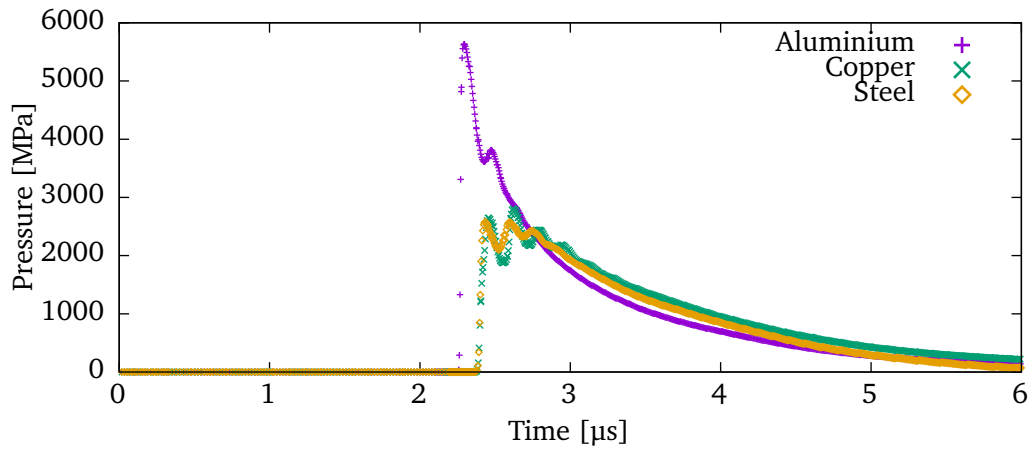


Figure 4.10: Plots of pressure from the numerical solution of the blast wave generated by the detonation of the explosive charge in a detonator with 0.5 mm copper shell. The blast wave is asymmetric in the near field similar to the aluminium case, but the internal reflections lead to multiple peaks of approximately half the strength of the blast wave generated in the case of aluminium.

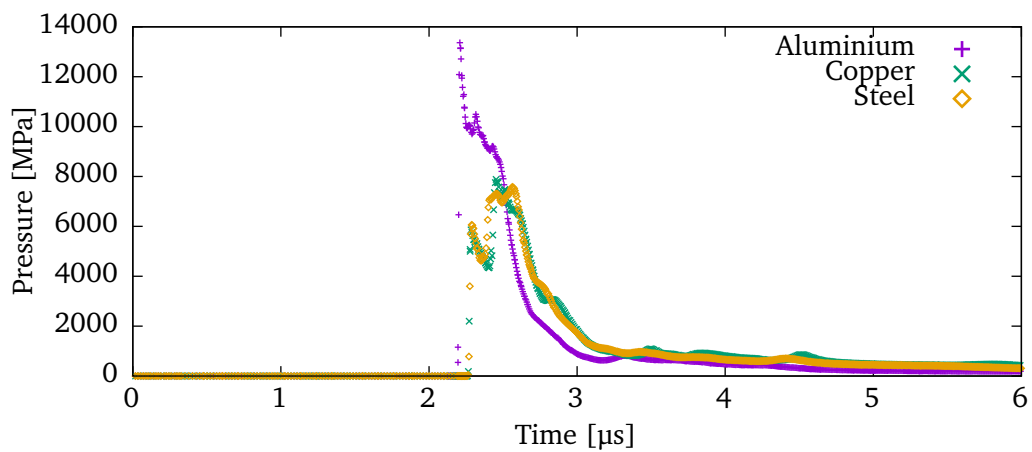
4.6. The effect of shell material



(a) 400 mm in the normal direction



(b) 1 mm in the normal direction



(c) 1 mm in the axial direction

Figure 4.11: Comparison of the pressure pulse generated underwater for 0.5 mm thick detonators for different shell materials.

flow.

The comparison of the pressure pulses obtained at selected points in the near and far field of the detonators is shown in figure 4.11 for the three shell materials examined. The three materials show little variation in the generated blast wave when observed in the far field but have stark differences in the near field. The peak pressure for the copper and steel detonators at the distance of 1 mm is a little over 2.5 GPa which is half the value of the aluminium detonator. Similar behaviour is observed in the axial direction. The pulse of the aluminium detonator has almost double the pressure peak of the copper and steel detonators.

Furthermore, the copper and steel detonators also feature multiple peaks which are a result of stronger reflections of the shock wave within the copper/steel shell. This is caused by the higher impedance difference of copper/steel and water which means that the shock wave is mostly reflected at the interface of metal and water and only a small portion is transmitted outside. The shock wave is also reflected at the inner interface between metal and explosive products where the impedance mismatch is also large. This results in more pressure peaks of lower amplitude compared to the case of aluminium case.

As the blast wave expands to larger distances, the stronger pressure peaks merge with the slower ones ahead while the weaker ones behind decrease further and are incorporated into the tail of the blast wave. After this equilibration process, only a single peak remains. At the distance of 400 mm the blast wave has peak pressure of around 9 MPa for both aluminium and copper and slightly lower for steel.

Figure 4.12 shows the decay of shock pressure with distance in the normal direction for all materials considered. The higher peak pressures observed in aluminium extend to a distance of 10 mm while copper and steel exhibit similar peak pressures and decay. At larger distances the blast wave from all configurations shows nearly identical values of pressure and the decay rate specified by the power law $r^{-1.321(7)}$ describes all materials within error. Similar results are observed for the blast wave in the axial direction.

Overall the blast waves from these configurations are seen to differ only in the near field. As the wave expands, the blast waves converge and they are practically the same at the distance of 400 mm. As a result, the shock energies measured at this point would be similar for all detonators which would mean that they have equivalent initiation capability, according to the European standard test. However, the strength of the shock is the leading factor in the initiation of heterogeneous solid explosives [65, 66]. The initial pressure pulse must be above a threshold to ensure the reliable initiation of

4.7. The effect of the shell thickness

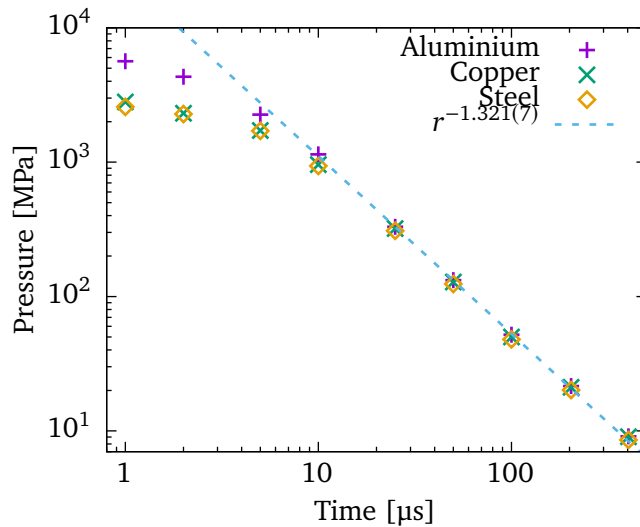


Figure 4.12: Logarithmic plot of the decay of peak pressure of the blast wave with distance in the direction normal to the detonator and for the three materials considered.

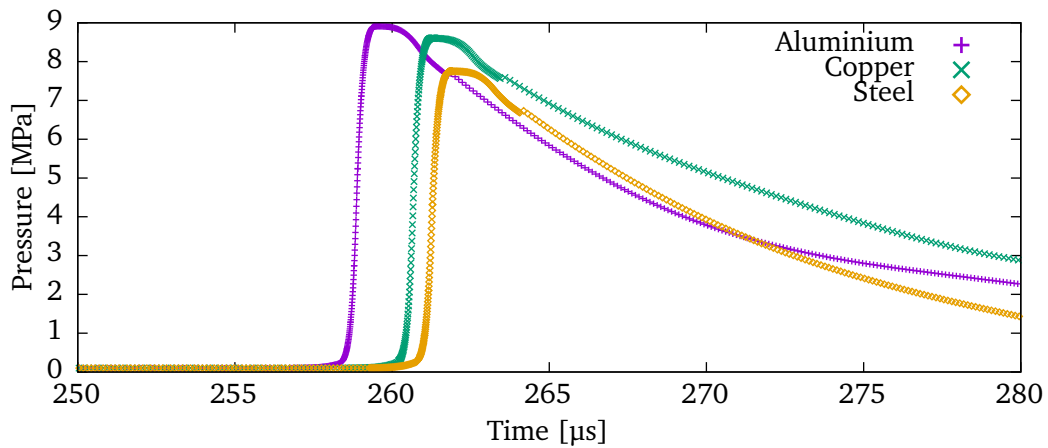
the explosive and thus, the reduced peak pressure of the copper and steel detonator indicates lower capability in the initiation of secondary explosives. In addition, the weak blast wave can also lead to effects of shock desensitization which is common in heterogeneous secondary explosives. The important differences in the near field are not accounted for by tests that focus on the far field performance which suggests limited suitability for assessing initiation capability.

4.7 The effect of the shell thickness

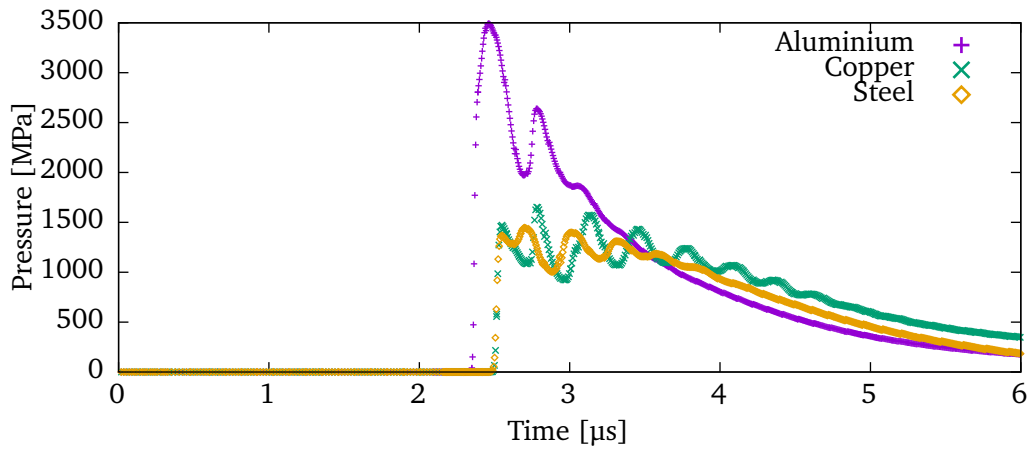
This section examines the effect of shell thickness on the blast wave generated by detonators. The mass of the shell, determined by its thickness, is expected to affect the equivalent energy yield of the device because the explosive charge and the shell have comparable masses [51]. We consider detonators of 1 mm in shell thickness which is double the value of the previous configurations and made out of the same three different materials as in the previous section.

The plots of figure 4.13 compare the pressure pulse calculated for the thick detonators at selected points. Interestingly, the blast wave in the far field (400 mm) is not considerably different from the case of the thinner detonators. In particular, the pressure pulse of the aluminium shell is largely similar and for copper and steel the reduction in peak pressure is approximately 5%. The increased effect for the case of

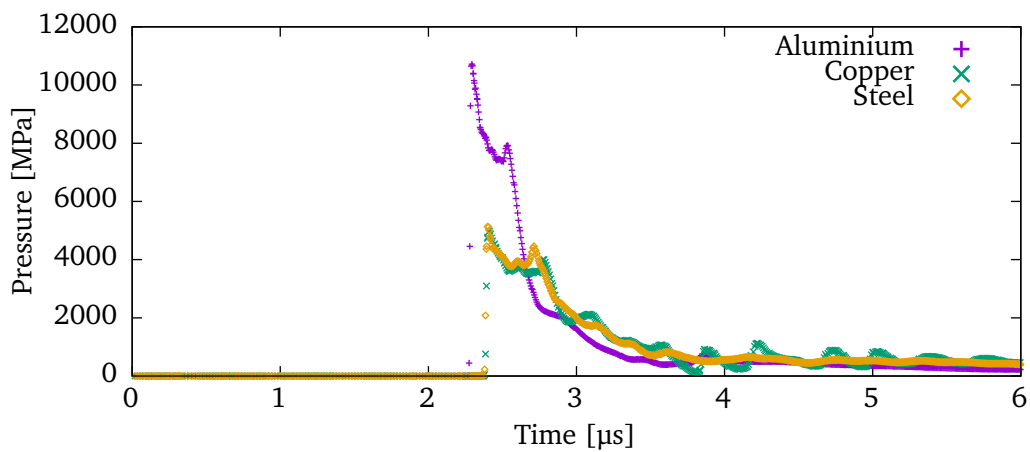
4.7. The effect of the shell thickness



(a) 400 mm in the normal direction



(b) 1 mm in the normal direction



(c) 1 mm in the axial direction

Figure 4.13: Comparison of the pressure pulse generated underwater for 1 mm thick detonators for different shell materials.

4.7. The effect of the shell thickness

copper and steel detonators is caused by the fact that the increase in mass is much larger for these denser materials compared to aluminium.

In the near field, the relative differences between materials are also similar to the previous section. The aluminium detonator generates pulses of approximately double in pressure than copper and steel which have similar values. The existence of multiple peaks in the case of detonators made out of high impedance materials (copper/steel) is also observed, but the period of the oscillations is now larger due to the increased thickness and hence the larger time between reflections within the shell.

The increased shell thickness does however cause a significant reduction in the strength of the pressure pulses observed in the near field. All materials show decreased pressure pulses with the most extreme cases being the reduction of the pulse strength in the normal direction. The pressure peaks for this case have reduced to almost half. However, the reduction in the axial direction is less severe, with the aluminium reducing by 20% and the copper and steel by 35%.

An additional distinction to the case of thin detonators is the difference between the pressure pulses in the axial and normal direction which is larger for the thick detonators. In the 0.5 mm thick shells, the pulse in the axial direction had approximately twice the peak pressure in the normal direction, but for the shells of 1 mm this increases to three times larger pressure peaks.

A comparison of the decay of peak pressure of the blast wave between the thin and thick detonator is shown in figure 4.14 for the case of the aluminium shell. The plot shows that they deviate only in the near field where the doubling of the thickness leads to approximately halving of the pressure peak. However, at distances beyond 10 mm the shock pressure is similar for detonators of both thicknesses. This indicates that the mass of the shell mostly affects the formation regime of the blast wave. Once the energy of the explosive has been transferred to the surrounding material, the generated blast wave is similar for both sizes of detonator shell.

Overall, the results indicate that the increased thickness of the shell leads to a significant reduction in the near field pressure values. This suggests that the detonator will have lower capability in igniting an explosive. However, the impact of the shell thickness does not persist into the far field which follows the theme that is observed in the previous sections. Thus, direct initiation capability tests that consider the blast wave only at the far field are not able to fully capture the effect of the shell thickness and will demonstrate little difference in performance between the thin and thick detonators.

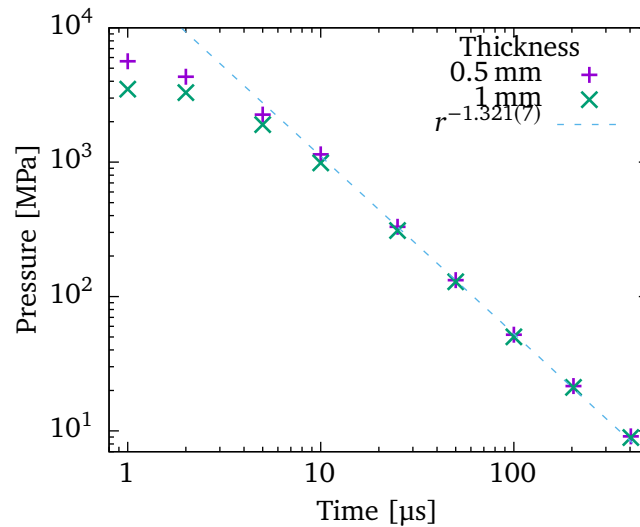


Figure 4.14: Logarithmic plot of the decay of peak pressure of the blast wave with distance in the normal direction for aluminium detonators of different shell thickness.

4.8 Conclusions

This study investigates the blast wave generated by a detonator underwater and follows the initiation capability test described in the European standard [11]. This is a direct test of initiation which has not been shown to correlate with the actual initiation capability of the detonators. However, it is widely used for assessing detonators and there exist experimental data for it which motivated its use in this study. The aim is twofold, to study the blast wave generated by different types of detonators and also to examine potential shortcomings of using this test for estimating the initiation capability of detonators.

The design of the detonators is based on actual devices produced by Orica and is also similar to the design of the reference detonator provided by the European standard. The explosive used in detonators is usually highly porous because of the manufacturing methods. In the case of the Orica i-kon II detonator, the density is 1.5 g cm^{-3} which is 16% lower than the maximum density of PETN. This prompted the use of a porosity model and the adjustment of the reactive parameters to match experimental CJ values for this density.

The numerical solution is validated against the experiments of Klapötke et al. [12] which used detonators of 500 mg and 700 mg of PETN of the same density as mentioned above. The numerical results show higher pressure peaks and larger shock energy

4.8. Conclusions

than measured experimentally. This is attributed to imperfections of the experimental pressure measurement equipment. An experimental study by Zhou et al. [60] examined the same pressure gauge used in the experiments of Klapötke et al. and showed that piezoelectric sensors distort the pressure pulse due to their size which results in increased rise times and reduced pressure measurements as was the difference between the numerical and experimental results.

The numerical solution of a blast wave generated by a detonator underwater shows distinct features between the near and far field of the detonator. In the near field, the blast wave has an ellipsoidal shape and is twice as strong in the axial direction than in the normal direction. In addition, this region is where the blast wave goes through its formation regime which is characterized by a slow rate of decay. Once the blast wave has engulfed a large portion of the surrounding water, it is considered established and exhibits a faster rate of decay which follows a power law. Finally, as the blast wave propagates into the far field, the variability of its strength with direction is minimized and attains a spherical shape.

The analysis into the effect of the metal shell on the generated blast wave has revealed a common theme. The blast waves produced by the different types of detonators can have significant differences in the near field, but these are minimized after the expansion of the wave into the far field. The results show that the pressure pulse in the far field is similar for all shell materials. In the near field however, the blast wave is critically different for the case of aluminium which produces a pressure pulse with double the peak pressure of the denser metals, copper and steel. This is caused by the larger impedance difference between the water and copper/steel which leads to stronger reflections within the metal shell and results in blast waves with multiple peaks. The impact of the thickness of the shell also follows the same theme. In the far field, the aluminium detonators show very similar pressure pulses for both thin and thick detonators and for the thicker copper and steel detonators, the reduction in peak pressure is approximately 5%. Contrary to that, the near field peak pressure of the pulse is reduced to half in the normal direction and by 20%-35% in the axial direction for all thicker shells.

The distinct features of the blast wave in the near field play an important role in the initiation capability of detonators because the initiation of heterogeneous explosives is believed to depend primarily on the strength of the blast wave. In addition, the experimental observations of the lower effectiveness of copper detonators compared to aluminium as well as the change in initiation capability depending on the orientation of the detonator can be explained by considering the differences in the strength of the

4.8. Conclusions

pressure pulse in the near field. However, this variation in the generated blast wave does not persist in the far field and is not captured by tests that examine the blast wave only in the far field. These tests, such as the standard underwater test, would show similar performance for most detonators which suggests that they are not able to fully assess the effectiveness of a detonator.

The outcomes of this work highlight the need for experimental studies that consider the full extent of the blast wave. These require advanced experimental techniques that are able to capture the short timescales and multi-dimensional character of the blast wave in the near field. Recent studies have proposed the use of high-speed imaging and optical techniques [43] which are able to measure the near field blast wave strength and its variation with direction. A detailed description of the blast wave obtained from accurate experimental data will provide invaluable insight into the properties of the blast waves generated by detonators and can be used to validate the results of numerical studies. Lastly, the utilization of leading experimental techniques will also pave the way for the development of improved tests that will provide a more comprehensive evaluation of detonator performance.

The development of new tests will also have to be supported by experiments that confirm their ability to capture the initiation capability of a device. This is required for all direct tests that consider the detonator in isolation. In particular, for the class of tests that consider the blast wave generated by a detonator, it must be examined whether the distinct features of the blast waves produced by each type of detonator correlate with their actual initiation capability. Theoretical considerations of shock initiation of heterogeneous explosives support this connection but it must also be verified through indirect tests that place the detonator within an explosive. These experiments will reveal the impact of each aspect of detonator design on the initiation capability and will allow to evaluate the suitability of a direct test in assessing it.

The next chapter extends the numerical investigation by considering the detonator within a booster. This configuration is used to initiate mining blastholes but can also be viewed as an indirect test of initiation capability. The aim is to examine the performance of the booster and compare the initiation capability of the detonators in the actual configuration that they are designed to operate in.

4.8. *Conclusions*

Chapter 5

Performance evaluation of boosters

5.1 Introduction

Mining operations involve drilling holes in the rock, filling them with explosive and igniting them in a specific pattern designed to increase the efficiency of rock fragmentation. The explosive that is most commonly used by the mining industry is ANFO (Ammonium Nitrate mixed with Fuel Oil). It is a very insensitive explosive that has beneficial safety and usability characteristics, in addition to low cost. However, its detonation is highly non-ideal with low detonation velocity and poor performance in small diameters. It requires strong stimulus for initiation and is recommended to use a three-step initiation train which includes a detonator and a booster.

A booster is an explosive device that is part of the three-step explosive initiation train. It provides an additional explosive layer between a detonator and a tertiary explosive to ensure reliable initiation of non-detonator-sensitive explosives. As such, it has to be sensitive enough to be ignited by a detonator and powerful enough to provide a sufficient impulse for the ignition of insensitive tertiary explosives such as ANFO. Similar to detonators, these devices exist in several designs which have different types and quantity of explosive as well as shell material and shape. Their industrial design must satisfy a long list of specifications which relate to safety, cost and ease of use which inevitably leads to compromises in performance.

The study is motivated by the need to assess the performance of these initiation devices. The detonator and booster configuration have a complex structure which encumbers any analytical efforts to predict the behaviour of the detonation. Further, this study is also an extension of the investigation of the previous chapter. As mentioned, the estimation of the initiating capability of a detonator can be conclusively assessed

5.1. Introduction

only through experiments involving the explosive it is meant to ignite. In this chapter, the detonator and booster configuration will be also considered as the simulation of an indirect test for the initiation capability of the detonators.

The studied configuration includes a detonator which is placed within a secondary charge. The booster explosive is less sensitive than explosives used in detonators and is usually a heterogeneous explosive that can exhibit shock desensitization. The initiation process begins with the ignition of the detonator where a detonation is quickly established. As it propagates, it generates shock waves in the metal confinement which are transmitted in the secondary explosive. If these shock waves are not strong enough to ignite the explosive, they might desensitize it and lead to the formation of a dead zone within the explosive of the booster. Extensive dead-zones will obstruct the propagation of the detonation and can be detrimental to the performance of the booster.

The impact of shock desensitization on mining operations has been considered in several studies by the mining industry. The investigations have mostly focused on the effect of shock waves from neighbouring blasts in situations where multiple blastholes are initiated sequentially [67, 68, 69]. The generated shock waves travel through rock at high velocities and can reach adjacent blastholes ahead of their initiation. Depending on the strength of the shock, this can cause an untimely initiation of the blasthole or desensitization of the explosive and loss of performance of the blast. In addition, it has been observed that the shock wave can also interfere with the initiating devices such as the detonator [70] and render them unable to initiate the blasthole.

Shock desensitization can also influence the initiation of the booster by the detonator. Orica performed internal experimental studies, called aquarium tests, in which they used ultra-high-speed photography to capture the initiation of a commercial booster placed underwater. They made observations of the detonation front on the surface of the booster which demonstrated the complex initiation process as well as indicated that certain regions of the explosive are desensitized, leading to the formation of dead-zones. This is also recognized in accompanying numerical investigations in which it was observed that several regions were not promptly ignited when shocked, because of low shock strength, and would have been desensitized. However no desensitization was included in the mathematical model to allow for the complete study of the effect.

The heterogeneous nature of the explosives and the geometry of the booster indicate that its initiation can be affected by shock desensitization. As seen in the previous chapter, the blast wave obtained by the detonator has variable strength along its front which can cause the initiation of a region of the explosive while other regions are

5.2. Shock desensitization of solid explosives

desensitized by the weaker parts of the blast wave. However, experimental studies investigating the initiation of a booster device do not exist in the literature. Experiments utilizing x-ray or proton radiography can be performed to analyse the extent of reactions within the detonator and booster configuration and provide valuable insight into the influence of shock desensitization during the initiation of the booster.

This study employs numerical simulations to study the detonator and booster configuration based on a design that is used by the mining industry. We consider the detonators used in the previous chapter inserted within the booster device and examine their ability to initiate the booster explosive as well as the effect of shock desensitization on this process. The reactive model is extended with a desensitization model to account for the effect of shock desensitization. This extension is required for the Ignition and Growth model to capture dead zone formation as has been shown by previous studies [23, 14]. The shock desensitization effect and the related model are discussed in the next section along with extensive validation. Following this, the booster configuration is presented and examined in several configurations. The study considers the initiation process of the booster with and without the desensitization model, for different types of detonators, and for a case of different positioning of the detonator.

5.2 Shock desensitization of solid explosives

Shock desensitization is the phenomenon where the sensitivity of an explosive is decreased by the passage of a shock wave that is not strong enough to ignite it. The degree of desensitization increases with the strength of the shock and can have different manifestations depending on the setup. For example, desensitization effects include the delay of shock to detonation transition in the case of double shock initiation and the quenching of an established detonation when it encounters a desensitized region.

The physical processes behind this phenomenon are quite intricate and despite studies spanning over five decades, there has not been a consensus on the underlying causes. However, it is a subject of great interest to the explosives community because of its wide reaching implications ranging from being a useful safety feature for rendering explosives difficult to initiate to being a highly undesirable effect in applications concerned with the performance and efficiency of explosive devices.

Shock desensitization of solid explosives was first mentioned in a study by Campbell et al. [71] in which they performed experiments on shock initiation of heterogeneous explosives. The authors observed that the layer of the explosive which was first to

5.2. Shock desensitization of solid explosives

experience the shock did not proceed to complete reaction and it was deduced that the shock had desensitized that region.

Subsequent investigations have distinguished between different manifestations of shock desensitization [72, 5]. In the context of shock initiation, desensitization is observed in double (or reflected) shock initiation where there is a delay in the transition to detonation of the explosive compared to single shock case. This suggests that the first shock has desensitized the explosive making it harder for the second shock to ignite it. When considering detonation propagation, shock desensitization is expressed as the quenching of detonation in parts of the explosive that have been previously shocked. In many occasions, detonation will propagate around these regions and will leave portions of non-reacted or partially reacted explosive, commonly called “dead zones”.

Multiple experimental studies have investigated shock desensitization and a useful aggregation of the experimental evidence is provided in the study of Hussain et al. [72]. Double shock initiation experiments have found that if the first shock induces no reactions by the time the second shock catches it, then the time or distance to initiation is increased. However, when measured from the catch point, it is almost the same as initiation from a single shock of the same pressure as the second one. In cases where the second shock never overtakes the first, such as in reflected shock scenarios, no reactions are induced in the explosive. This suggests that the initiation of an explosive requires a single shock of strength above a certain threshold, while splitting it to multiple shocks will not ignite the explosive even if the final shock is above the initiation threshold.

On the aspect of detonation quenching, Drimmer and Liddiard [73] performed one of the first experiments involving detonation failure in pre-shocked HMX-based explosives. Campbell and Travis [74] performed similar experiments on RDX-based explosives and more recently Vandersall et al. [75] studied the interaction of detonation with weak shocks in TATB-based explosives. All studies reported that detonation degenerated into an inert shock for a range of pre-shock pressures that were weak enough not to induce reactions in the explosive. However, detonation did proceed for shock pressures below a minimum value. The studies concluded that desensitization is a time dependant phenomenon where strong shocks lead to faster desensitization and by extension, faster failure of detonation.

Advances in experimental diagnostics have enabled the study of dead zone formation and have shown that they occur for all polymer bonded explosives [5]. The usual setup used in such studies involves an abrupt change in geometry such as an increase in charge radius which forms a corner. As the detonation moves into the wider explosive region, it is diffracted and may propagate in the radial direction usually referred to as

5.2. Shock desensitization of solid explosives

“turning the corner”. In most cases, the detonation in the radial direction is established at some distance from the corner which results in some parts of the explosive not reacting. Cox and Campbell [25] performed one of the earliest experiments involving detonation diffraction and reported dead zone formation in TATB-based explosive. Similar experiments performed by Held [76] showed dead zone formation in an RDX-based explosive.

The formation of dead zones in charges with sharp corners is a result of a weak shock propagating radially as the detonation expands into the wider explosive region. This shock is not strong enough to induce prompt reactions and results in desensitizing the explosive. The detonation continues to propagate in the initial direction as well as expanding radially, at a rate faster than the weak shock. It eventually reaches the outer boundary of the corner but it is unable to penetrate the desensitized region resulting in a pocket of non-reacted explosive. The dead zone is more extensive if the corner is covered with a high sound speed confining material. In this case, the shock wave formed in the confining material is transmitted into the explosive region along the corner much earlier than the detonation is able to diffract and reach it. This results in the desensitization of a large region of the explosive along the corner which might not be consumed by the detonation.

The processes involved in the formation of dead zones are the result of the complex interactions between the rarefaction, shock, and detonation waves. The resulting size and shape of the dead zone is heavily dependant on the fine details of relative timings and strengths of these interactions. As mentioned in the review paper by Handley et al. [5], detonation diffraction experiments are very sensitive to initial conditions and explosive composition and show significant variability between similar experiments. This sensitivity is observed in the numerical simulations as well which has made this class of experiments an ideal case for assessing the accuracy and capabilities of reactive models.

All of the effects of shock desensitization described above have been explained by the simple notion that shocks which are too weak to induce reactions will instead desensitize the explosive and that the degree of desensitization will vary depending on the strength of the shock. However, the underlying cause of shock desensitization of explosives is still debated between two concepts.

The classic view [74, 77] considers the hotspot mechanisms and advocates that the weak first shock activates the hotspots in the explosive to a small degree that does not lead to hotspot coalescence and ignition. When the second shock arrives, the hotspots are no longer available and initiation fails. This view resides heavily on the

5.3. *Mathematical model of desensitization*

pore collapse mechanism for hotspot generation and it is assumed that the majority of the pores are closed by the first shock making them unavailable to subsequent shocks. In this view, desensitization is a time dependent effect since certain time is required for the shock to activate the hotspots, similar to the induction time.

The second hypothesis has been proposed by James and Lambourn [13] and is based on thermodynamic and hydrodynamic arguments. In this view, desensitization arises naturally when assuming that the reaction rate depends on a thermodynamic quantity that is greatly reduced behind multiple shocks compared to a single shock. Such a thermodynamic variable can be temperature or entropy which can be shown to raise significantly less than pressure behind subsequent shocks and do not provide sufficient stimulus for ignition. The observed time dependence of the desensitization is then explained as hydrodynamic effects resulting from the reduced reaction rate and will also be different depending on how the desensitization manifests, e.g. delay in run to detonation or detonation quenching. This view is supported by simulations using temperature and entropy based reaction rates which naturally capture the desensitization effects as will be discussed in the following section.

The main difference between the two hypotheses is that the classic view considers the cause of desensitization to be a physical change in the structure of the explosive which is time dependant, while the new view assumes that the reaction depends on a thermodynamic quantity that is not sufficiently increased by secondary shocks. Further experimental and numerical investigations are required for settling this debate which is related to the need for a deeper understanding of the shock initiation mechanisms in solid explosives. It is also possible that the two concepts are not competing, as they have been presented, but are in fact compatible and can be fused to provide a complete picture of the desensitization processes. It should be noted that A.W. Campbell who introduced the idea of the deactivation of hotspots, also mentions the reduction of shock temperature as a cause of the higher induction times in double shock initiation [74].

5.3 Mathematical model of desensitization

The traditional development of reaction models relies mostly on run to detonation and velocity of detonation experimental data for their calibration. Effects of shock desensitization such as delayed initiation or dead zone formation were not considered. Owing to better diagnostic methods and to a range of new experiments involving desensitization effects, there has been an increased interest in investigating the capabilities of reactive models on such configurations. The wealth of experimental data produced is being

5.3. *Mathematical model of desensitization*

used to assess, calibrate and develop new reaction models.

Popular pressure-based reaction rates, such as I&G have been quite successful in matching shock initiation and detonation propagation experiments, but have been unable to capture desensitization effects. Aslam et al. [78] evaluated different reactive models by comparing them with experiments of multiple shocks and isentropic compression of PBX-9502. These experiments generated pressures of more than 20 GPa in the explosive which would normally cause a prompt run to detonation if attained through a single shock. However, the multi-shock and nearly isentropic compression did not initiate any reactions in the explosive. The study considered the pressure-based models Ignition and Growth [41], WSD [79], and WSD extended for desensitization [80] as well as the entropy based model CREST [3]. Results confirmed that pressure-based models predict detonation in all cases where pressure rises above a threshold regardless of the process that has led to this increase, whereas the entropy-based model produced the best match to the experimental results.

Tarver [24] has presented numerical results from the I&G for the hockey puck configuration where dead zones were experimentally observed. The simulations show good agreement with the breakout times of the diffracted detonation and even report the formation of dead zones. However, subsequent investigation by Kapila et al. [23] showed that the dead zones are not sustained and in fact they are quickly consumed as the detonation expands around the corner. These results further reinforce the notion that pressure dependence makes the reaction models too reactive in situations where shock desensitization occurs.

While the original pressure-based reactive models have been unsuccessful in capturing desensitization, there has been a large number of enhancements aimed to replicate desensitization effects with pressure-based reaction rates. Initial efforts used switches to deactivate reaction if a critical range of shock compression is generated in the explosive [81]. However, these cannot replicate the time dependence observed in detonation quenching experiments. A more sophisticated approach was proposed by DeOliveira et al. [14] which suggested the addition of a desensitization parameter that is advected with the flow coupled with a desensitization rate similar to the reaction rate. This modification has managed to match experimental results for detonation quenching [75] and corner turning [82] in TATB-based explosives.

Despite the success of the desensitization models for pressure-based reaction models, their introduction requires a desensitization rate formulation and an adjustment of the reaction rate for which not much is known. In addition, the introduction of new parameters requires calibration for each explosive and it is possible that different

5.3. Mathematical model of desensitization

applications will require different parameters, similar to the need for different initiation and propagation parameters for I&G. For example, the parameters by DeOliveira were reported by Tarver [25] to produce heavier desensitization in the case of the Jack Rabbit experiments whereas Vandersall et al. [75] had to slightly increase desensitization to better match the experimental data for the same explosive.

The use of a desensitization model to reproduce the effects of desensitization follows from the classical view that desensitization is caused by the activation of the available hotspots in the explosive. However, reaction rates dependant on entropy or temperature have been shown to account for desensitization naturally. In particular, the entropy-based reaction model CREST has been shown to agree with experimental corner turning data at different initial temperatures [83] using one set of coefficients. This has given rise to an alternative theory for the cause of desensitization, as discussed in the previous section.

In essence, the different methods of modelling desensitization emerge from the two views on the cause of desensitization. The question of which is the most appropriate method will be addressed by the outcome of the debate between the two hypotheses. Further investigations are required to provide conclusive arguments.

5.3.1 The desensitization model by DeOliveira et al. [14]

The Ignition and Growth reactive model has been quite successful in modelling detonation and a large range of explosives have been calibrated for this reactive model. However, its dependence on local pressure makes it unable to capture desensitization effects. A proposed desensitization model [14] has showed promising results in capturing dead zone formation. This will allow the use of the extensive I&G parameter sets to applications involving desensitization phenomena.

The proposed desensitization model is based on the concept that two competing transformations are taking place when an explosive charge is shocked [77]. One is the chemical transformation which turns reactants into products with the release of energy and the second is a mechanical transformation that activates the hotspots and progressively makes the explosive less sensitive. In this view, reactions and desensitization behave similarly which warrants similar treatment. The desensitization model introduces a desensitization parameter $\psi \in [0, 1]$ that is advected in the flow

$$\frac{\partial \psi}{\partial t} + \mathbf{u} \nabla \psi = \mathcal{C}, \quad (5.1)$$

5.3. Mathematical model of desensitization

where $\psi = 0$ represents the pristine explosive and $\psi = 1$ represents the completely desensitized state. The inclusion of this variable in the hybrid model (chapter 2), is done by combining it with the continuity equation for the reactive material, similar to the reaction progress variable which yields

$$\frac{\partial z\rho_1\psi}{\partial t} + \nabla \cdot z\rho_1\psi\mathbf{u} = z\rho_1\mathcal{C}. \quad (5.2)$$

This introduces a desensitization rate \mathcal{C} for which DeOliveira et al. proposes the form

$$\mathcal{C} = Ap(1 - \psi)(\psi + \varepsilon), \quad (5.3)$$

where p is local pressure, A is a constant representing the strength of the desensitization and ε is a small number required for the desensitization rate to produce non-trivial solutions at $\psi = 0$. The form of the desensitization rate is parabolic concave down which means that it is minimum at the least and most desensitized states and has a maximum at the midpoint of $\psi = 0.5$. There is no physical justification behind this choice. In fact the rate being lowest at the beginning is counter-intuitive when considering that the closure of pores is assumed to be the strongest cause of desensitization. Compression of a porous material requires the least energy at the beginning and progressively becomes harder as it is compacted. Thus the desensitization rate should have a maximum during the initial compression and decrease as desensitization increases.

Further, the linear dependence on pressure is contrary to experimental studies. Campbell and Travis [74] and later Mulford et al. [84] found that pressure p and time to desensitization τ are related by an expression of the form

$$p^m\tau = c \quad (5.4)$$

where m and c are constants. The exponent was found to be $m = 2.2$ for HMX-based PBX9404 which suggests that the addition of an exponent on the pressure dependence will allow it to calibrate to experimental data more accurately.

The parabolic form of the desensitization rate has proven useful in the numerical modelling of desensitization despite having no physical justification. In its suggested form, the desensitization rate does not depend on the reaction progress variable and the desensitization proceeds independently of whether the reactant is being consumed or not. The minimal desensitization rate when the material is pristine, allows for the reactions to be initiated undisturbed if the stimulus is above the initiation threshold. This ensures that the desensitization model does not alter the standard I&G detonation

5.3. Mathematical model of desensitization

initiation and propagation characteristics in regimes where the desensitization does not have an effect. For prompt initiation, the reaction progress variable λ should increase faster than the desensitization variable ψ . If, instead, the desensitization variable grows faster than the reaction variable, it will hinder further growth of the reaction and either fail to initiate or quench the detonation.

Another numerical advantage of the parabolic form is that the differential equation can be solved analytically which would allow for its quick and accurate numerical update without the need for numerical solution algorithms. The differential equation

$$\frac{dy}{d\tau} = Ap(1-y)(y+\varepsilon) \rightarrow \int_{\psi_0}^{\psi} \frac{dy}{(1-y)(y+\varepsilon)} = \int_0^t Apd\tau, \quad (5.5)$$

yields

$$\psi(t) = \frac{\exp(Apt(1+\varepsilon)) + \varepsilon \frac{\psi_0-1}{\psi_0+\varepsilon}}{\exp(Apt(1+\varepsilon)) - \frac{\psi_0-1}{\psi_0+\varepsilon}}, \quad (5.6)$$

which is used to update the desensitization variable at each time step.

The desensitization model also modifies the reaction rate so that it also depends on the desensitization parameter. The modifications by DeOliveira et al. [14] aim to increase the ignition threshold and inhibit the growth terms. This is achieved by replacing the constant α in the I&G rate with the function

$$\alpha(\psi) = \alpha_0(1-\psi) + \alpha_1\psi, \quad (5.7)$$

where α_0 is the original threshold and α_1 is a newly introduced constant that represents the ignition threshold of the completely desensitized explosive. In addition, the lower limit of the growth term is increased by the introduction of a minimum value of reaction progress before it is activated. This term is set to

$$\lambda_{G1}^{\min} = \lambda_c\psi, \quad (5.8)$$

where λ_c a constant. Even though the original study suggests this restriction only for the first growth term, since the second already has a usually high λ_{G2}^{\min} threshold, our implementation sets the lower threshold for the second growth term to be the maximum between the original I&G parameter and the value of equation (5.8) to ensure that no growth terms are activated below the desensitized threshold regardless of the original I&G parameters.

Overall, the desensitization model introduces four new parameters. Two relating to

the desensitization rate and the two for the inhibition of the reaction rate. The rate parameters can be found using data of time to desensitization over input pressure for which experiments have been performed for a few explosives. The calibration usually concerns parameter A since ε is only required to be a small number. However, as previously mentioned, experiments suggest that the desensitization time and pressure are related with an exponent which can be added to the desensitization rate for a more faithful representation of the experimental data as suggested by Hussain et al. [72]. The parameters for the adjustment of the reaction rate are more arbitrarily deduced. Experiments investigating the increase in the threshold of initiation for completely desensitized explosive can be used to determine parameter α_1 while the restriction of the growth terms is chosen so that experiments involving formation of dead zones are matched.

5.4 Validation

The study of desensitization and formation of dead zones usually involves the diffraction of a detonation wave at a sharp edge, known as corner turning experiments. The desensitization model implemented for this study is validated through a series of test cases involving this geometry starting with the hockey puck geometry which was used in the study introducing the desensitization model. Two variations of the material of the corner are considered. One has rigid walls, as in the original work of DeOliveira et al. [14] and the second has steel, modelled as an elastic-plastic material. Lastly, the implementation is assessed in the case of the Jack Rabbit experiments which provide a much more challenging configuration and for which there is useful experimental data.

The numerical computations involving the desensitization model require the use of appropriate resolution to exhibit the intended phenomenology of the model. This is inherited from the original I&G reaction model which also requires finely resolved simulations to capture the phenomenology that is designed into the equations. Thus, this validation section also aims to explore the resolution required to adequately capture the reaction and desensitization processes.

5.4.1 Detonation diffraction around a rigid corner

The hockey puck configuration considered here is shown in figure 5.1. It follows the experiment by Souers et al. [85] which used a cylindrical LX-17 explosive charge with a coaxial cylindrical cavity of $R = 19.05$ mm in radius and $L = 15$ mm in length. The

5.4. Validation

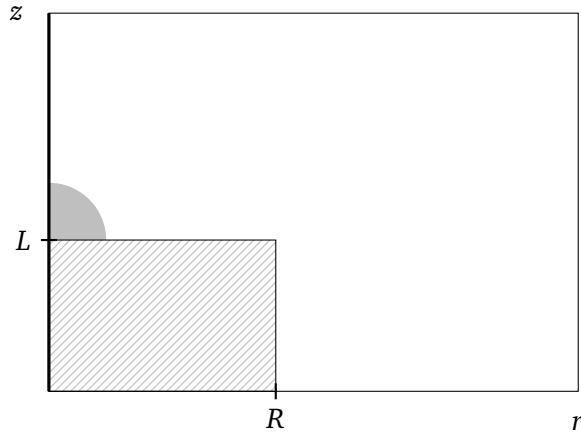


Figure 5.1: A two-dimensional illustration of the axisymmetric hockey puck configuration. It involves a cylindrical disk of radius R and height L which is surrounded by explosive. The detonation is initiated by a hemispherical region of high pressure positioned in the middle of disk's top surface.

LX-17 is initiated by a hemispherical TATB charge embedded within the LX17 at the base of the cavity. The experimental study used streak cameras to record breakout times along the side and base of the charge as well as x-ray photography to examine the detonation front. Results showcased the formation of dead zones in LX-17.

Figure 5.2 shows numerical results for the hockey puck configuration using rigid walls, as done in the study by DeOliveira. The setup is axisymmetric and the explosive is initiated by a hemispherical region of 7.68 mm in radius filled with products at the pressure of 31.46 GPa and positioned at the base of the cavity. This setup causes the formation of a hemispherical detonation that is well established when it reaches the corner at $t = 1.6 \mu\text{s}$ as seen in the first plot of figure 5.2.

Subsequently, the detonation is diffracted and while it continues to propagate undisturbed in the region above the corner, it is weakened as it expands around the corner. The reactions stop and a curved inert shock emanates from the corner which compresses and desensitizes the explosive as can be seen in the second frame. As the detonation continues to propagate radially outwards it expands and approaches the corner. Since it travels faster than the inert shock, it manages to go around the desensitized region and eventually touch the corner. This forms a region in the explosive where no reactions have taken place. Even the stronger shock reflected once the detonation hits the wall is not sufficient to overcome the increased reaction threshold and the resulting dead zone persists as seen in the last plot of figure 5.2.

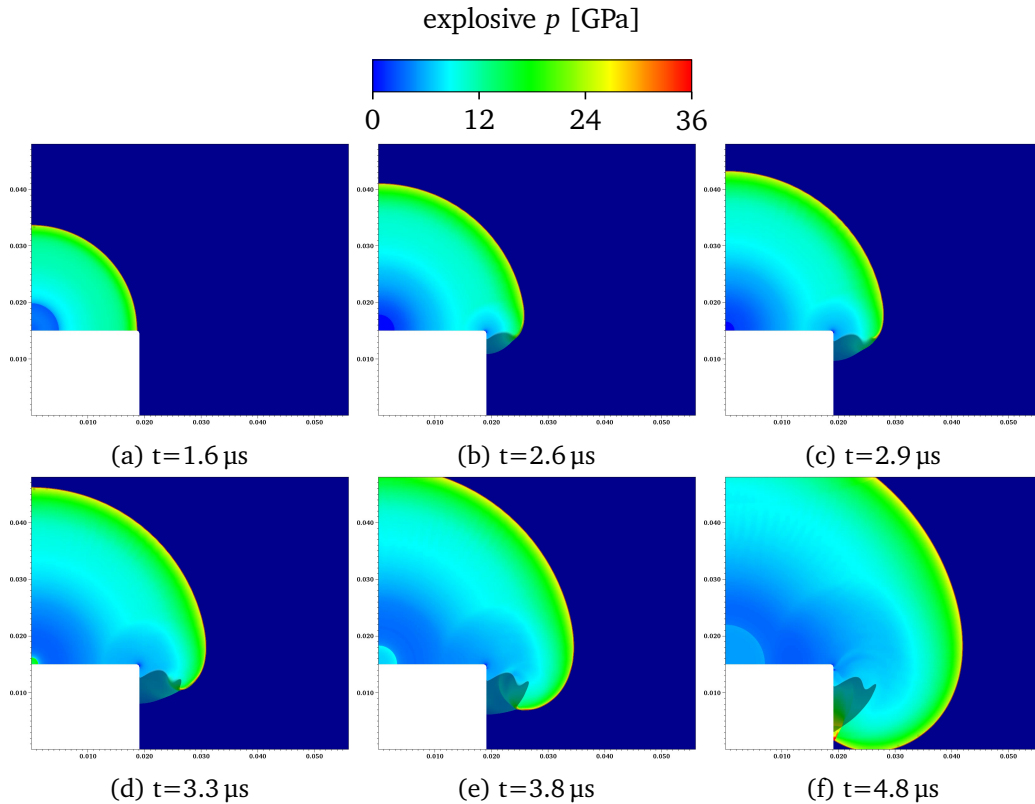


Figure 5.2: Plots of pressure from the numerical solution for the hockey puck configuration used in the experimental study by Souers et al. [85]. The shaded region represents areas where the explosive has not reacted (dead zone) and the resolution is $\Delta x = 10 \mu\text{m}$. The weak lateral shock produced after the detonation reaches the corner leads to the desensitization of the explosive and the formation of a dead zone.

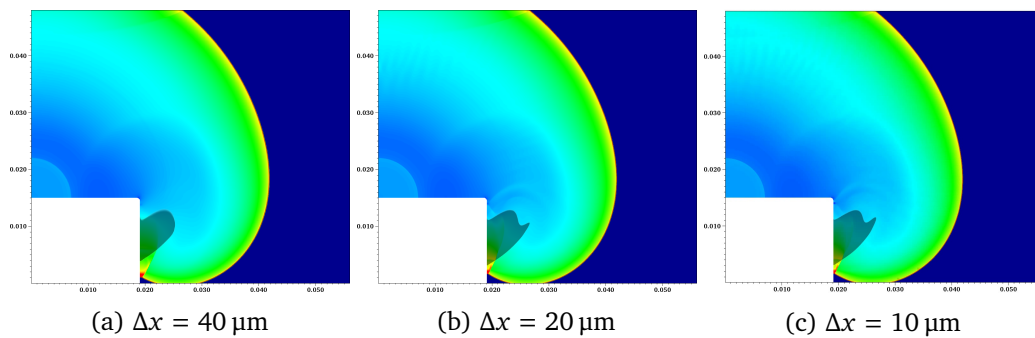


Figure 5.3: Increasing resolution plots for the numerical solution of the hockey puck configuration at time $4.8 \mu\text{s}$. The resulting dead zone is not adequately captured with resolutions of $40 \mu\text{m}$ or more. The solution shows adequate convergence for cell size of $20 \mu\text{m}$.

5.4. Validation

The computational mesh used in this validation case had a cell size of $160\ \mu\text{m}$ and was adaptively refined using two levels of refinement by a factor of four each resulting in an effective resolution of $10\ \mu\text{m}$ and was selected based on a convergence study. Figure 5.3 shows the resulting pressure field and dead zone for increasing resolution. The shape of the dead-zone requires at least $20\ \mu\text{m}$ to converge while the position and shape of the detonation front has sufficiently converged even for the $40\ \mu\text{m}$ resolution. It should be noted that for resolutions of $80\ \mu\text{m}$ or lower, the explosive is immediately desensitized, before the hemispherical detonation is established. This reinforces the notion that the effect of the desensitization model requires significant resolution to manifest and even more resolution to ensure convergence. The results presented in this section can be directly compared to the example used in the study by DeOliveira et al. [14]. The results are very similar which validates the implementation used in the study.

5.4.2 Detonation diffraction around a solid corner

We consider the same configuration as used in the previous section but with a solid material replacing the rigid corner. The material is steel and is governed by the elastic-plastic formulation along with the hyperelastic EOS and parameters given in the study of Barton and Drikakis [16] and the perfect plasticity model of constant yield stress [17]. The addition of a high sound speed and high impedance material in the corner means that the shock wave formed in the confining material will be fast enough to reach the explosive in the region shadowed by the corner ahead of the weak lateral shock resulting from the diffraction of the detonation. This has the potential to desensitize a larger portion of the explosive and produce a larger dead zone.

The explosive is initiated by a hemispherical region of high pressure products as in the previous section. Figure 5.4 plots the numerical solution of the detonation diffracting around the solid corner at selected times. Initially, the propagation of the detonation along the steel disk generates a shock wave in the solid. This shock propagates within the solid to reach the vertical side of the corner and transmit a shock in the explosive. This is in addition to the lateral shock formed by the diffraction of the detonation. These two shock waves are not strong enough to induce reactions in the explosive and they jointly desensitize the explosive.

In subsequent times, the detonation expands and propagates round the corner. It does not penetrate the desensitized region where it is quenched and degenerates into an inert shock wave. Plot 5.4e illustrates the complex wave structures formed after the

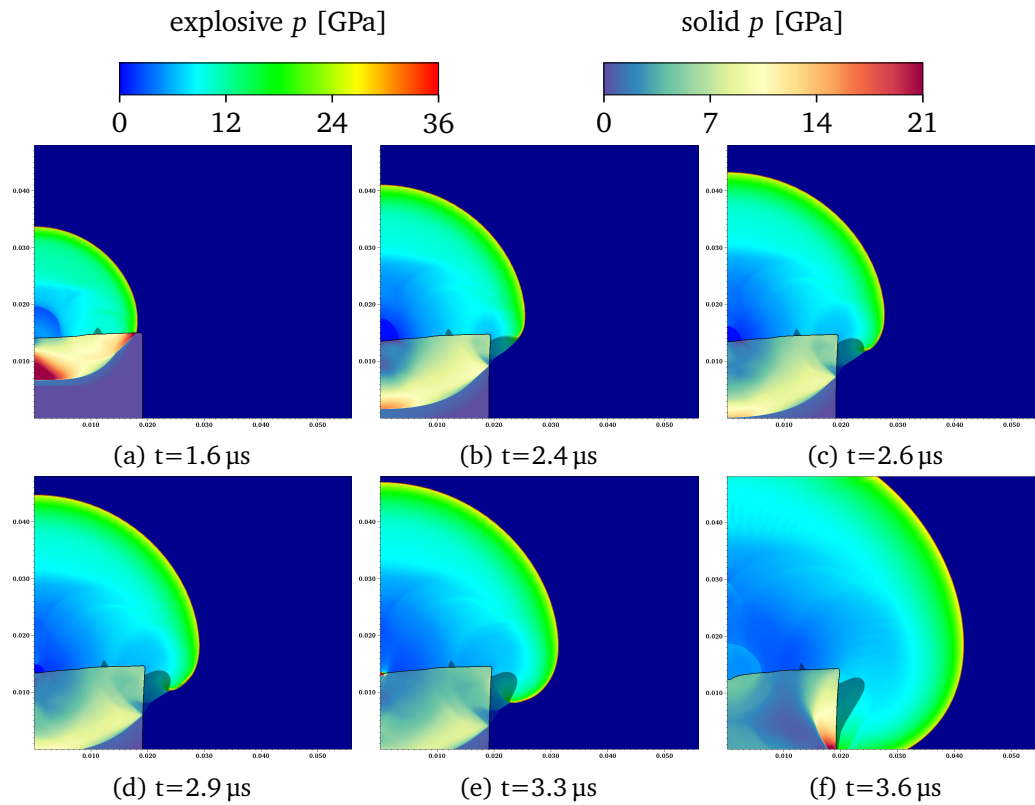


Figure 5.4: Plots of the pressure field from the numerical solution of the hockey puck configuration with a solid corner. The shaded region represents non-reacted regions of the explosive and the resolution is $\Delta x = 10 \mu\text{m}$. The shock wave formed in the solid material is transmitted into the explosive along the vertical side of the corner. This desensitizes the explosive region and leads to the formation of a dead-zone.

5.4. Validation

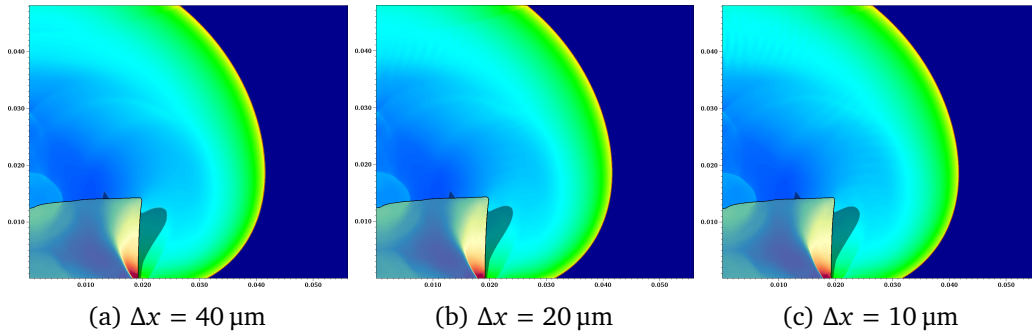


Figure 5.5: Increasing resolution plots for the numerical solution of the hockey puck configuration with a solid corner. The solution has sufficiently converged even for the resolution of $40 \mu\text{m}$.

diffraction of the detonation. The shock wave transmitted from the solid produces an oblique shock in the explosive that has propagated farthest from the corner. Upstream of it, the curved inert shock generated at the corner follows and forms a Mach stem as it interacts with the oblique shock. The pressures generated in these regions have not exceeded the initiation threshold and no reactions have occurred. However, the region is completely desensitized and the expanding detonation upstream is quenched as it encounters this region. The locus of interaction between the Mach stem formed by the two inert shock waves and the detonation is approximately the boundary of the formed dead zone.

The configurations of rigid and solid corner show differences in both the diffraction of detonation and the formed dead-zone. Initially, the detonation reaches the corner at similar times with the detonation in the solid corner slightly behind because of the loss of a fraction of energy in deforming the solid. However, the detonation around the solid corner expands faster than around the rigid corner because the solid corner has become slightly rounded by the passage of the detonation. Already at $2.6 \mu\text{s}$ after initiation, the detonation in the solid corner configuration has acquired significant curvature while in the rigid case, detonation has not been established below the height of the corner. Consequently the dead zone formed next to the solid corner is smaller than in the case of the rigid corner. However, the dead zone next to the solid corner is longer in height due to desensitization by the oblique shock wave transmitted from within the solid. Overall, the deformation of the solid corner leads to a weaker diffraction of the detonation wave and the formation of a smaller dead zone.

A convergence study was performed for the configuration of the solid corner and can be seen in figure 5.5. The numerical solution of this configuration seems to have

adequately converged for a resolution of 40 μm even in terms of the shape of the dead zone. This indicates that the resolution required for convergence depends on the shape complexity of the dead zone. As this can not be determined a priori, appropriate resolution studies are required for each application.

5.4.3 The Jack Rabbit experiments

The desensitization model is further validated against the so-called “Jack Rabbit” experiments performed at the LLNL[86]. These are a series of five experiments (PT3-7) with a complex setup that have been specifically designed to assess mathematical models of detonation in terms of detonation diffraction and desensitization. Several studies has considered the numerical simulation of these experiments using the most popular reactive models, including the one used in this study [25] as well as CREST [83] and more recently WSD(T) [87]. These studies have shown reasonable agreement with the experiment but neither has a complete match. In addition, the discrepancies vary to different degrees for each configuration. It is overall accepted that the numerical results are very sensitive to EOS and reaction rate parameters and that careful calibration is required for a more accurate match.

The configuration of this experiment can be seen in figure 5.6. The detonation is initiated at the centre of the uTATB charge and develops a hemispherical detonation front that is transferred to the LX17 charge. The existence of the steel plate forces the detonation to diffract around it while a shock propagates through the steel plate and into the explosive region between the two plates. The shock is designed to be weak enough to desensitizes the explosive in that region. When the detonation reaches the desensitized explosive it is quenched which leaves a non-reacted portion of explosive. The experimental setup used photon Doppler velocimetry (PDV) to measure the axial velocity along the lower aluminium plate in addition to x-ray photography.

The numerical simulation of the complex processes involved in the Jack Rabbit experiments requires that the setup and the material parameters used are a faithful representation of the actual configuration. Thus, both of the explosives were modelled as a two phase reactive material using the hybrid multiphase model without an inert phase. The parameter sets for the explosives ultra-fine TATB and LX-17 were taken from the study of Tarver[24] and the desensitization parameters from DeOliveira et al. [14]. The solid disks were modelled with the elastic-plastic formulation as mentioned previously.

Figure 5.7 shows the numerical solution at selected times for the PT5 configuration.

5.4. Validation

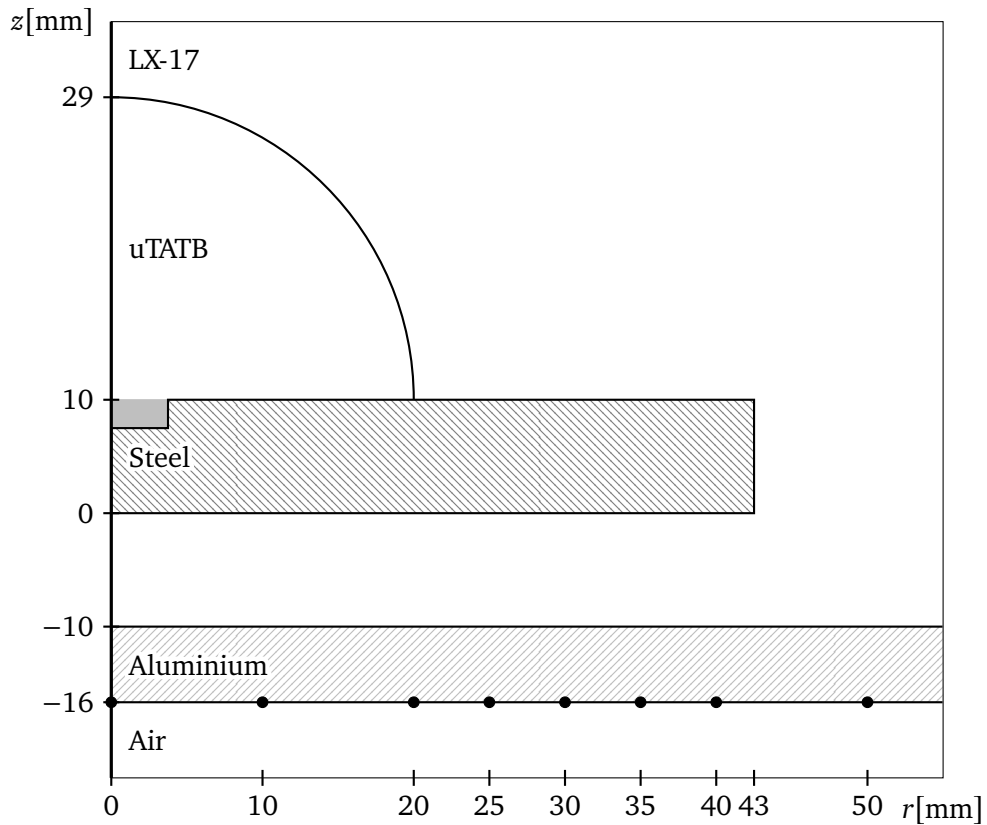


Figure 5.6: Illustration of the axisymmetric configuration used in the Jack Rabbit experiments. It involves a hemispherical ultra-fine TATB charge placed on top of a steel disk. These are embedded in a cylindrical LX-17 charge with aluminium plates at its bases. The uTATB is initiated by a detonator housed in the steel plate which is represented in the simulations by a high pressure region (grey area). The setup is designed to produce a weak shock in the region between the steel and aluminium plates which will desensitize the explosive there, before the detonation is diffracted around the steel disk and into that region. The points on the outer surface of the aluminium disk indicate the positions where the speed of the plate is measured. The distances correspond to the E5 variation (other versions have different values but same setup).

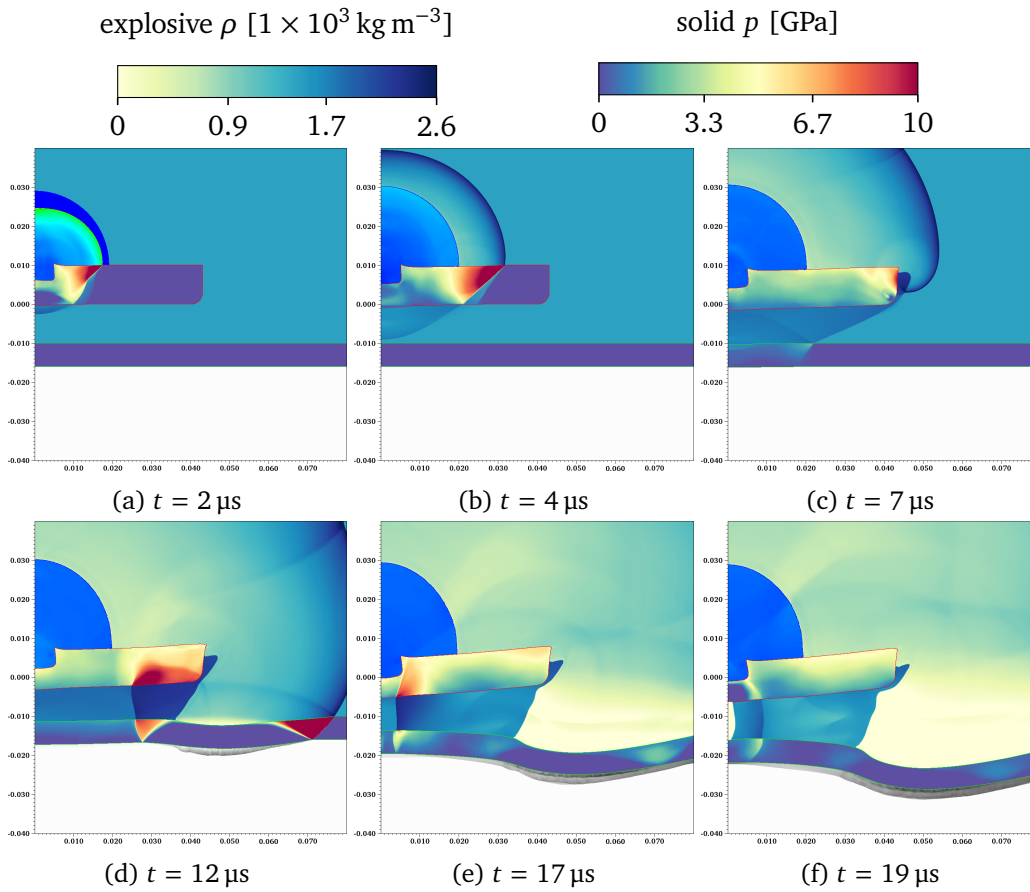


Figure 5.7: Plots of density from the numerical solution of experiment PT5 of the Jack Rabbit experiments [86]. As the spherical detonation propagates along the steel disk, an inert shock is transmitted into the explosive on the other side of the disk. This desensitizes a large region of the explosive which remains non-reacted as was seen in the experiment.

5.4. Validation

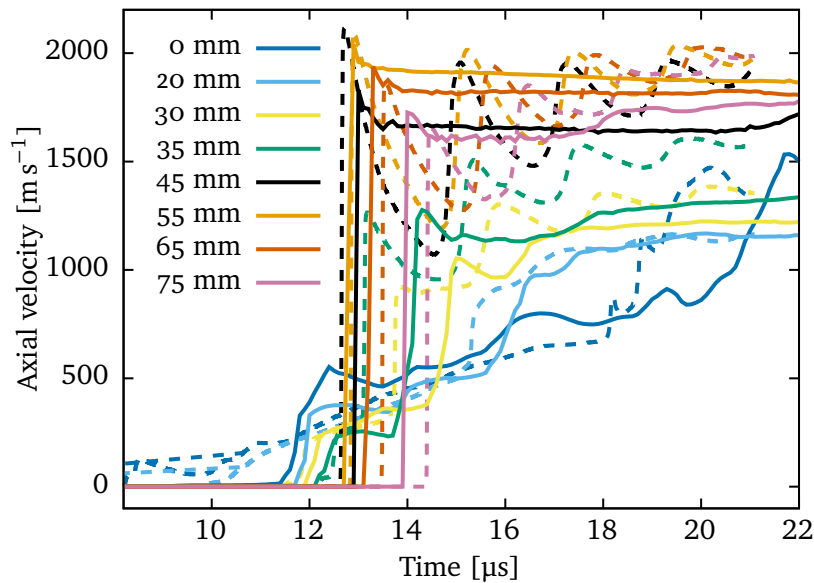


Figure 5.8: Comparison of experimental (solid lines) and numerical results (dashed lines) for the Jack Rabbit experiment PT5. The plot shows axial velocity measured at given radial distances from the centre of the aluminium plate.

The detonation in the hemispherical charge was initiated by a small region of high pressure uTATB products. This was embedded in the steel disk as was the detonator used in the actual setup. The first plot shows the detonation wave establishing in the ultra-fine TATB. It is then transmitted into the LX-17 and propagates along the steel disk. At the same time, a shock has formed in the steel plate which propagates through the material and is transmitted into the lower explosive region, between the two disks. It does not induce any reactions in the explosive but completely desensitizes a large region of the explosive between the two disks.

Once the detonation has reached the corner, it is diffracted and a weak shock forms which desensitizes a small pocket of explosive similar to the cases discussed in the two previous sections. This is in addition to the larger region of desensitized explosive between the metal disks. As the detonation turns around the steel plate and moves into the desensitized region, the reactions stop and it is reduced to an inert shock propagating in the reactant. The inert shock wave moves towards the axis of symmetry of the configuration while a detonation propagates radially outwards into the undisturbed explosive. This is evident by the curved shape of the lower aluminium plate caused by being pushed with different force depending on whether the detonation or the inert shock is propagating along it. The point where there is a change in the

curvature of the aluminium disk indicates the approximate radial extent of the dead zone. Meanwhile, the inert shock propagating in the desensitized region is focused on the axis of the configuration which strengthens it and initiates reactions in that region. However, it is promptly extinguished as it begins to propagate outwards and degenerates into an inert shock once again as seen in the last plot of figure 5.7.

The comparison between the numerical and experimental axial velocity values and resulting dead zone for the PT5 experiment is shown in figures 5.8 and 5.10. Our results show good agreement with the experiment in terms of peak axial speeds and resulting dead zone. The detonation first impacts the aluminium plate somewhere between the 45 mm – 55 mm as in the experiment. In terms of jump off times, best agreement is seen for positions ahead of the point of first impact, in which the detonation propagates. However, the numerical solution shows a slightly slower propagation of the detonation as indicated by the increasing discrepancy in larger radial distances. This fact, in conjunction with the somewhat bigger dead zone of the numerical solution indicate that the desensitization parameters should be adjusted to produce less desensitization, as is also mentioned by Tarver [25]. In the region where the inert shock propagates (inside the point of first impact), the numerical solution predicts a faster travelling shock wave than seen in the experiment. This indicates that a calibration of the reactants EOS is required for a more accurate prediction. It should also be noted that the ignition seen at the region near the axis of the plate caused a rapid increase of the velocity at the centre of the plate which is also seen in the experimental results.

Similar results are seen for the case of the PT6 experiment which are compared with the experimental values in figure 5.9. This configuration has twice the distance between the steel and aluminium disk compared to the PT5 experiment but the same radius for the steel disk. This means that the point of first impact of the detonation on the aluminium plate is similar to before. However, the detonation manages to propagate further inwards in this configuration since the inert shock did not have the time to cover the whole region between the metal disks. A discrepancy with the experimental values is seen in later times where the ignition of some explosive as the shock wave is focused on the axis of the setup causes a large increase in the axial speed which greatly exceeds the experimental value.

A final distinction between the numerical and experimental results is seen in the speed of the aluminium plate after the initial peaks. The experimental data show constant velocity for the plate whereas the numerical results predict oscillating values. The oscillations of the numerical simulation are considered physical and are caused by the consecutive reflections of the shock wave inside the aluminium plate. The lack

5.4. Validation

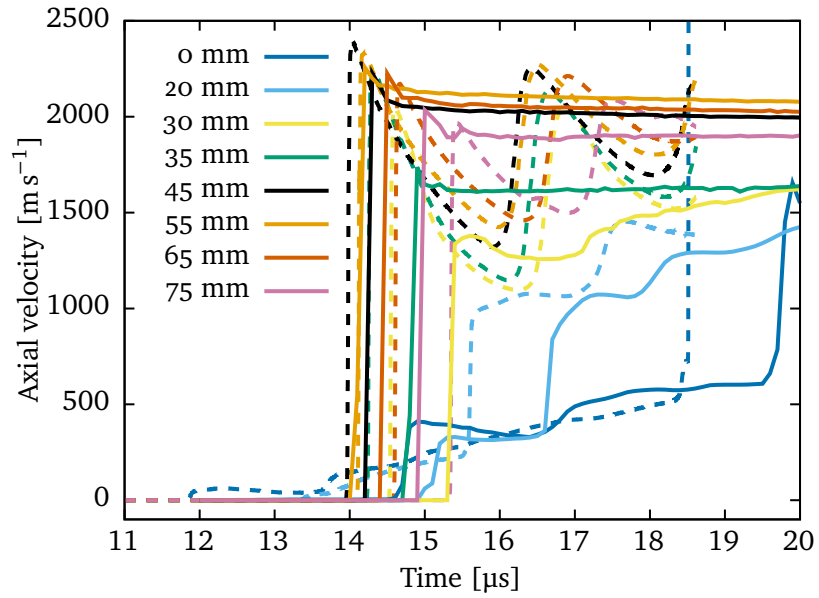


Figure 5.9: Comparison of experimental (solid lines) and numerical results (dashed lines) for the Jack Rabbit experiment PT6 similar to figure 5.8

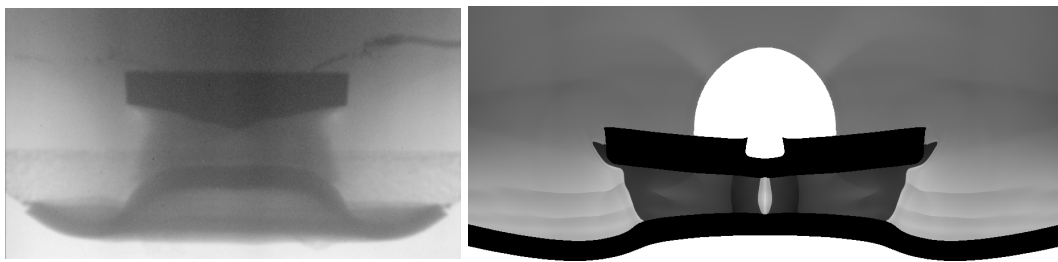
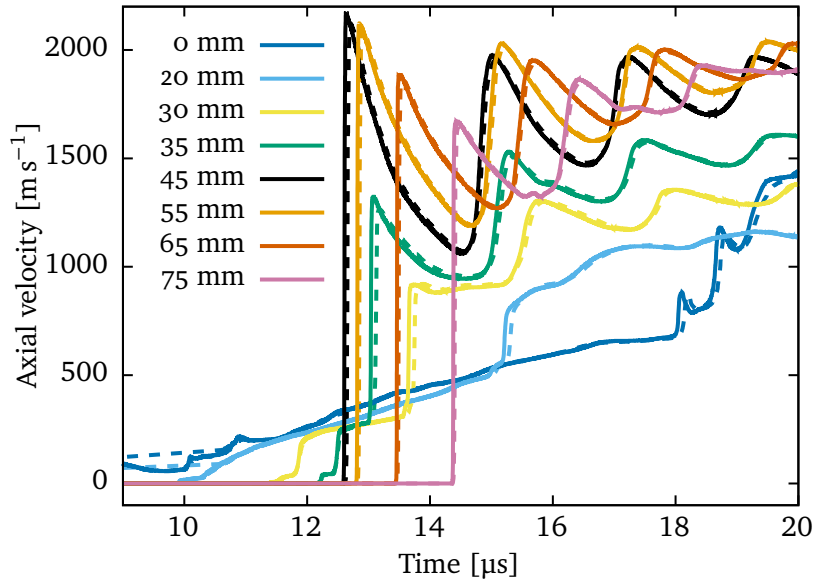


Figure 5.10: Comparison of dead zone formed in experimental (left) and numerical results (right) for the Jack Rabbit experiment PT5.



(a) The numerical axial velocities obtained with a resolution of $\Delta x = 20 \mu\text{m}$ (solid lines) and of $\Delta x = 40 \mu\text{m}$ (dashed lines).

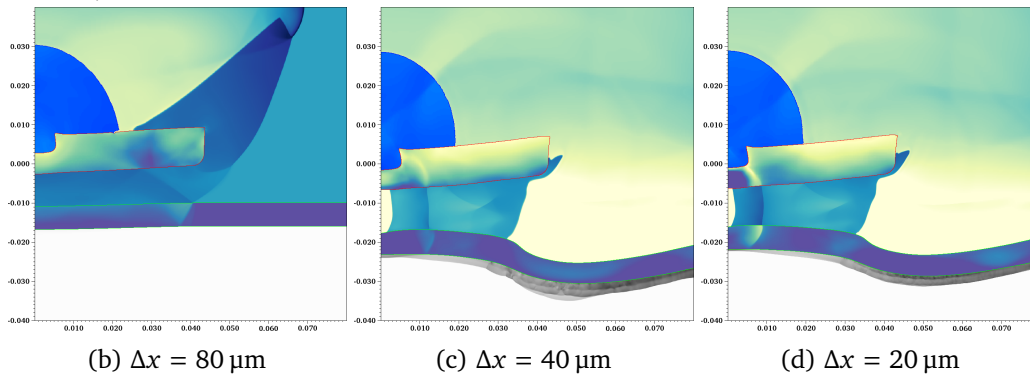


Figure 5.11: Plots of increasing resolution for the numerical solution of the PT5 Jack Rabbit experiment.

5.4. Validation

of oscillations in the case of the experiments is probably caused by spallation. As the plate is bent, fragments break off and interfere with the velocimeter which registers the constant velocity of the fragments instead of the plate velocity.

A convergence study for this configuration can be seen in figure 5.11. This shows that the solution has converged for the resolution of $\Delta x = 40 \mu\text{m}$ both in terms of the resulting dead-zone and of the axial velocities. As seen for previous configurations as well, the effect of desensitization is not properly captured for the resolution of $\Delta x = 80 \mu\text{m}$ where the detonation is quenched before it turns the corner. This contradicts the study by Tarver [25] which used a resolution of $\Delta x = 100 \mu\text{m}$ to perform the same study.

5.4.4 Desensitization model parameters for composition B

The most common explosive used in mining boosters has been composition B (RDX,TNT) which is progressively being replaced by pentolite (PETN,TNT). For both of these explosives there exist validated parameter sets for the regular Ignition and Growth reactive model. However, the desensitization model of DeOliveira et al. [14] has only been used for the TATB-based explosive LX-17 and no parameters exist for either of these explosives. Fortunately, one of the original studies on shock desensitization had used composition B [74] and includes the necessary experimental data to determine the parameters for the desensitization model. Furthermore, dead zone formation in composition B has been observed experimentally which allows for the validation of the selected parameters. For these reasons the study of the booster configuration considers composition B as the booster explosive instead of pentolite.

The desensitization rate requires two parameters, A and ε . These were determined based on the experimental data on desensitization time over shock pressure taken from the study of composition B-3 (60/40 RDX/TNT) of initial density 1.737 g cm^{-3} [74]. The study provides just two data points but the form of the desensitization rate does not allow for both to be satisfied as discussed in section 5.3.1. Parameter ε is only required to be a small number so $\varepsilon = 10^{-3}$ is chosen as in the original study. Parameter A is chosen so that it is equally close to both experimental data points. This yields a value of $A = 3.5 \times 10^{-3} \text{ Pa}^{-1} \text{ s}^{-1}$.

The parameters for equation of states and reaction rate for composition B are taken from the study of Urtiew et al. [88] which considered a 63/36/1 RDX/TNT/wax variant of composition B with initial density 1.717 g cm^{-3} . The density threshold for initiation was set so that it can be ignited by shock waves of 0.5 GPa or stronger. This does not

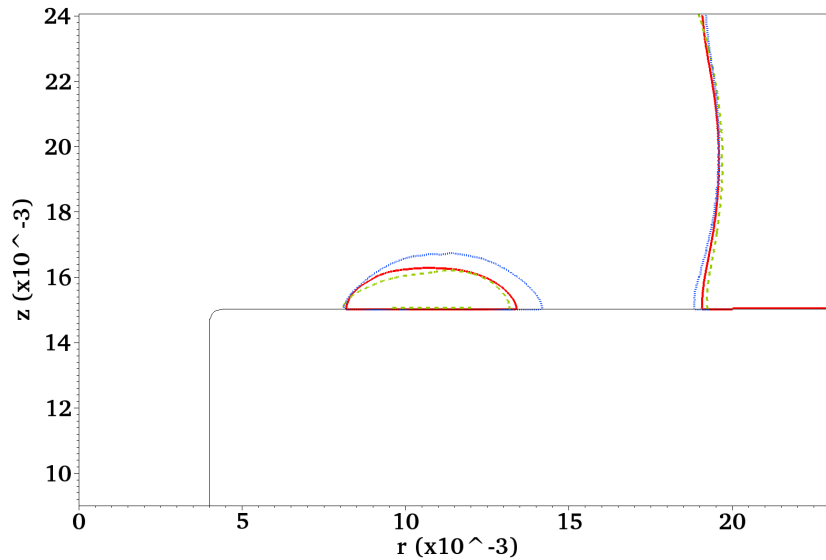


Figure 5.12: Contour plot of reactants mass fraction variable at $\lambda = 0.5$ which depicts the dead zone formed in composition B once the detonation diffracts into the wider cylindrical charge. Three solutions of increasing resolution are shown, starting with the $\Delta x = 40 \mu\text{m}$ (blue dotted line), $\Delta x = 20 \mu\text{m}$ (green dashed line) and $\Delta x = 10 \mu\text{m}$ (red solid line).

agree with the study of Campbell and Travis [74] in which shock waves up to 2.4 GPa did not ignite the explosive. The discrepancy is attributed to the different composition B variant used for each study. To ensure that the desensitization behaviour is replicated, the density threshold of the pristine explosive was raised to $\alpha_0 = 0.1$ so that shock waves of approximately 2 GPa do not ignite it.

The next two parameters required for the desensitization model correspond to the change of the reaction rate when the explosive is desensitized. These are α_1 which represents the increased density threshold for initiation and λ_c which restricts the growth terms until some reactions have occurred. There is no proper method for determining these parameters and following the example of DeOliveira, they are chosen so that they reproduce dead zones in configurations that have been experimentally observed to produce them.

The experimental study on dead zone formation in composition B was performed by Held [76]. The author used a semi-cylindrical charge of a variation of the composition B explosive that had RDX/TNT ratio of 65/35 and an average density of 1.72 g cm^{-3} . The charge had a radius of 29 mm and was initiated by a cylindrical charge of 95/5

5.5. *The booster configuration*

RDX/wax and a radius of 4 mm. The detonation from the small charge passed into the semi-cylindrical charge where it was diffracted and was recorded using a streak mask positioned on the flat surface of the semi-cylindrical charge. The results confirmed the formation of a dead zone and measured a corner turning distance somewhere between 8 mm – 10 mm.

The parameter values $\alpha_1 = 0.5$ and $\lambda_c = 0.2$ were found to reproduce the formation of a dead zone for the configuration used in the experimental study by Held [76]. The dead zone formed in the simulation is shown in figure 5.12 for solutions of increasing resolution. It should be noted that the configuration used in the simulation has a complete cylindrical charge instead of a semi-cylinder. This was chosen to allow for an axisymmetric two-dimensional domain. Thus, it is expected that the resulting dead zone will be smaller than in the experimental study due to additional release waves that weaken the detonation in a semi-cylindrical charge.

5.5 The booster configuration

The configuration considered here is inspired by the 400 g Global Booster produced by Orica. The actual booster is made of multiple parts and has a complex design to allow for the use of different types of detonators, detonator cord and even a sensitizing PETN bottle. The design adopted here is simpler and axisymmetric to allow for a solution in a two-dimensional domain and make high resolution simulations possible.

The booster is made out of an outer shell filled with the explosive and a cap on top. There is a cylindrical cavity along the axis for placing the detonator. The shell has a cylindrical shape of 25 mm in radius and 130 mm in length with a rounded lower corner of radius 20 mm and is made from a thermoplastic polymer of 1 mm in thickness. It is modelled as a fluid using the Euler equations and the shock Mie-Grüneisen EOS with parameters corresponding to PMMA from the work of Hamada et al. [89]. The high pressures that are imparted by detonation waves justify the assumption of purely fluid behaviour given the low yield strength of plastics.

The booster explosive is composition B which has been extensively used in mining boosters and for which there exist validated reactive parameter sets and extensive experimental studies. The parameter set was taken from the study of Urtiew et al. [88] and the desensitization model parameters were determined as described in section 5.4.4. The initial density of composition B is 1.717 g cm^{-3} and the volume of the booster is 233.36 cm^3 which translates to approximately 400 g as in the Global Booster produced by Orica.

5.5. The booster configuration

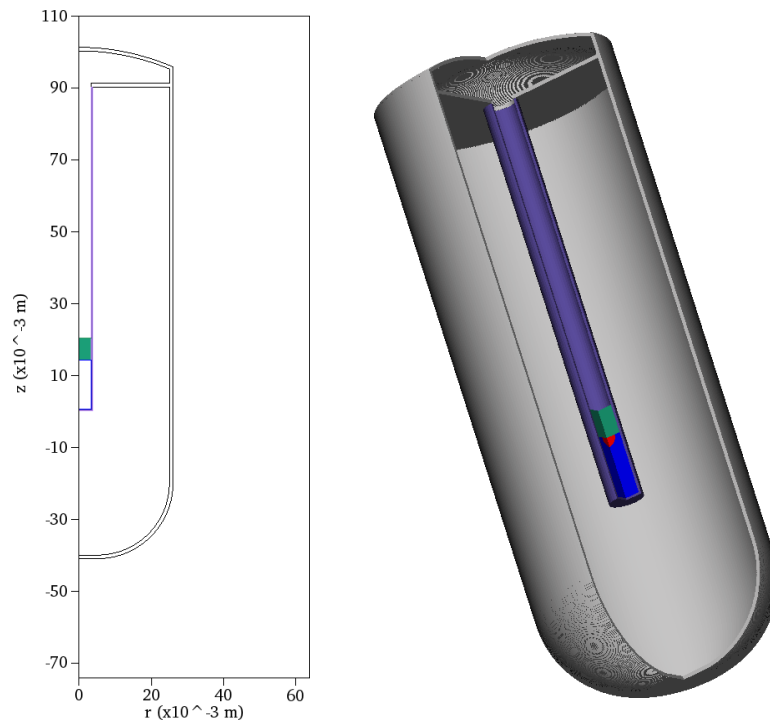


Figure 5.13: The booster and detonator configuration have an axisymmetric design which is based on actual devices used in the mining industry. The booster has a plastic shell (shown in grey) and is filled with approximately 400 g of composition B (not shown). The detonator is placed inside the booster charge and is made of a metal shell (shown in purple) and contains 780 mg of PETN.

5.6. *Initiation of the booster without desensitization*

The design of the detonator also follows the specifications of an industrial detonator and specifically of the i-kon II by Orica. This has a copper shell of 3.3 mm in radius and 89 mm in length with a thickness of 0.5 mm. It is filled with 780 mg of the explosive PETN which is placed at the base of detonator, deep inside the booster explosive. The PETN is modelled as a two phase explosive with the I&G reactive model and parameters from the study by Tarver et al. [56]. The explosive charge is sealed with a copper cup of 6.2 mm in length. The metal shell and cup of the detonator are both modelled with the elastic-plastic formulation as in the previous chapter.

The assembled configuration of booster and detonator is initiated by a small hemispherical region of high pressure PETN products as shown in figure 5.13 (with red). The expansion of the products leads to a prompt detonation of the PETN detonator charge which generates a shock in the detonator shell and subsequently in the explosive of the booster. The material surrounding the booster is water which emulates aquarium tests used for performance assessment of explosive devices. The water is modelled with the inviscid Euler equations and the stiffened gas EOS with parameters given in table 4.3. The numerical solution was computed with a resolution of 40 μm which was found adequate for the convergence of the detonation front and formed dead zones.

5.6 **Initiation of the booster without desensitization**

The study of the booster configuration begins by considering the initiation processes without accounting for desensitization effects and modelling the explosive with the regular pressure-based I&G reaction rate. This aims to investigate the already intricate processes involved in the initiation and propagation of a detonation in the booster and to allow for comparisons and evaluation of the impact of desensitization.

The initiation of a booster depends on several factors in addition to potential desensitization effects. Initially, the impulse generated by the detonator must lead to a run to detonation distance that is well inside the boundaries of the explosive. Also, the established detonation should have curvature that does not exceed the limits for a self-sustained detonation. This will determine the ability of the detonation to diffract and establish a self-propagating detonation upstream of the detonator. Lastly, as the detonation propagates in the explosive, additional waves are generated from the interaction with the material boundaries of the detonator and the booster shell. These waves disturb the flow behind the detonation and have the potential to interfere with the reaction zone and influence the propagation of detonation.

An ideal initiation of the booster will lead to the detonation of the entire explosive of

5.6. *Initiation of the booster without desensitization*

the booster and extract the maximum energy from the device. This will depend on the characteristics of the detonator and explosive in the booster but also on the geometry and size of the booster charge. The impact of desensitization effects on the initiation processes will likely be a delay in the run to detonation, slow detonation diffraction and most critically, the formation of regions of non-reacted explosive. However, the proper assessment of the impact of desensitization must first establish the characteristic features of the initiation process without the influence of desensitization effects, which is done in this section.

The booster configurations considered involve the regular detonator of 0.5 mm in thickness with either aluminium, copper or steel shell. The initiation of the booster with the aluminium detonator is shown in figure 5.14. The impulse produced by the detonator leads to the formation of an extensive detonation front mainly downstream of the detonator while a shock of approximately 1 GPa – 3 GPa (at 3 μ s) is transmitted from the sides of the detonator and propagates upstream without inducing reactions. The detonation quickly expands and increases its curvature. An upstream and downstream front have been established by the time it reaches the outer shell of the booster as seen in plot 5.14b. In subsequent times both fronts continue to propagate undisturbed until all of the explosive is consumed. A curved shock front is transmitted into the surrounding water which expands outwards and is supported by the expansion of the explosive products.

The booster with the copper detonator is shown in figure 5.15. In this setup, the detonation of the base charge in the detonator induces a weaker pulse in the explosive of the booster. This is caused by the larger impedance difference between the copper shell and composition B as was also observed in the study of the isolated detonators in section 4.6. The buildup to detonation is slower and the run to detonation distance is larger. Nevertheless, a detonation is established which progressively expands and attains enough curvature to propagate upstream before it reaches the boundary of the explosive. The detonation upstream propagates through a large region of previously shocked explosive. The shock strength is less than from the aluminium detonator and in the range of 1 GPa – 2 GPa. However, the detonation is not affected by desensitization effects since the pressure-based reactions are activated regardless of the state of the explosive ahead.

In both considered cases, the booster explosive was completely consumed. The copper detonator caused slower formation of the detonation but apart from a time delay, the pressure pulse generated in the surrounding water was similar. The results of this section have shown that the detonator and booster configuration do lead to

5.6. *Initiation of the booster without desensitization*

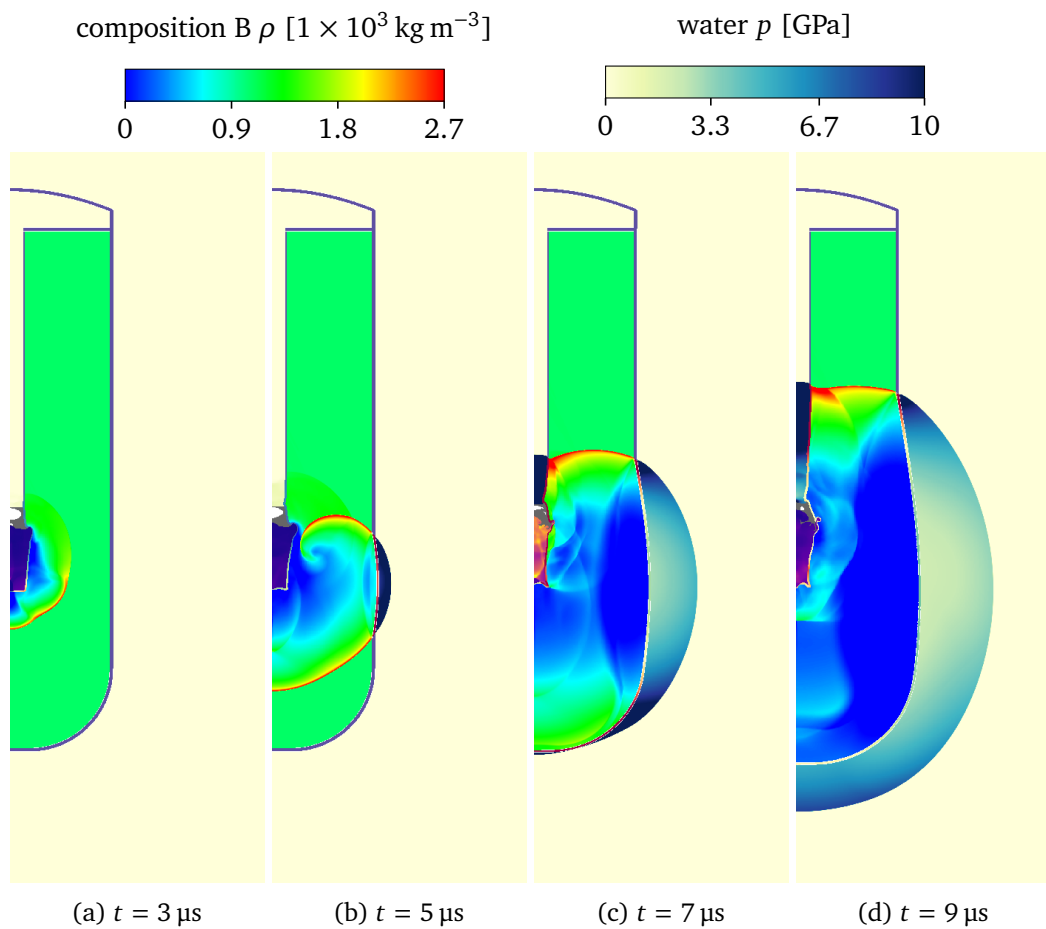


Figure 5.14: Plots of density depicting the initiation of the booster explosive from an aluminium detonator without accounting for desensitization. A detonation is promptly established and propagates through the entire charge.

5.7. The effect of detonator shell material

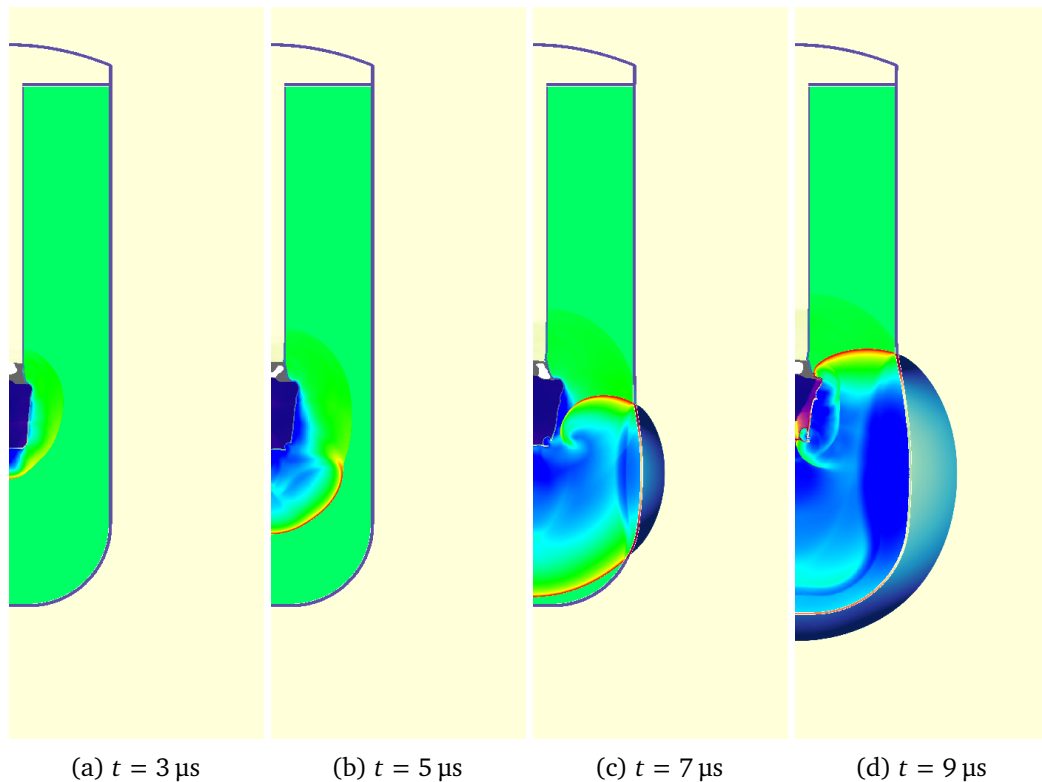


Figure 5.15: Plots of density depicting the initiation of the booster explosive from a copper detonator without accounting for desensitization. The detonation is established at a slower rate compared to the aluminium configuration but also manages to diffract upstream of the detonator and consume the entire booster charge.

successful initiation but have indicated that the parts of the explosive were subjected to pre-shocking which has the potential to desensitize the explosive.

5.7 The effect of detonator shell material

Having examined the initiation of the booster for the case where the explosive is modelled with the regular I&G reactive model, we now include the desensitization model and investigate the influence of the desensitization phenomena on the initiation processes. The configurations considered are similar to the previous case where the material of the detonator is altered between aluminium and copper that is commonly used in industrial detonators and steel. Steel has a speed of sound that is roughly in the middle of the values of copper and aluminium and with a high density (similar to copper), it has higher impedance than the other two metals.

5.7. *The effect of detonator shell material*

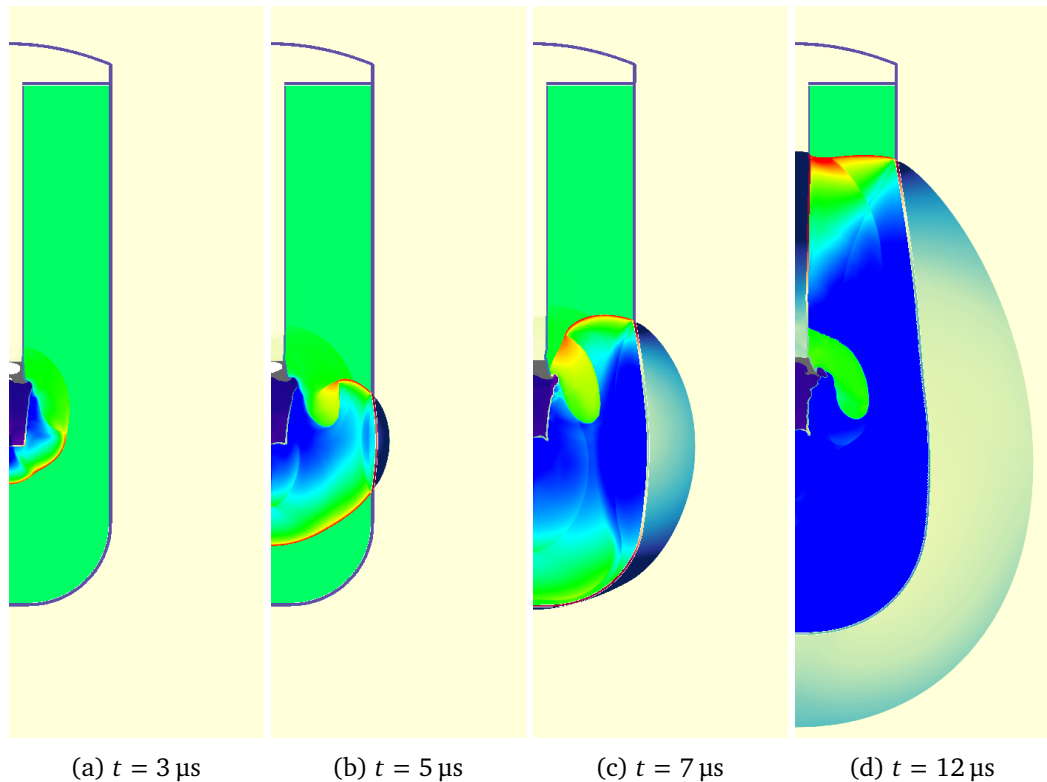


Figure 5.16: Plots of density depicting the effect of desensitization on the initiation of the booster explosive from an aluminium detonator. Part of the explosive is desensitized by the shock transmitted from the side of the detonator and remains non-reacted while the detonation propagates around it and consumes most of the booster charge.

5.7. *The effect of detonator shell material*

Figure 5.16 shows plots of the initiation of the booster by the aluminium detonator. The ignition of the detonator generated an impulse in the booster and lead to the formation of a detonation that is virtually indistinguishable from the case of no desensitization in early times. In fact, the initiation of the explosive in the area downstream of the detonator is the same as in the case of no desensitization. However, the upstream area shows distinct behaviour as is evident 5 μ s after initiation, in figure 5.16b. The inert shock transmitted from the side of the detonator has desensitized part of the explosive which prevents it from reacting. Nevertheless, the expansion of the detonation front is fast enough that overtakes the desensitizing shock, which gets slower and weaker as it expands, and manages to propagate around the desensitized region. Inside the desensitized part of the booster explosive, the detonation is quenched and is reduced to an inert shock.

In later times, the detonation propagates stably in the booster area above the detonator charge and consumes the remaining explosive. The non-reacted region persists through the simulation and is slightly compressed by pressure waves in the flow field. The explosive products expand and support the shock generated in the water.

The case of the booster initiated by the copper detonator is shown in figure 5.17. The differences with the case of no-desensitization are more profound for this configuration. The detonation front established by the time mark of 5 μ s is smaller and restricted close to the axis of the configuration. The weaker pulse transmitted from the sides of the detonator was not able to induce reactions. In subsequent times, the detonation expands into the pristine explosive downstream and even attains enough curvature to begin upstream propagation. However, this happens at a rate that has allowed the inert shock to desensitize a large region of the explosive next to the detonator. Once the detonation encounters this region, it is quenched and continues upstream as an inert shock.

For the configuration which has the steel detonator, the results are vastly similar to the copper shell. The detonation in the booster only manages to establish downstream of the detonator whereas a large region upstream is desensitized which prevents the detonation from further propagation. The resulting dead zone is shown in the plot of figure 5.18 and can be compared with the one from the copper configuration. The shape is similar with the only difference being that detonation was slightly faster and managed to propagate slightly further upstream.

The desensitization observed in the case of the copper detonator is critically extensive. The majority of the explosive has not been ignited as a desensitized region has blocked the propagation of the detonation upstream. As a consequence, the shock

5.7. The effect of detonator shell material

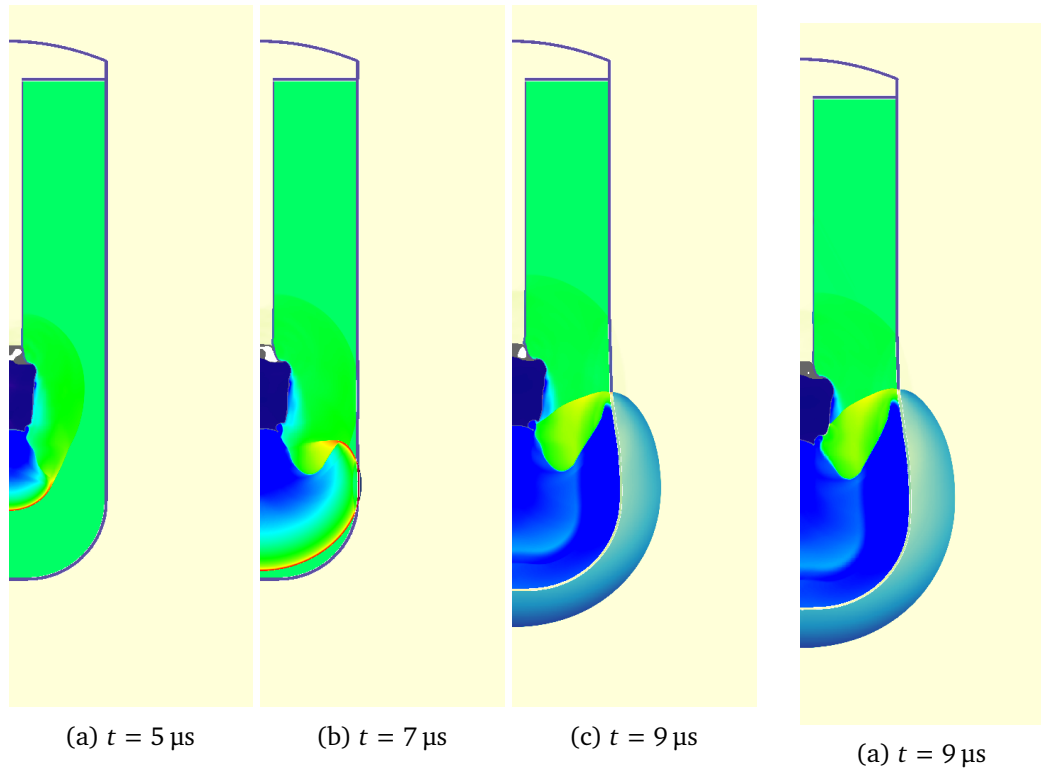


Figure 5.17: Plots of density depicting the effect of desensitization on the initiation of the booster explosive from a copper detonator. The slower formation of the detonation allows for the desensitization of a large region of the explosive which hinders the propagation of the detonation upstream of the detonator.

Figure 5.18: Initiation of the booster by a steel detonator is similar to case of copper.

5.8. *The effect of detonator shell thickness*

produced in the water is weaker and will also decay faster as it expands because of less support from the expansion of the explosive products. Overall, the quenching of the detonation in the booster will reduce its ability to ignite the surrounding explosive and potentially lead to failure in the initiation of the blasthole.

5.8 The effect of detonator shell thickness

We examine the effect of increasing the detonator shell thickness to 1 mm. The increased thickness will weaken the impulse from the detonator leading to a slower formation of the detonation. At the same time, the shocks transmitted from the side of the detonator which have been shown to desensitize the explosive will also be weaker and the desensitization will be slower. The combined effect of these processes will depend on their relative timings and strength and will be investigated in the following configurations.

Figure 5.19 displays plots from the configuration of the 1 mm thick aluminium shell. The booster explosive is ignited and a curved detonation front is established by the time mark of 5 μ s. Compared to the case of the 0.5 mm thick aluminium detonator the expansion of the detonation front is slower but does attain enough curvature to begin propagation upstream. However the shock transmitted from the sides of the detonator has caused the desensitization of a large region which has rendered it unable to detonate. Thus, the detonation can only propagate into an increasingly narrower region of pristine explosive. After the detonation is restricted to a region of approximately 3 mm in width, the detonation fails and most of the booster explosive remains non-reacted.

The copper and steel detonators with a thickness of 1 mm do not ignite the explosive in the booster at all. The thicker shell absorbs much of the energy from the explosion of the detonator and the impulse generated is too weak to cause a shock to detonation transition. Figure 5.20 shows the inert shock propagating in the explosive which is similar for both copper and steel. The shock is desensitizing the explosive but its effect is of no importance since a detonation has not been established.

5.9 The effect of detonator positioning

The investigation in the previous sections revealed that the influence of desensitization on the initiation process of the booster is to desensitize a region of the explosive next to the detonator which hinders the upstream propagation of the detonation. On the other

5.9. The effect of detonator positioning

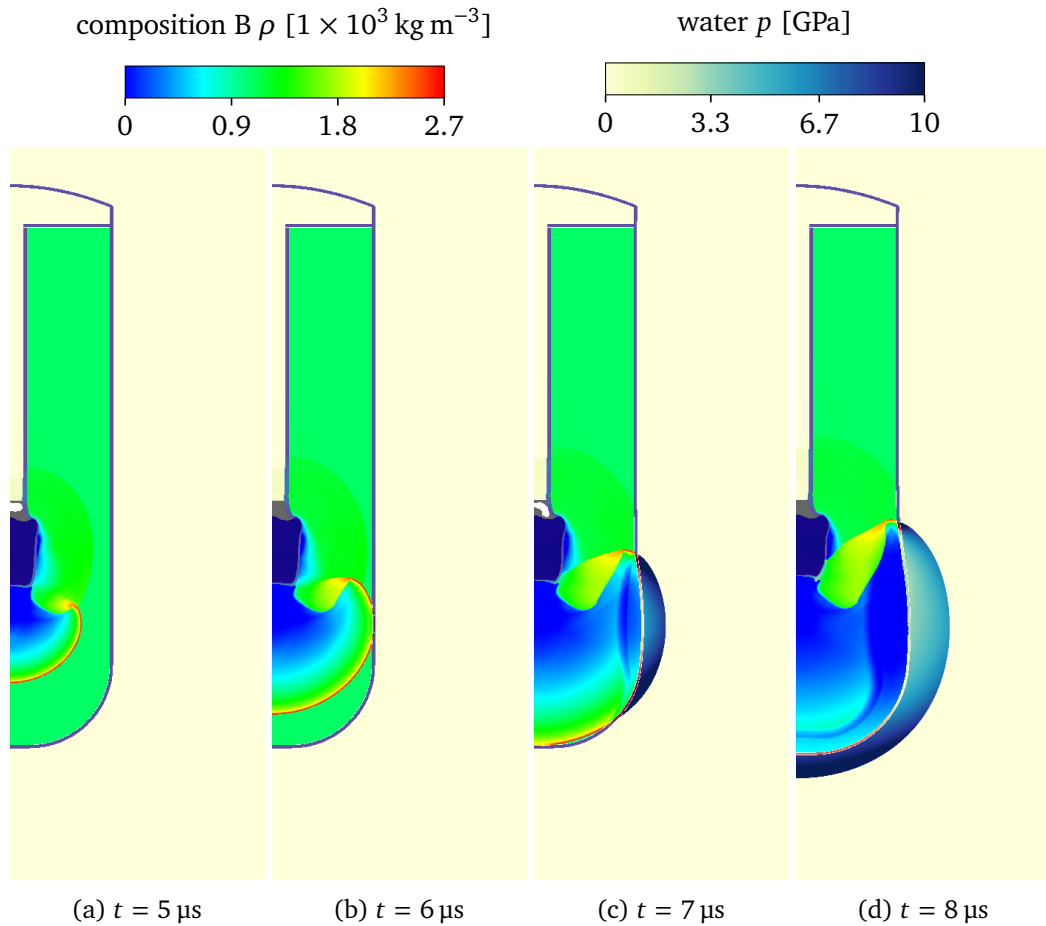


Figure 5.19: Plots of density depicting the initiation of the booster explosive from a 1 mm thick aluminium detonator. The impulse from the detonator is weakened compared to the thinner detonator and the detonation is slow to establish allowing for the extensive desensitization of the explosive. The detonation fails to propagate upstream from the detonator.

5.9. The effect of detonator positioning

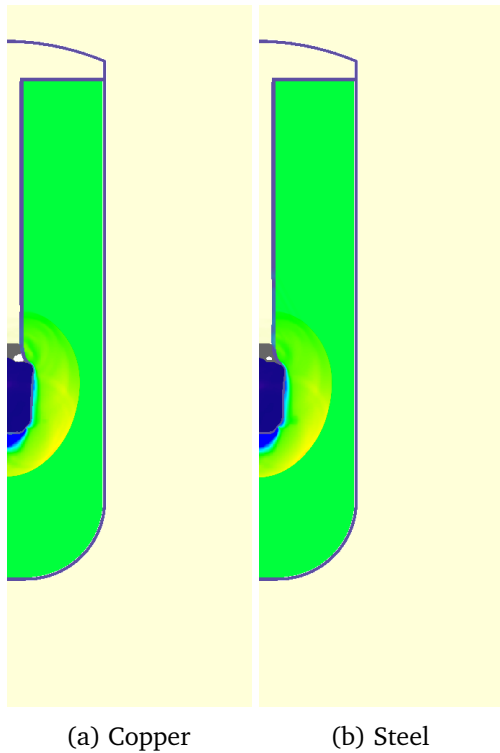


Figure 5.20: Plots of density for the booster configurations with a 1 mm thick copper and steel detonators which fail to ignite the explosive in the booster ($t = 5 \mu\text{s}$).

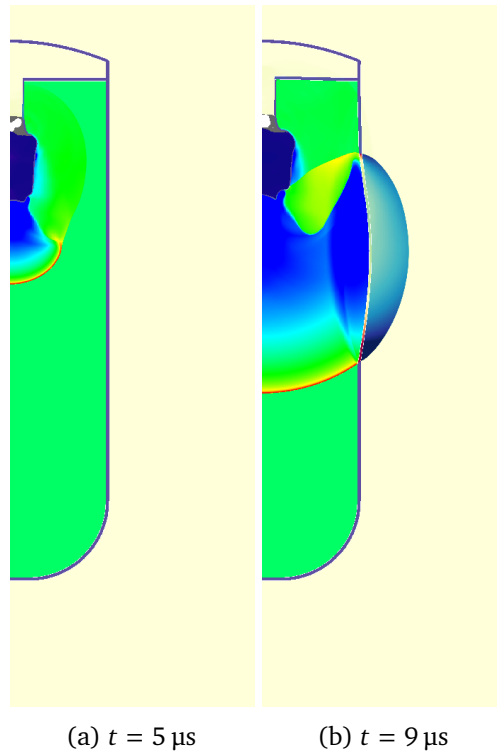


Figure 5.21: Plots of density depicting the initiation process for the booster configuration with a withdrawn steel detonator. The explosive upstream is desensitized and remains non-reacted but the detonation propagates downstream undisturbed, consuming most of the explosive.

5.10. Conclusions

hand, the detonation downstream propagates into pristine explosive and once it is established, it propagates undisturbed. This has motivated the examination of whether the positioning of the detonator will have a considerable impact on the efficiency of the booster.

We consider a configuration where the detonator is withdrawn by 60 mm towards the top of the booster and has a length of 30 mm. Given that the column of base explosive is only 13 mm in length, the explosive is not affected and its mass is the same as in the previous detonators. However, we do not consider whether such a short detonator is feasible from a manufacturing aspect and whether the additional components and circuitry can fit in such a short detonator. This design has the potential to ensure robust detonation of the majority of the booster even for configurations that are most prone to desensitization such as the 0.5 mm thick copper and steel shell.

Figure 5.21 shows plots for the configuration of the withdrawn detonator with a 0.5 mm thick steel shell and similar results are observed for the case of the copper shell as well. The detonation is established downstream while the region next to the detonator is being desensitized. Similar to the configuration of the longer detonator, the detonation does not manage to propagate upstream before the explosive is desensitized. However, the detonation downstream propagates as a single front and consumes all of the explosive below the detonator. Since most of the booster charge has detonated, the performance of the booster is greatly increased compared to the configurations of the long detonator in which all of the explosive upstream has not reacted.

5.10 Conclusions

The study presented in this chapter investigates the initiation process and performance of the detonator and booster configuration used to initiate tertiary explosives in mining blastholes. The numerical solution was obtained using several mathematical models ranging from the Euler equations for the fluid materials, to a two phase reactive model with desensitization for the explosive and an elastic-plastic formulation for the metal shell of the detonator.

The phenomenon of shock desensitization of explosives was introduced along with an extension of the reactive model to account for this effect. The implementation of the model is initially validated against a previously studied configuration involving diffraction around a rigid corner. This is extended to the case of a solid corner and even further by examining the configuration of the Jack Rabbit series of experiments.

The study of the initiation and performance of the booster used a design based on

actual industrial devices. An explosive commonly used in boosters is composition B which was modelled using the I&G reactive model for which a set of parameters exist in literature. However, the desensitization model has not been previously applied to it and no parameters exist. Following the example of DeOliveira et al. [14] and based on experiments from Campbell and Travis [74] and Held [76] a set of desensitization model parameters for composition B were determined.

The study of the booster configuration has revealed that the effect of shock desensitization can have great impact on the initiation of the booster charge and by extension, on its performance. In the cases without desensitization, all configurations lead to the complete detonation of the explosive in the booster. However, when accounting for desensitization effects all configurations were influenced and formed dead zones even though the amount of the remaining non-reacted explosive varied greatly depending on the type of detonator.

The mechanism by which desensitization influences the booster charge is through the shock transmitted from the side of the detonator. This shock is weaker than the one transmitted in the axial direction and does not lead to prompt reactions. Instead, it desensitizes an expanding region of the explosive next to the detonator and unless a detonation is established quickly and overtakes the weak shock it will desensitize the explosive all the way to the boundary and prevent the detonation from propagating in the upper region of the booster. This will result in a large portion of the explosive remaining after the detonation was quenched even though not all of it has been desensitized.

The effect of different materials for the shell of the detonator on the initiation of the booster was investigated. As was shown in chapter 4 the blast wave produced by detonators of different metal shell has significantly different magnitudes in the near field and this has a critical impact on the fine balance between desensitization and detonation. The aluminium detonator, which produces a stronger pulse, leads to the quick formation of a detonation which expands and propagates upwards before desensitization extends to a large region in the explosive. This is not the case for the copper shell where the detonation takes longer to establish and once it is diffracted upwards it encounters a fully desensitized region and is quenched.

Similar effects were observed for the configurations with the thicker detonator shells. The increased thickness causes a weaker impulse which made the initiation process more prone to desensitization. The configuration of the aluminium detonator led to detonation downstream of the detonator but it did not propagate upstream while the copper and steel shell did not ignite the booster explosive at all.

5.10. Conclusions

The outcomes of the numerical simulations clearly demonstrate that shock desensitization can have a detrimental impact on the initiation and performance of the booster which warrants its experimental investigation. Orica performed underwater tests of booster initiation in which they observed the detonation front on the surface of the booster and suggested that a dead zone was formed but they did not examine the process internally or the dead zone itself. Experimental studies that focus on shock desensitization in these devices are not available in literature and are highly required to establish the actual impact of shock desensitization and the extent of the agreement with the numerical results.

The critical influence of shock desensitization on the initiation of the booster identifies it as an important factor to be considered in the design of these devices. This study considered a configuration with a short detonator placed higher in the booster which was motivated by the observation that the detonation downstream of the detonator is robustly established in all cases and is not significantly influenced by desensitization. The results have confirmed that this configuration leads to the detonation of a larger portion of the explosive which increases the ability of the booster to ignite the surrounding explosive. Further investigations may consider alternative designs such as dumping the shock from the sides of the detonator using a specialized material or a simple air gap.

The work presented herein also showcases the capabilities and potential of the numerical methodology to aid the design and assessment of initiation devices. However, the use of a desensitization model is still a novel technique and there exist alternative reactive models that have shown promising results in capturing this phenomenon using different approaches. These should be further explored and evaluated in a wide range of applications involving shock desensitization to establish their accuracy and applicability in performing high-fidelity simulations of such applications. This effort also requires the extension of the available experimental data on the physical behaviour of explosive materials to enable the validation and advancement of the mathematical models as well as the calibration of the parameter sets.

Chapter 6

Conclusions

The advancement of reactive models for detonation and computational methods for multi-material simulations as well as the continuous increase of computational power have enabled the numerical study of increasingly complex explosive configurations. In this work, we employ the widely used and validated Ignition and Growth reactive model with extensions for porosity and desensitization along with accurate fluid and solid material models build into a multi-material framework to study explosive configurations of academic and industrial interest.

A hybrid diffuse interface model was implemented for the purposes of this study and was used to model two-phase explosives and an inert fluid material. The partial derivatives required for the calculation of the sound speed and the approximate Riemann solver wave speed estimates were derived for the case of a general equation of state. This allows the hydrodynamic model to be used with the majority of the continuum reactive models which usually feature two general EOS for the reactants and products and a reaction rate. The numerical algorithm was also extended beyond the classical finite volume methods to tackle the challenging aspects in the solution of the mathematical formulation.

The thesis begins with the study of detonation propagation in annular charges which considers both the transition and the steady state phase. The numerical results provide a full description of the evolution of detonation speed along the annular arc which resolves the fine features of the transition phase. These show a deviation from the exponential model suggested by other studies. A new description of the transition phase is proposed and supported by physical arguments and simulations of special test cases. The results are compared against an experimental study of the same configuration but the large uncertainties in the experimental data do not allow for a definite assessment

of the agreement between them. Experimental studies that consider the velocity of the detonation in annular charges are limited and there is a need for additional experiments that can provide high quality data for the validation of the outcomes of this study.

In addition, we conducted a parametric study on the dependence of the transition and steady state phase on the dimensions of the annulus. We confirmed previous findings on the affine dependence of reciprocal steady angular velocity on the inner radius of the annulus. The transition phase is examined in terms of its angular and temporal extent. We observed that the duration of the transition phase can either increase or decrease with inner radius depending on the width of the charge. This behaviour is explained using the new description of the evolution of detonation speed during the transition phase.

In the rest of the thesis, the focus was on the study of explosive devices used in the initiation of explosive blastholes in mining. In particular, we considered the detonator and booster configuration based on actual designs used in the industry. These devices have a complicated structure with multiple layers of explosive and inert materials that leads to complex interactions between the detonation wave and the solid structures.

The detonator was first studied in isolation guided by the underwater setup described in the European standard which is extensively used to assess the initiating capability of detonators. The investigation into the nature of the blast wave revealed distinct features in the characteristics of the blast wave between the near field and far field. In the near field, the blast wave is asymmetric and is stronger along the axis of the detonator in addition to showing distinct features depending on the material and thickness of the metal shell. However, these differences are lost in larger distances where the blast waves from different configurations all show similar features. Theoretical arguments and experimental evidence indicate that the differences in the blast waves observed in the near field translate into differences in the initiation capability. This suggests that the direct tests that consider the blast wave only at a single point in the far field are unable to accurately assess the initiation capability of detonators.

The detonator is then placed within a booster and the complete initiation configuration is examined. The explosive model was extended to account for shock desensitization and validated. Desensitization parameters for the booster explosive were determined from experimental data and used in the study of booster initiation. The numerical results showed that shock desensitization plays an important role in the performance of the booster. Desensitization is caused by the weak shock transmitted from the side of the detonator and unless a detonation is quickly established and proceeds to overtake it, it will lead to an extensive desensitized zone and prevent the

detonation of a large part of the explosive.

In the configuration which used the aluminium detonator, the desensitized region is limited and the detonation wave propagates around it and consumes the majority of the booster charge. Copper and steel detonators, which were found to generate weaker blast waves in the near field, lead to the desensitization of a large part of the booster charge next to the detonator and detonation was established only in the explosive region downstream. This motivated a configuration with a short detonator placed in the upper region of the booster. The impulse developed into a full detonation downstream and consumed the majority of the explosive. Large non-reacted parts of the booster charge indicate significant loss of the expected performance of the explosive initiation train. The study of the different configurations considered herein, highlights the influence of the materials and design in the ability to initiate explosives and showcase the potential of numerical methods in examining and assessing the initiating capability of detonators and boosters.

The numerical simulations of the detonator and booster configuration have provided insights into the internal initiation processes and performance of these devices that have not yet been observed experimentally. Modern experimental techniques are able to produce detailed and high quality experimental data that will provide a more comprehensive view into the physical behaviour of these devices. Such experiments should be pursued in order to provide the necessary data for the validation of the numerical results but also to assist in the advancement of the mathematical models.

6.1 Future work

Extensions of this study can be found in many directions. Considering the initiation capability of the detonator and booster device, an interesting investigation would be to place this configuration in an actual tertiary explosive used in mining and assess its initiation performance. This is straight-forward in terms of implementation, as it can be done with the models and methods used in this study. There exist several reactive models for ANFO that can be used within the computational framework of this study which also allows for multiple explosive and inert materials to be added. The difficulty with this extension would be the heavy computational cost of simulating such a setup and the large differences in the length scales and time scales of the involved processes.

In addition, the computational framework can be used to assess other designs for the booster that could alleviate the effect of desensitization. Certain shock damping materials or even an air gap can be placed between the detonator and booster to

6.1. *Future work*

examine its ability to weaken the shocks from the side of the detonator and evade heavy desensitization.

In addition to the study of applications, a further direction would be an improvement of the reactive material models. In particular, the desensitization model considered here is somewhat arbitrary and does not follow the relation between input pressure and desensitization time that has been observed experimentally. Further, the parameters of the model require calibration through experiments designed for this purpose, which has not been done yet. Lastly, another alternative is the use of a different reactive model, such as an entropy or temperature based model which have shown promising results in capturing desensitization without a dedicated desensitization model. A broad comparison of these models in conjunction with experimental data will be invaluable in determining the most appropriate representation of shock desensitization and will guide future numerical studies on the topic.

Bibliography

- [1] Wildon Fickett and William C. Davis. *Detonation: Theory and Experiment*. Dover Publications, 1973.
- [2] E. L. Lee and C. M. Tarver. “Phenomenological model of shock initiation in heterogeneous explosives”. In: *Physics of Fluids* 23.12 (1980), p. 2362. DOI: 10.1063/1.862940.
- [3] C. A. Handley et al. “The CREST reactive-burn model for explosives”. In: *EPJ Web of Conferences* 10 (2010). DOI: 10.1051/epjconf/20101000004.
- [4] Tariq D Aslam. “Shock temperature dependent rate law for plastic bonded explosives”. In: *Journal of Applied Physics* 123.14 (2018), p. 145901. DOI: 10.1063/1.5020172.
- [5] C. A. Handley et al. “Understanding the shock and detonation response of high explosives at the continuum and meso scales”. In: *Applied Physics Reviews* 5.1 (2018). DOI: 10.1063/1.5005997.
- [6] P C Souers et al. “Corner turning rib tests on LX-17”. In: *Propellants Explosives Pyrotechnics* 23.4 (1998), pp. 200–207.
- [7] S. N. Lubyatinsky et al. “Detonation Propagation in 180° Ribs of an Insensitive High Explosive”. In: *AIP Conference Proceedings* 706.1 (2004), pp. 859–862. DOI: 10.1063/1.1780372.
- [8] Clarence Hall and Spencer Pritchard Howell. *Investigations of detonators and electric detonators*. US Department of the Interior, Bureau of Mines., 1913.
- [9] R. L. Grant and J. E. Tiffany. “Determining the Initiating Efficiency of Detonators The Miniature-Cartridge Test”. In: *Industrial and Engineering Chemistry - Analytical Edition* 17.1 (1945), pp. 13–19. DOI: 10.1021/i560137a003.

Bibliography

- [10] T. S. Bajpayee and J. Edmund Hay. “Method of Comparing Initiating Strength of Detonators Using Adjustable-sensitivity Liquid Explosive”. In: *US Department of the Interior, Bureau of Mines*. (1994).
- [11] European Committee for Standardization (CEN). *Explosives for civil uses - Detonators and relays - Part 15: Determination of equivalent initiating capability*. Tech. rep. EU, 2004. DOI: 10.3403/03128972U.
- [12] Thomas M. Klapötke et al. “Determination of the Initiating Capability of Detonators Containing TKX-50, MAD-X1, PETNC, DAAF, RDX, HMX or PETN as a Base Charge, by Underwater Explosion Test”. In: *Propellants, Explosives, Pyrotechnics* 41.1 (2016), pp. 92–97. DOI: 10.1002/prop.201500220.
- [13] Hugh R James and Brian D Lambourn. “Shock Desensitization in Explosives: An Exploration of Two Competing Hypotheses.” In: *Fourteenth International Detonation Symposium*. US Office of Naval Research, 2010, pp. 1172–1181.
- [14] G. DeOliveira et al. “Detonation diffraction, dead zones, and the ignition-and-growth model.” In: *The Thirteenth Symposium (International) on Detonation*. (2006), Vol 16.
- [15] Sergei K. Godunov and Evgenii I. Romenskii. *Elements of Continuum Mechanics and Conservation Laws*. Boston, MA: Springer US, 2003. DOI: 10.1007/978-1-4757-5117-8.
- [16] Philip T. Barton and Dimitris Drikakis. “An Eulerian method for multi-component problems in non-linear elasticity with sliding interfaces”. In: *Journal of Computational Physics* 229.15 (Aug. 2010), pp. 5518–5540. DOI: 10.1016/j.jcp.2010.04.012.
- [17] G H Miller and P Colella. “A High-Order Eulerian Godunov Method for Elastic–Plastic Flow in Solids”. In: *Journal of Computational Physics* 167.1 (2001), pp. 131–176. DOI: 10.1006/jcph.2000.6665.
- [18] Stefan Schoch, Kevin Nordin-Bates, and Nikolaos Nikiforakis. “An Eulerian algorithm for coupled simulations of elastoplastic-solids and condensed-phase explosives”. In: *Journal of Computational Physics* 252 (2013), pp. 163–194. DOI: 10.1016/j.jcp.2013.06.020.
- [19] L Michael and N Nikiforakis. “A multi-physics methodology for the simulation of reactive flow and elastoplastic structural response”. In: *Journal of Computational Physics* 367 (Aug. 2018), pp. 1–27. DOI: 10.1016/j.jcp.2018.03.037.

- [20] L. Michael and N. Nikiforakis. “A hybrid formulation for the numerical simulation of condensed phase explosives”. In: *Journal of Computational Physics* 316 (July 2016), pp. 193–217. DOI: 10.1016/j.jcp.2016.04.017.
- [21] Grégoire Allaire, Sébastien Clerc, and Samuel Kokh. “A Five-Equation Model for the Simulation of Interfaces between Compressible Fluids”. In: *Journal of Computational Physics* 181.2 (Sept. 2002), pp. 577–616. DOI: 10.1006/jcph.2002.7143.
- [22] J. W. Banks et al. “A high-resolution Godunov method for compressible multi-material flow on overlapping grids”. In: *Journal of Computational Physics* 223.1 (2007), pp. 262–297. DOI: 10.1016/j.jcp.2006.09.014.
- [23] A. K. Kapila et al. “A study of detonation diffraction in the ignition-and-growth model”. In: *Combustion Theory and Modelling* 11.5 (Sept. 2007), pp. 781–822. DOI: 10.1080/13647830701235774.
- [24] Craig M. Tarver. “Ignition and Growth Modeling of LX-17 Hockey Puck Experiments”. In: *Propellants, Explosives, Pyrotechnics* 30.2 (Apr. 2005), pp. 109–117. DOI: 10.1002/prop.200400092.
- [25] Craig M. Tarver. “Corner Turning and Shock Desensitization Experiments plus Numerical Modeling of Detonation Waves in the Triaminotrinitrobenzene Based Explosive LX-17”. In: *The Journal of Physical Chemistry A* 114.8 (Mar. 2010), pp. 2727–2736. DOI: 10.1021/jp9098733.
- [26] Bram van Leer. “Towards the Ultimate Conservative Difference Scheme”. In: *Journal of Computational Physics* 135.2 (Aug. 1997), pp. 229–248. DOI: 10.1006/jcph.1997.5704.
- [27] Bram van Leer. “Towards the ultimate conservative difference scheme. II. Monotonicity and conservation combined in a second-order scheme”. In: *Journal of Computational Physics* 14.4 (Mar. 1974), pp. 361–370. DOI: 10.1016/0021-9991(74)90019-9.
- [28] Eleuterio F. Toro. *Riemann Solvers and Numerical Methods for Fluid Dynamics*. Vol. 1. Berlin, Heidelberg: Springer Berlin Heidelberg, 2009. DOI: 10.1007/978-3-662-03915-1. eprint: arXiv:1011.1669v3.
- [29] Richard Saurel, Fabien Petitpas, and Ray A. Berry. “Simple and efficient relaxation methods for interfaces separating compressible fluids, cavitating flows and shocks in multiphase mixtures”. In: *Journal of Computational Physics* 228.5 (Mar. 2009), pp. 1678–1712. DOI: 10.1016/j.jcp.2008.11.002.

Bibliography

- [30] Zhao Tonghu et al. “An Experimental Study of Detonation Propagation in the Arc Insensitive High Explosive Initiated on the Basal Plane”. In: *Eleventh International Detonation Symposium, Snowmass, Colorado, USA*. US Office of Naval Research, 1998, pp. 1023–1028.
- [31] John B. Bdzil et al. “High-Explosives Performance”. In: *Los Alamos Sci* 28 (2003), pp. 96–110.
- [32] Larry G Hill and Tariq D Aslam. “Detonation shock dynamics calibration for PBX 9502 with temperature, density, and material lot variations”. In: *Fourteenth International Detonation Symposium*. Vol. 836. 2010, pp. 779–788.
- [33] Mark Short et al. “Steady detonation propagation in a circular arc: a Detonation Shock Dynamics model”. In: *Journal of Fluid Mechanics* 807 (2016), pp. 87–134. DOI: 10.1017/jfm.2016.597.
- [34] Hisahiro Nakayama et al. “Stable detonation wave propagation in rectangular-cross-section curved channels”. In: *Combustion and Flame* 159.2 (2012), pp. 859–869. DOI: 10.1016/j.combustflame.2011.07.022.
- [35] P. C. Souers et al. “The Diverging Sphere and the Rib in Prompt Detonation”. In: *12th Symposium (International) on Detonation* 5.1 (2002), pp. 1–7.
- [36] Jirí Jiří Vágenknecht and Vladislav Adamík. “A contribution to the analysis of corner turning rib problems”. In: *Propellants, Explosives, Pyrotechnics* 31.4 (2006), pp. 299–305. DOI: 10.1002/prop.200600041.
- [37] Craig M. Tarver et al. “Ignition and growth modeling of detonating TATB cones and arcs”. In: *AIP Conference Proceedings*. Vol. 955. 2008, pp. 429–432. DOI: 10.1063/1.2833085.
- [38] John H. S. Lee. *The Detonation Phenomenon*. Cambridge: Cambridge University Press, 2008. DOI: 10.1017/CBO9780511754708.
- [39] P. Clark Souers et al. “Air Gaps, Size Effect, and Corner-Turning in Ambient LX-17”. In: *Propellants, Explosives, Pyrotechnics* 34.1 (Feb. 2009), pp. 32–40. DOI: 10.1002/prop.200700232.
- [40] S A Sheffield and R Engelke. “Condensed-Phase Explosives: Shock Initiation and Detonation Phenomena”. In: *Shock Wave Science and Technology Reference Library, Vol. 3*. Ed. by Yasuyuki Horie. Berlin, Heidelberg: Springer Berlin Heidelberg, 2009, pp. 1–64. DOI: 10.1007/978-3-540-77080-0_1.

- [41] Craig M. Tarver and Estella M. McGuire. “Reactive flow modeling of the interaction of TATB detonation waves with inert materials”. In: *Twelfth International Detonation* 1 (2002), pp. 1–10.
- [42] R L Grant and J. E. Tiffany. “Factors Affecting Initiating Efficiency of Detonators.” In: *Industrial & Engineering Chemistry* 37.7 (July 1945), pp. 661–666. DOI: 10.1021/ie50427a017.
- [43] V. Petr and E. Lozano. “Characterizing the energy output generated by a standard electric detonator using shadowgraph imaging”. In: *Shock Waves* 27.5 (2017), pp. 781–793. DOI: 10.1007/s00193-017-0718-8.
- [44] Wen Yu, Bruce Underwood, and Stainislav Nikolov. *Underwater Testing of i-kon and Exel Detonators*. Tech. rep. Orica, 2013.
- [45] G Bjarnholt. “Strength Testing of Explosives by Underwater Detonation”. In: *Propellants, Explosives, Pyrotechnics* 3.1-2 (Apr. 1978), pp. 70–71. DOI: 10.1002/prep.19780030117.
- [46] Vječislav Bohanek, Mario Dobrilović, and Vinko Škrlec. “Influence of the initiation energy on the velocity of detonation of ANFO explosive”. In: *Central European Journal of Energetic Materials* 10.4 (2013), pp. 555–568.
- [47] United Nations. *Transport of Dangerous Goods: Manual of Tests and Criteria*. Tech. rep. United Nations, 2009.
- [48] Robert Matyáš and Jiří Pachman. *Primary explosives*. Vol. 9783642284. Berlin, Heidelberg: Springer Berlin Heidelberg, 2012, pp. 1–338. DOI: 10.1007/978-3-642-28436-6.
- [49] William Payman, Donald Whitley Woodhead, and Harold Titman. “Explosion waves and shock waves Part II—The shock wave and explosion products sent out by blasting detonators”. In: *Proceedings of the Royal Society of London. Series A - Mathematical and Physical Sciences* 148.865 (Feb. 1935), pp. 604–622. DOI: 10.1098/rspa.1935.0036.
- [50] Robert H. Cole. *Underwater explosions*. Princeton, Princeton Univ. Press, 1948. DOI: 10.5962/bhl.title.48411.
- [51] John M. Dewey. “Expanding Spherical Shocks (Blast Waves)”. In: *Handbook of Shock Waves*. Elsevier, 2001. Chap. 13.1, pp. 441–481. DOI: 10.1016/B978-012086430-0/50029-4.

Bibliography

- [52] Ralph Menikoff. “Empirical equations of state for solids”. In: *ShockWave Science and Technology Reference Library, Vol. 2*. Ed. by Yasuyuki Horie. Springer, 2007, pp. 143–188. DOI: 10.1007/978-3-540-68408-4_4.
- [53] L Davison et al. *Fundamentals of Shock Wave Propagation in Solids*. Shock Wave and High Pressure Phenomena. Berlin, Heidelberg: Springer Berlin Heidelberg, 2008. DOI: 10.1007/978-3-540-74569-3.
- [54] Keh-Ming Shyue. “A Fluid-Mixture Type Algorithm for Compressible Multicomponent Flow with van der Waals Equation of State”. In: *Journal of Computational Physics* 156.1 (1999), pp. 43–88. DOI: 10.1006/jcph.1999.6349.
- [55] M. Greenspan and C.E. E Tschiegg. “Speed of sound in water by a direct method”. In: *Journal of Research of the National Bureau of Standards* 59.4 (1957), p. 249. DOI: 10.6028/jres.059.028.
- [56] Craig M. Tarver, R. Don Breithaupt, and John W. Jon W. Kury. “Detonation waves in pentaerythritol tetranitrate”. In: *Journal of applied physics* 81.February (1997), pp. 7193–7202. DOI: 10.1063/1.365318.
- [57] B M Dobratz and P C Crawford. *LLNL Explosives Handbook*. 1985.
- [58] L. G. Green and E. L. Lee. “Detonation Pressure Measurements on PETN”. In: *13th Symposium (International) on Detonation* (2006).
- [59] Paul Harris and Henri Noel Presles. “Reflectivity of a shock front in water and nitromethane”. In: *The Journal of Chemical Physics* 80.1 (1981), pp. 524–527. DOI: 10.1063/1.446425.
- [60] Haibin Zhou et al. “Signal analysis and waveform reconstruction of shock waves generated by underwater electrical wire explosions with piezoelectric pressure probes”. In: *Sensors (Switzerland)* 16.4 (2016). DOI: 10.3390/s16040573.
- [61] G. I. Taylor. “The formation of a blast wave by a very intense explosion I. Theoretical discussion”. In: *Proceedings of the Royal Society of London. Series A. Mathematical and Physical Sciences* 201.1065 (Mar. 1950), pp. 159–174. DOI: 10.1098/rspa.1950.0049.
- [62] Hans A. Bethe et al. “Blast Wave”. In: *Los Alamos Scientific Laboratory* (1947).
- [63] Harold L. Brode. “Blast wave from a spherical charge”. In: *Physics of Fluids* 2.2 (1959), pp. 217–229. DOI: 10.1063/1.1705911.

- [64] G. J. Sharpe and J. B. Bdzil. “Interactions of inert confiners with explosives”. In: *Journal of Engineering Mathematics* 54.3 (2006), pp. 273–298. DOI: 10.1007/s10665-005-9025-y.
- [65] H. R. James and B. D. Lambourn. “On the systematics of particle velocity histories in the shock-to-detonation transition regime”. In: *Journal of Applied Physics* 100.8 (2006). DOI: 10.1063/1.2354416.
- [66] Hugh R James. “Comparison of Shock Initiation Threshold Criteria for Projectiles with Flat Impact Surfaces”. In: *15th International Detonation Symposium* (2014), pp. 629–638.
- [67] B Mohanty. “Intra-hole and inter-hole effects in typical blast designs and their implications on explosives energy release and detonator delay time—A critical review”. In: *Fragblast 9: Proceedings of the 9th Int. Symp. on Rock Fragmentation by Blasting*. 2009, pp. 23–31.
- [68] John T Aler, Michael S Wieland, and Explosives Group. “The waiting time recovery test”. In: *International Society of Explosives Engineers* (2000), pp. 59–67.
- [69] PD Katsabanis et al. *Explosives malfunction from sympathetic detonation to shock desensitization*. Tech. rep. International Society of Explosives Engineers, Cleveland, OH (United States), 1994.
- [70] M.S. Wieland. “Shock Wave Damage to Coal Mine Delay Detonators”. In: *Proceedings of the 14th Symposium on Explosives and Pyrotechnics*. Franklin Research Center, Philadelphia, PA, 1989.
- [71] W Campbell et al. “Shock Initiation of Solid Explosives”. In: *Physics of Fluids* 4.4 (1961), pp. 511–521. DOI: 10.1063/1.1706354.
- [72] T. Hussain and Liu Yan. “Single and double shock initiation modelling for high explosive materials in last three decades”. In: *IOP Conference Series: Materials Science and Engineering* 146.1 (2016). DOI: 10.1088/1757-899X/146/1/012041.
- [73] B. E. Drimmer and T. P. Liddiard. “Propagation failure in solid explosives under dynamic pre-compression”. In: *United States Naval Ordnance Laboratory* (1964).
- [74] A W Campbell and J R Tarvis. *Shock desensitization of PBX-9404 and Composition B-3*. Tech. rep. Los Alamos National Lab., NM (USA), 1985.
- [75] Kevin S Vandersall et al. “Shock Desensitization Experiments and Reactive Flow Modeling on Self-Sustaining LX-17 Detonation Waves”. In: *15th International Detonation Symposium*. 2014, pp. 333–340.

Bibliography

- [76] Manfred Held. “Corner turning research test”. In: *Propellants, Explosives, Pyrotechnics* 21.4 (1996), pp. 177–180. DOI: 10.1002/prop.19960210403.
- [77] W C Davis. “Shock Desensitizing of Solid Explosive”. In: *14th International Detonation Symposium* (2010), pp. 1058–1064. eprint: No.LA-UR-10-00810.
- [78] Tariq D. Aslam et al. “Multi-shock and isentropic compression of the tri-amino-tri-nitro-benzene based explosive PBX 9502 : Evaluation of reactive flow models”. In: *Fifteenth Symposium (International) on Detonation* (2014), pp. 1166–1175.
- [79] B. L. Wescott, D. Scott Stewart, and W. C. Davis. “Equation of state and reaction rate for condensed-phase explosives”. In: *Journal of Applied Physics* 98.5 (2005). DOI: 10.1063/1.2035310.
- [80] B L Wescott, D S Stewart, and W C Davis. “Modeling detonation diffraction and dead zones in PBX-9502”. In: *Proc., Symp. Detonation, 13th, Norfolk, Virginia*. 2006.
- [81] P. A. Urtiew C. M. Tarver, T. M. Cook and W. C. Tao. “Multiple Shock Initiation of LX-17”. In: *Tenth International Detonation Symposium, Boston*. 1993.
- [82] Craig M. Tarver. “Modeling Detonation Experiments on Triaminotrinitrobenzene (TATB)-Based Explosives LX-17, PBX 9502, and Ultrafine TATB”. In: *Journal of Energetic Materials* 30.3 (2012), pp. 220–251. DOI: 10.1080/07370652.2011.563770.
- [83] N. J. Whitworth. “CREST modelling of PBX 9502 corner turning experiments at different initial temperatures”. In: *Journal of Physics: Conference Series* 500.5 (2014). DOI: 10.1088/1742-6596/500/5/052050.
- [84] Roberta N. Mulford, Stephen A. Sheffield, and Robert R. Alcon. “Preshock desensitization of PBX explosives”. In: *AIP Conference Proceedings* 309.1994 (1994), pp. 1405–1408. DOI: 10.1063/1.46243.
- [85] P. Clark Souers et al. “LX-17 corner-turning”. In: *Propellants, Explosives, Pyrotechnics* 29.6 (2004), pp. 359–367. DOI: 10.1002/prop.200400067.
- [86] Mark M. Hart, Oliver T. Strand, and Stephen T. Bosson. *Jack Rabbit Pretest Data For TATB Based IHE Model Development*. Tech. rep. Lawrence Livermore National Laboratory, 2008, p. 209.
- [87] Nicolas Desbiens. “Modeling of the jack rabbit series of experiments with a temperature based reactive burn model”. In: *AIP Conference Proceedings*. Vol. 040034. 2017, p. 040034. DOI: 10.1063/1.4971528.

Bibliography

- [88] P. a. Urtiew et al. “Shock initiation of composition B and C-4 explosives: Experiments and modeling”. In: *Russian Journal of Physical Chemistry B* 2.2 (2008), pp. 162–171. DOI: 10.1134/S1990793108020036.
- [89] Toru Hamada, Yuichi Nakamura, and Shigeru Itoh. “The Performance of Pressure Vessel Using Concentric Double Cylindrical High Explosive”. In: *Journal of Pressure Vessel Technology* 126.4 (2004), p. 409. DOI: 10.1115/1.1804201.